Università degli Studi di Padova

Department of Industrial Engineering

Master of Science in Aerospace Engineering

Wall-Modeled LES of supersonic turbulent boundary layers over a compression ramp

Thesis advisor
Dott. Michele Cogo

Thesis co-advisor
Prof. Francesco Picano

Candidate: Niccolò Lazzari
Matriculation number: 2122351

Academic year 2025/2026

Abstract

The necessity of predicting the physics behind shock turbulent boundary layer interactions is one of the crucial subjects for aerospace engineering applications, ranging from atmospheric reentry, efficient propulsion system design to fluid-structure interaction and noise reduction in high-speed aircraft. The prohibitive computational cost required to resolve all the scales present in a flow is a significant challenge in numerical simulations. Direct numerical simulations (DNS) are limited to relatively low Reynolds numbers due to their high computational cost, while large-eddy simulations (LES) use subgrid-scale models to represent the unresolved small-scale turbulent motions, thereby enabling simulations at higher Reynolds numbers. Reynolds-averaged Navier-Stokes (RANS) simulations, because of their low computational cost can be used over a wide range of Reynolds numbers, as they provide access to the mean flow field at the expense of time-resolved representation of local flow features. However, capturing the boundary-layer structures generated by solid walls is still computationally prohibitive for most practically relevant flow conditions.

The purpose of this work is to implement a wall-model technique for large-eddy simulation for the first time using an Immersed Boundary Method (IBM) in the open source numerical solver STREAmS, reducing the computational cost of describing the interaction between a supersonic flow over a compression ramp, given the value of a certain distance from the wall, called the matching location.

The main focus is the implementation of the same setup and validation against a recent work presented by Dawson et al., (2013) [19], where the free-stream Mach number is $M_\infty = 2.9$ and the ramp angle $\theta = 24^\circ$. The results obtained using grid configurations ranging from coarse to fine and different matching locations are consistent with theoretical predictions. The choice of matching location has an higher impact than the specific mesh configuration over the predicted friction coefficient and mean pressure distribution across the domain, highlighting that, for a fixed matching location but different grid configurations, the finer grid captures the influence of the adverse pressure gradient more effectively. They emphasizes the limitations of the equilibrium wall model in faithfully representing the physics when flow separation occurs, especially when compared to a DNS and experimental analysis, Wu & Martin (2008) [13] and Riguette et al., (2009) [14]. Concerning the oblique shock wave, the model predicts accurately the fluid properties jump over the shock wave itself and the oblique angle with a deviation error lower than $\epsilon_{prop} = 4\%$ and $\epsilon_\beta = 2\%$ respectively.

In the future, it may be useful to investigate implementing a wall model that can represent strongly non-equilibrium flow features and rough surfaces, in order to obtain a more complete understanding of the supersonic case.

Contents

1 Introduction

1.1 State of the art

Turbulence and turbulent fluid flows have been the focus of research for over 100 years, and their complete solution still eludes engineers and scientists. Since an important focus of the material will be on engineering aerodynamic flows, it is useful to provide some historical background on the research trends to date. In the 1930s, research groups became focused on the study of compressible, high-speed boundary layer flows, with extensive experimentation on rockets. In the 1930s and throughout the 1940s, extensive work was done on compressible turbulent flows. In the 1950s, compressible flow research was vigorously pursued through both experiments and theory, and the foundational studies from that era continue to inform modern analysis of turbulent flows as well as key applications in manned and unmanned space missions. For vehicles traveling through the atmosphere, flight in the supersonic regime is associated with aerodynamic drag and heat transfer, as it influences both structural integrity and aerodynamic performance. Because of the combined thermal and acoustic loads, the panel structure may exhibit nonlinear random vibration responses. The thermal loads due to aerodynamic heating cause thermal buckling and post-buckling of the panel, which result in a sudden change in vehicle configuration. Deformation of the structure leads to a modified aerodynamic profile, and the aerodynamic flow properties over the vehicle will change. At these speeds, shock waves are formed around the vehicle's surface, which, depending on the body shape, can develop at different angles. A possible example is the YF-12A Blackbird aircraft, which is capable of sustaining Mach 3, Fig 1a. Aerodynamic friction and continuous engine operation during high-speed flight subject some parts of the airplane to temperatures as high as 840 K, with an average surface temperature ranging from 512 K to 600 K. For this aircraft, the use of titanium, stainless steel, and other advanced alloys, as well as high-temperature plastics and a configuration to prevent corrosion and stress-corrosion cracking, is implemented. Another illustration is the intake of the Concorde's supersonic aircraft engine, Fig. 1b. To enhance overall engine performance, the airflow through the engine section is adjusted at various flight speeds using a variable-geometry intake control system. When cruising supersonically at Mach 2, a supersonic shock wave is generated at the engine inlet.

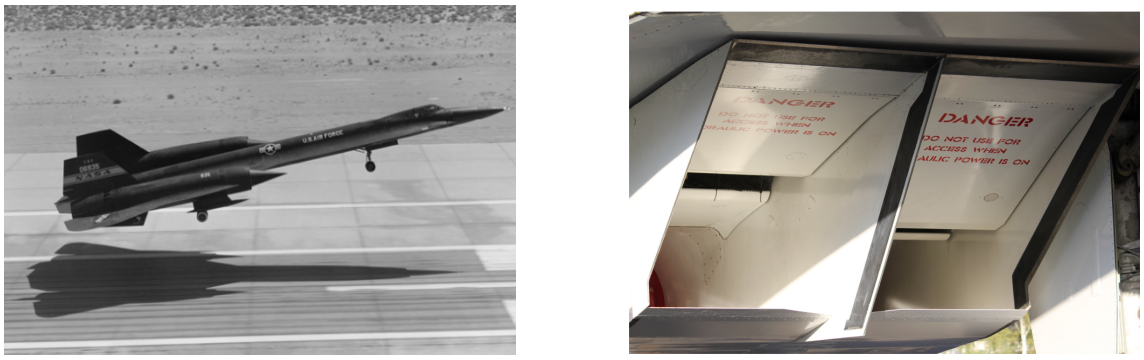

(a) (b)

Figure 1: (a) YF-12A Lockheed Blackbird supersonic $M = 3$ aircraft. (b) Concorde intake engine nozzle. (credit: NASA)

An example of how destructive interactions between shock waves and boundary layers are shown in the images from an X-15 test flight, where shock-shock and shock-boundary layer interactions significantly damaged the body and a control surface of the aircraft at Mach 6.7. In these applications, the understanding of compressible fluid dynamic helps improve efficiency and reduce operational costs, Fig 2. Therefore, the development of a turbulent boundary layer over compression ramps

(a)

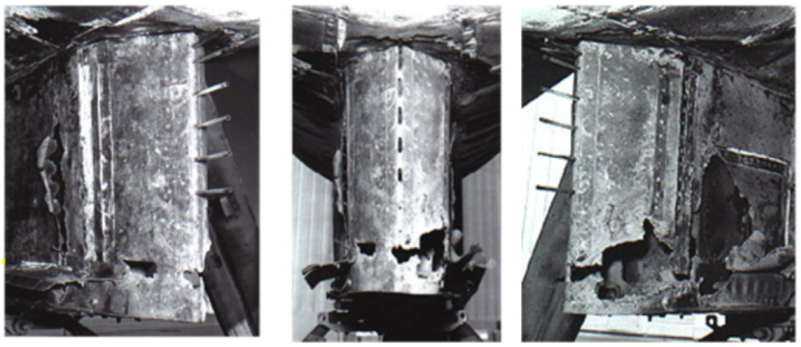

(b)

Figure 2: (a) Hypersonic X-15 aircraft. (b) Damages on control surfaces of X-15 test flight. (credit: NASA)

is considered a classic problem in high-speed aerodynamics, due to the intricate interaction between shock waves and turbulence confined near the wall.
Furthermore, inadequate management of shock turbulent boundary layer interaction (STBLI) can diminish, or even completely nullify, the effectiveness of hypersonic vehicle control surfaces. Although STBLI plays a critical role in both propulsion and aerodynamic systems, our understanding of its underlying physics in many key areas remains incomplete: we still lack dependable, cost-efficient tools to accurately predict the advantages of new STBLI control strategies.
Despite many decades of experimental and theoretical investigations, as well as extensive numerical studies using DNS (Wu & Martin, 2008; Pirolizzi & Grasso, 2006) and LES (Garnier et al., 2002; Touber & Sandham, 2009) which have substantially improved our comprehension of this interaction, accurately predicting turbulent boundary layers over compression ramps by numerical means still remains a challenging problem. A primary issue in comparing experimental results with numerical simulations is that the high Reynolds numbers reached in experiments cannot be

reproduced in simulations, since the computational effort needed to resolve all scales of the flow would be prohibitively large. Reynolds-Averaged Navier-Stokes (RANS) models are computationally inexpensive but frequently fail to accurately predict separation length, reattachment characteristics, and detailed turbulence behavior. In contrast, Large Eddy Simulation (LES) can better resolve turbulent structures but requires far greater computational effort, particularly at high Reynolds numbers that are typical of practical configurations. The full range of turbulent motions is directly resolved by Direct Numerical Simulation (DNS), but due to its extremely high computational cost, it is not practical for most realistic flow scenarios.
For this reason, in recent years, there has been a growing need to develop new experimental and practical solutions to this problem. A wide variety of methods have been introduced to address this "near-wall problem", all of which share the same fundamental goal: bypassing the necessity of resolving the turbulent eddies in the inner region of the boundary layer. The various methods to model turbulence are based on different rationales, specifically regarding whether they model or directly resolve the outer part of the boundary layer.
Therefore, the central aim of this study is to validate a method that does not explicitly resolve the energetic motions in the outer boundary layer while representing them through modeling in the inner one. This approach is referred to as "wall-modeled LES" or "WMLES". An Equilibrium Wall Model (EWM) is used to evaluate its capability in predicting STBLI over a compression ramp with an inclination angle of $\theta = 24^{\circ}$ at a freestream Mach number of 2.9. The validation is performed using several mesh configurations, ranging from coarse to fine grids with a stretching approach close to the ramp corner, in order to identify potential differences arising from changes in the input parameters. In order to determine the limitations of the model, it must be compared with DNS data and experimental results for the same case study.

1.2 Bibliographic research

The study of the behavior of incipient turbulent boundary layer separation under different conditions allows for obtaining solid and practical results that can be applied to the design of high-speed aircraft or turbomachinery.
Therefore, the interest in reducing the high computational cost associated with simulating turbulent boundary layers led to the emergence of wall modeling as a potential solution.
Beginning with Deardorff's pioneering work in 1970 [4] and extending into the late 1990s, other approaches were proposed, including the hybrid LES/RANS methods of Schumann (1975) [5] and Bagget (1998) [6]. The status of wall-modeling research up to the early-to-mid 2000s was thoroughly reviewed by Piomelli & Balaras (2002) [10] and Piomelli (2008) [12].
Then a comprehensive overview of the near-wall problem in LES, along with how it can be addressed via modeling, is provided by Larsson et al., (2016) [20]. The authors identify in "log-layer mismatch" the most persistent source of error in wall-modeled LES, in which the mean velocity profile plotted in viscous units is displaced either upward or downward. The predicted wall shear stress is also directly affected by this discrepancy because the skin-friction coefficient scales with $1/U_\infty^2$. Accurately predicting skin friction is crucial not only for drag estimation but also for forecasting boundary layer separation, since the accumulated loss of near-wall momentum in the upstream boundary layer controls the separation location.
Based on this, it is possible to highlight the reference work and its main findings regarding the intricate coupling of the turbulent boundary layer over a compression ramp.
Settles et al., (2012) [16] investigates the interaction between a shock wave and a compressible turbulent boundary layer at a fixed Mach number 2.9, using nominal Reynolds numbers representative of those encountered by large high-speed aircraft in flight and employing various compression ramp configurations. The separation begins with initial corner angles in a range of roughly 16° to 18°, and it does not start abruptly; instead, it develops progressively. Over the range studied, the incipient separation angle was found to be essentially independent of the Reynolds number.
Even when the flow is nominally attached at small corner angles, there exist tiny, separated zones at the corner embedded within the overall attached flow.
A similar methodology is adopted by Li et al., (2017) [22], who, using a DNS approach, investigate how increasing the corner angle influences the size of the separation bubble as well as the associated unsteadiness and frequency. Based on their analysis of the separation region, Zhu et al., (2016) [21] examined how wall temperature influences the STBLI. Wall temperature has a strong impact on the size of the separation bubble, which expands significantly as the wall becomes hotter. The findings clarify how elevated wall temperatures enlarge the separated flow region and shift the shock interaction point further upstream. Heating thickens the boundary layer and generates more large-scale vortical structures, whereas cooling diminishes the overall vorticity.
Bermejo-Moreno et al., (2011) [15] replicate the experimental conditions of Helmer & Eaton (2011) to perform a WMLES simulation of the interaction of an oblique shock and a turbulent boundary layer in a low aspect-ratio duct.
Dawson et al., (2013) [19] conducted a detailed study on the application of wall-modeling techniques in large-eddy simulations of a supersonic turbulent boundary

layer at $M_\infty = 2.9$ over a 24° compression ramp. By comparing a wall-resolved LES (WRLES) with a wall-modeled LES (WMLES) at different reference Reynolds numbers, they assessed the limitations of the latter in predicting shock-turbulent boundary layer interactions. Their skin friction analysis demonstrates that WMLES does not accurately capture this coefficient in the recovery region and underestimates the separation length. These findings highlight the shortcomings of the equilibrium wall model, in particular its inability to account for non-equilibrium effects.
The direct numerical simulations reported by Wu & Martin [13] concentrate on the characteristic frequency associated with the shock motion, and to validate the results, this solid reference set of data is used. The results show that both the shock oscillation and the movement of the separation point are correlated with, and lag behind, the motion of the reattachment point, indicating that the downstream flow plays a key role in driving the low-frequency shock motion.
Based on the DNS study by Wu & Martin (2008), Riguette et al., (2009) [14] conduct experiments to examine the flow behavior at a Mach number of 2.9 over a compression ramp inclined at 24°. Their analysis of the mean pressure and velocity profiles reveals that, even at locations far downstream from the ramp corner, the flow is still turning and decelerating during the final phase of the compression.

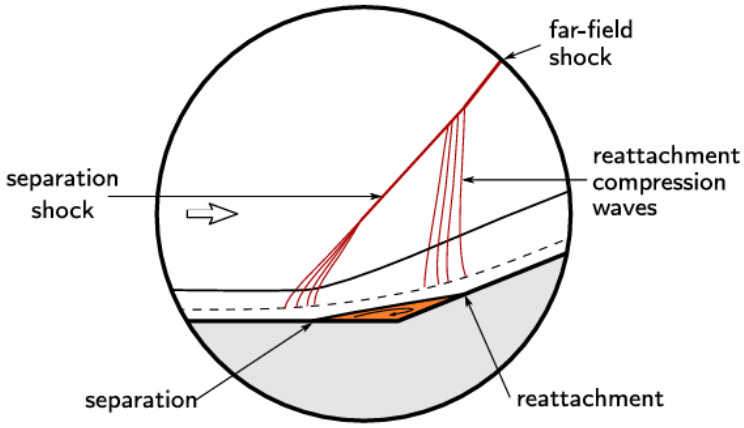

Figure 3: Sketch of the compression ramp problem and the shock waves representation, (Kshitij Sabnis & Holger Babinsky (2023) [27]).

Understanding shock-turbulent boundary-layer interactions is fundamental in many application areas, and research on this topic continues from multiple perspectives. From a computational standpoint, there is a need for models that can lower computational cost while still delivering sufficiently accurate results for practical use, thereby avoiding the expense of full DNS. Wall-Modeled Large Eddy Simulation (WMLES) provides a promising approach, although certain disadvantages remain. In particular, for equilibrium wall models (EWM), it is well known that they cannot accurately capture flow separation unless pressure effects are explicitly included. By examining the individual terms in the streamwise momentum equation, the viscous term dominates in the undisturbed equilibrium boundary layer, whereas the pressure-gradient and convective terms become the leading contributions within the interaction and recovery regions. Under such conditions, an equilibrium wall model cannot be expected to yield accurate skin-friction predictions in strongly non-equilibrium flows unless these additional terms are incorporated.
Therefore, it is crucial to develop a compressible framework that can faithfully rep-

resent the thermodynamic variations occurring along a compression ramp, enabling a more effective comparison of the flow evolution with its incompressible counterpart. Van Driest [3] initiated this line of research to understand how to account for variable changes under these conditions across different flow regions.
An important research gap to emphasize involves the low-frequency oscillatory behavior of the shock. The cause of this motion remains unclear, although one plausible explanation is the dynamic interaction among the shock, the separation bubble, and the turbulent boundary layer. Understanding this phenomenon is crucial in STBLI studies because it results in non-stationary peak pressure gradients as well as fluctuating aerodynamic and acoustic loads. The present thesis seeks to apply a WMLES approach to the analysis of an STBLI, focusing on a compression ramp over a smooth surface. Validating the model for a rough-wall configuration is essential in order to better identify its limitations and to explore potential solutions for industrial applications.

2 Theoretical background

In this chapter, the relevant theoretical background is presented. It begins with an analysis of shock wave physics, highlighting the main solutions that are later confirmed by the numerical results. In addition, the governing equations for the boundary layer are described, focusing on the turbulent bounded flow and the compressible approximation.

2.1 Oblique shock wave

The formation of an oblique shock is analyzed for a specific operating condition characterized by a free-stream Mach number of $M = 2.9$ and a ramp angle of $\theta = 24°$, and the resulting flow behavior as it crosses this shock is examined.
A cone with a finite half-angle θ placed in a supersonic free stream with $M_\infty > 1$ can be approximated as an infinitely extended wedge in the spanwise direction, subject to the impermeability condition, which requires that the velocity component normal to the body surface be zero. In the vicinity of the body, the free-stream flow with speed V_∞ is turned through an angle θ, resulting in a finite flow deflection. By decomposing the incoming velocity into two components, u_∞ and w_∞, and further analyzing the relation between c and a_∞, the propagation speeds of a finite-amplitude shock wave and an infinitesimal disturbance can be related as follows:

$$c \geq a_\infty \tag{2.1}$$

$$V_\infty sin(u) = a_\infty \leq c \tag{2.2}$$

In other words, the wave speed c must match u_∞ so that the wave appears stationary in this reference frame. Consider a point located along the direction of V_∞ and observe the behavior as the flow encounters this influence, the flow is turned through an angle θ and then readjusts to become parallel to the body surface, thereby satisfying the tangency condition at the body.

$$sin(\beta) \geq sin(u) \tag{2.3}$$

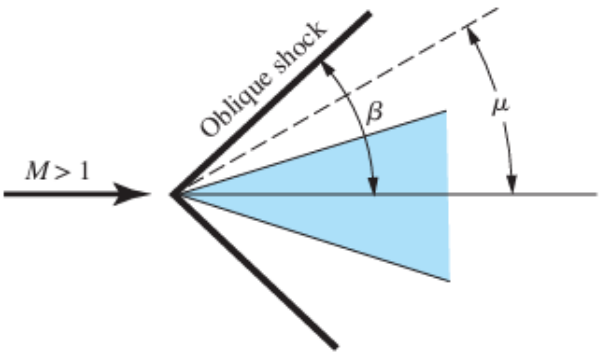

Figure 4: Relation between the oblique shock-wave angle and the Mach angle (John D. Anderson, Jr [23]).

When a shock forms in a supersonic flow, it generates a finite disturbance that must turn the flow through a finite angle. This finite-amplitude disturbance propagates more rapidly than the associated infinitesimal-amplitude wave, so that $\beta \geq u$.
To determine what occurs when a flow crosses an oblique wave, it is first essential to examine the upstream and downstream conditions, using a small control volume whose faces are aligned partly with the shock wave and partly with the flow direction in each region, Fig. 5.
The assumptions are defined as follows:

- $\frac{\partial}{\partial t} = 0$ stationary
- adiabatic
- $\overline{f} = 0$ zero-mass forces
- $\vec{\sum}\hat{n} \simeq 0$ on ∂W: volume edge

+ conditions related to the geometric aspect:

- $u_1 = V_1 sin(\beta)$
- $u_2 = V_2 sin(\beta - \theta)$

2.1.1 Rankine-Hugoniot relations

Given the assumptions adopted to describe the shock wave phenomenon, the equations that characterize the jump conditions in this situation are outlined from the mass and momentum balance relations. The mass conservation B.6 states:

$$\frac{\partial \rho}{\partial t} + \vec{\nabla} \cdot (\rho \vec{V}) = 0, \tag{2.4}$$

then apply the divergence theorem B.1 after having integrated over W

$$\partial W = S_1 \cup S_2 \cup (S_a \cup S_b \cup S_c \cup S_d) \tag{2.5}$$

$$\int_{\partial W} \rho(\vec{V} \cdot \hat{n}) dS \quad \rightarrow \rho_1(-u_1)S_1 + \rho_2(u_2)S_2 = 0 \quad \rightarrow \rho_1 u_1 = \rho_2 u_2. \tag{2.6}$$

Where, by construction, the components of ∂W in brackets are parallel to the flow, the integral is therefore zero since $\vec{V} \cdot \hat{n} = 0$. S_1 and S_2 offset each other because they represent the same surface.
Then, conservation of momentum B.12 implies:

$$\frac{\partial \rho \vec{V}}{\partial t} + \vec{\nabla} \cdot (\rho \vec{V} \vec{V}) = -\vec{\nabla} p + \vec{\nabla} \cdot \vec{\sum}, \tag{2.7}$$

and considering $-\vec{\nabla} p = -\vec{\nabla} \cdot (p\vec{\vec{I}})$, It is possible to integrate and apply the divergence theorem here as well:

$$\int_{\partial W} \rho \vec{V} (\vec{V} \cdot \hat{n}) dS + \int_{\partial W} p \hat{n} dS = \int_{\partial W} \vec{\sum} \cdot \hat{n} dS \tag{2.8}$$

Here, $\vec{\sum} \cdot \hat{n}$ vanishes by assumption, and it should be noted that the surfaces $S_a \cup S_c$ belong to the upstream region, while $S_b \cup S_d$ are located in the downstream region, cancel out because we have the same p with opposite $\hat{n}$.
Along the normal direction $\hat{n}$:

$$\rho_1 u_1(-u_1)S_1 + \rho_2(u_2)^2 S_2 - p_1 S_1 + p_2 S_2 = 0 \quad \rightarrow \rho_1(u_1)^2 + p_1 = \rho_2(u_2)^2 + p_2. \tag{2.9}$$

Where $-u_1$ refers to the integral over S_1 and, as before, the surfaces cancel out with each other.
Tangential direction to the wave $\hat{z}$:

$$\rho_1 w_1(-u_1)S_1 + \rho_2(w_2)^2 S_2 = 0 \quad \rightarrow (\rho_1 u_1)w_1 = (\rho_2 u_2)w_2 \quad \rightarrow w_1 = w_2 \tag{2.10}$$

Note that the pressure does not contribute here because $\hat{n_1}$ and $\hat{n_2}$ are orthogonal. The result shows the conservation of the tangential component of the wave. Regarding energy, the relation for the total enthalpy states:

$$h_{0,1} = h_{0,2} \quad \rightarrow h_1 + \frac{V_1^2}{2} = h_1 + \frac{V_2^2}{2} \quad \rightarrow h_1 + \frac{u_1^2 + w_1^2}{2} = h_2 + \frac{u_2^2 + w_2^2}{2} \tag{2.11}$$

Then

$$h_1 + \frac{u_1^2}{2} = h_2 + \frac{u_2^2}{2} \tag{2.12}$$

leading conservation of sensible enthalpy and the squared velocity component.
Eq. 2.6, 2.9, and 2.12 are known as the Rankine-Hugoniot relations for the description of the shock wave jump conditions.
To visualize the phenomenon, analyze the representation in Fig.6, which shows what happens in terms of angles and velocity components for a flow encountering an oblique shock wave with an inclination β. To establish the relationship that allows

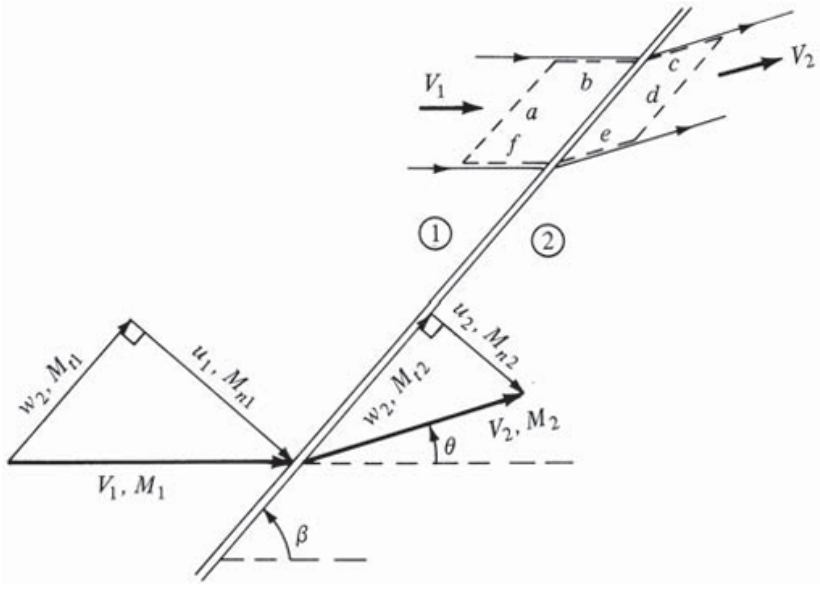

Figure 5: Oblique shock geometry(John D. Anderson, Jr [23]).

us to evaluate the quantities between two regions associated with the formation of a shock wave, it is essential first to define the normal Mach number Mn:

$$Mn_1 = \frac{u_1}{a_1} = \frac{V_1 sin(\beta)}{a_1} = M_1 sin(\beta) \tag{2.13}$$

$$Mn_2^2 = \frac{1 + \frac{\gamma-1}{2} Mn_1^2}{\gamma Mn_1^2 - \frac{\gamma-1}{2}} = \frac{1 + \frac{\gamma-1}{2} M_1^2 sin(\beta)^2}{\gamma M_1^2 sin(\beta)^2 - \frac{\gamma-1}{2}} \leq 1 \tag{2.14}$$

where the subindex refers to the upstream, 1, and downstream, 2, shock region. Mn_2^2 is subsonic, while the one upstream of the shock is supersonic.
In the end, the system of equations that connects the regions is given by:

$$\frac{\rho_2}{\rho_1} = \frac{u_1}{u_2} = \frac{(\gamma+1)Mn_1^2}{\gamma Mn_1^2 - \frac{\gamma-1}{2}}, \qquad \frac{p_2}{p_1} = 1 + \frac{2\gamma}{\gamma+1}(Mn_1^2 - 1), \qquad \frac{T_2}{T_1} = \frac{P_2/P_1}{\rho_2/\rho_1} \tag{2.15}$$

Recalling how Mn_2 can be expressed as Mn_1, then:

$$Mn_2 = \frac{u_2}{a_2} = \frac{V_2 sin(\beta-\theta)}{a_2} = M_2 sin(\beta-\theta) \tag{2.16}$$

To calculate the downstream Mach number M_2 after the shock wave, it is essential to know the values of β and θ.

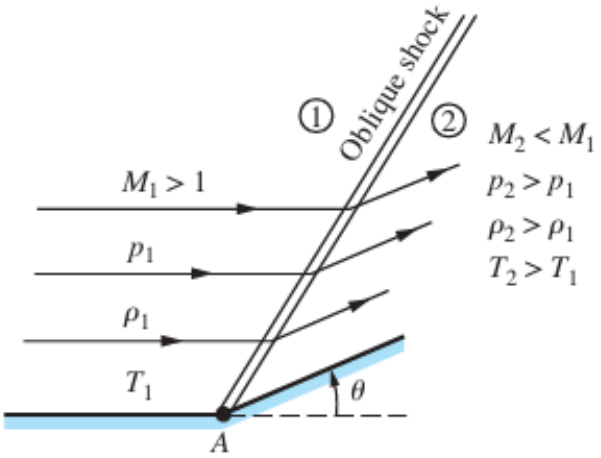

Figure 6: Supersonic flow over a corner (John D. Anderson, Jr [23]).

2.1.2 $\theta - \beta - M$ relation

It is possible to establish a relation between θ, the inclination angle of the object under analysis, β, the inclination angle of the shock wave, and M, the Mach number. This relation is essential for predicting the possible configurations based on the known values of M_1, the upstream Mach number, and θ:

$$\frac{u_1}{w_1} = tan(\beta), \qquad \frac{u_2}{w_2} = tan(\beta-\theta) \tag{2.17}$$

By using the relation $\frac{\rho_2}{\rho_1} = \frac{u_1}{u_2}$, we can derive the following expression:

$$\frac{\rho_2}{\rho_1} = \left(\frac{u_1}{w_1}\right)\left(\frac{w_2}{u_2}\right) = \frac{tan(\beta)}{tan(\beta-\theta)} = \frac{(\gamma+1)\overbrace{M_1^2 sin(\beta)^2}^{Mn_1^2}}{2 + (\gamma+1)\underbrace{M_1^2 sin(\beta)^2}_{Mn_1^2}} \tag{2.18}$$

$\theta - \beta - M$ relation states:

$$tan(\theta) = 2cot(\beta) \cdot \frac{(M_1^2 sin(\beta)^2 - 1)}{M_1^2(\gamma + cos(2\beta)) + 2} \tag{2.19}$$

The graph of the relation C, displays two distinct branches. For each value of θ, there exist two corresponding solutions:

- a strong solution, denoted by β_s,
- a weak solution, denoted by β_w.

Regarding the intensity of the shock, there is a condition in which $\beta_s = \beta_w$, that is, when the maximum deflection for that upstream Mach number is set: $\theta_{MAX}^{M_1}$. It is important to highlight that, in the supersonic regime, there is a range before $\theta_{MAX}^{M_1}$ in which the downstream flow is still subsonic even with β_w, so there will be a value of θ for which $M_2 = 1$.
A simple case to consider is when $\theta = 0$: the flow does not undergo any deflection as it passes through the wave, but we still have two solutions:

1. $cot(\beta) = 0 \rightarrow \beta = \frac{\pi}{2}$, when the shock wave is orthogonal to the undisturbed flow, and the oblique shock becomes a normal shock.
2. $M_1^2 sin(\beta)^2 = 1 \rightarrow sin(\beta) = \frac{1}{M_1} = sin(u) \rightarrow \beta = u$, the oblique shock becomes a Mach wave, with infinitesimal strength and an angle given by β.

The discussion of the case under consideration can be extend to a ramp, with $\overline{\theta} < \theta_{\mathrm{MAX}}^{M_{1,A}}$. Among the two solutions, the one that usually occurs is the weak one. The strong one occurs in the curved shock case, Fig.7.
The difference between the solutions is due to the fact that what matters is Mn_1 and not M_1, therefore:

$$\beta_s > \beta_w \rightarrow \sin(\beta_s) > \sin(\beta_w) \rightarrow Mn_1^s > Mn_1^w \tag{2.20}$$

With a weak shock, an enthalpy saving in the flow deflection occurs. Then, in the strong case, high values of pressure downstream are present.
Downstream of the oblique shock, a flow might be sonic, subsonic, or supersonic. The entire branch of the β_s solutions has solutions with $M_2 < 1$, while the weak branch, β_w, almost always has solutions with $M_2 > 1$:

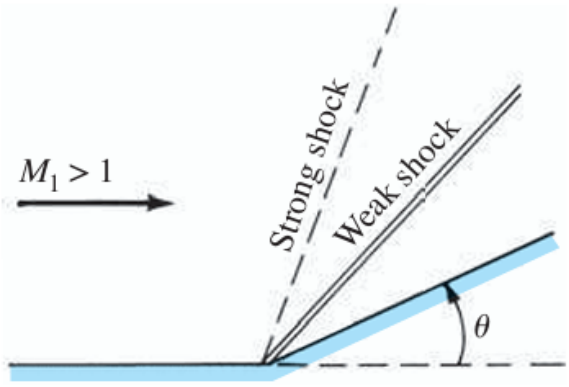

Figure 7: The weak and strong shock cases: $\theta < \theta_{MAX}$ (John D. Anderson, Jr [23]).

2.2 Wall-bounded turbulent flow

Most turbulent flows arise in environments that involve one or more solid surfaces. Typical examples include internal flows, like those found in pipes and ducts, as well as external flows, such as those past aircraft and ship hulls.
For the wall-bounded turbulent theoretical analysis, a steady flow between two parallel plates separated by a fixed distance is considered. In our case, the flow is developed only on the lower side of the wall.

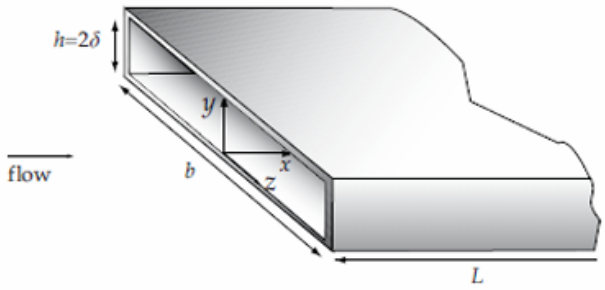

Figure 8: Sketch of a channel flow (Pope [9]).

The setup considered for the description of a turbulent channel flow is defined by the distance between the two walls as 2δ, and the stream-wise L_x and span-wise L_z dimensions are much larger than the wall-normal one. So, the Reynolds averaged velocity statistics B.6 do not depend on x, z, and t. In general, the average velocity has three components:

$$\langle U \rangle = \begin{pmatrix} u \\ v \\ w \end{pmatrix} \tag{2.21}$$

where $w = 0$ for the construction, and the mean velocity field is represented by a vector field that depends solely on y, varying along the gap between the two plates.

$$\langle \vec{U} \rangle = \langle \vec{U}(y) \rangle \tag{2.22}$$

Then the Reynolds number is defined as follows:

$$Re = \frac{U_0 2\delta}{\nu} \tag{2.23}$$

where:

- U_0 is the bulk velocity in the section, defined as:

$$U_0 = \frac{1}{2\delta} \int_0^{2\delta} \langle U(y) \rangle dy \tag{2.24}$$

- δ is the channel half width.
- ν is the kinematic viscosity.

Assuming a sufficiently large Reynolds number to ensure turbulent flow conditions and starting from the RANS equations, B.6, by exploiting the symmetry of the problem and the impermeability boundary condition, the conservation of mass states that:

$$\langle V \rangle = 0 \tag{2.25}$$

The average normal velocity is zero for all y. Then the y-component of the momentum equation reduces to:

$$\langle p \rangle + \rho \langle v'^2 \rangle = p_w(x) \tag{2.26}$$

where $\langle v'^2 \rangle$ represents the fluctuation of the wall-normal velocity component and $p_w(x)$ is the wall pressure, which depends only on x. By differentiating all terms with respect to x, it is possible to obtain:

$$\frac{\partial p}{\partial x} = \frac{dp_w}{dx}(x) \tag{2.27}$$

and thus the x-component of the momentum equation becomes:

$$\frac{dp_w}{dx} = \frac{d}{dy}\left[\tau(y)\right] \tag{2.28}$$

where $\tau(y)$ is the mean shear stress, and it is defined as follows:

$$\tau(y) = \underbrace{p\frac{d\langle U \rangle}{dy}}_{viscous\ stress} - \underbrace{\rho \langle u' v' \rangle}_{turbulent\ Reynolds\ stress} \tag{2.29}$$

Since the left-hand side of Eq. 2.28 depends on x, while the right-hand side depends on y, the only way to satisfy the equation is for both to be equal to the same constant value, i.e. $f(x) = \tau(y) = a$, where a is a constant. Therefore, in order to define the constant value:

$$\frac{d}{dy}\left[\tau(y)\right] = a \tag{2.30}$$

$$\tau(y=0) = \mu \frac{d\langle U \rangle}{dy}\bigg|_{y=0} - \rho \langle u' v' \rangle\bigg|_{y=0} = \mu \frac{d\langle U \rangle}{dy}\bigg|_{y=0} = \tau_w \tag{2.31}$$

Here, τ_w denotes the mean wall shear stress in the lower section. Because $\tau(y)$ is antisymmetric about the mid-plane, it follows that in the case of top wall stress, this can be defined as $\tau(y = 2\delta) = -\tau_w$. The value of the constant required to solve this problem is:

$$a = \frac{-\tau_w}{\delta} \tag{2.32}$$

Based on this result, the expression for the mean shear stress becomes:

$$\tau(y) = \tau_w \left(1 - \frac{y}{\delta}\right) \tag{2.33}$$

Consequently, the key outcome is the equilibrium between the mean shear flow and the pressure gradient in the x-direction:

$$\tau_w = -\frac{dp_w}{dx}\delta \tag{2.34}$$

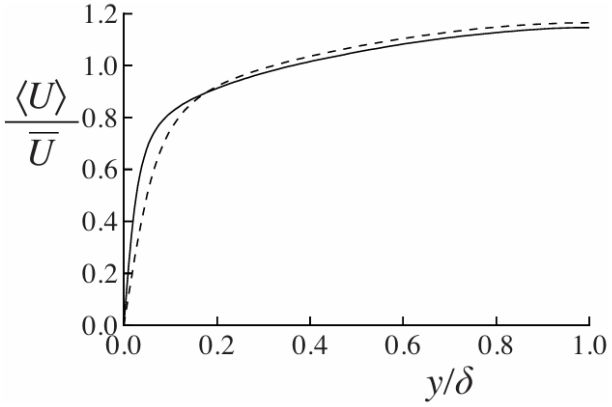

Figure 9: Mean velocity profiles in fully developed turbulent channel flow from the DNS of Kim et al. (1987): dashed line, Re = 5,600; solid line, Re = 13,750.(Pope [9]).

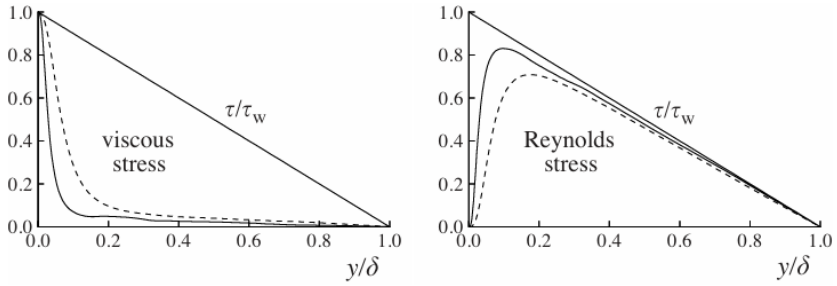

Figure 10: Profiles of the viscous shear stress, and the Reynolds shear stress in turbulent channel flow: DNS data of Kim et al. (1987): dashed line, Re = 5,600; solid line, Re = 13,750. (Pope [9]).

According to Fig. 9, the velocity gradient at the wall increases as the Reynolds number rises. Regarding Fig. 10, with increasing Reynolds number, the viscous shear stress becomes dominant in a region close to the wall, while the Reynolds stress grows more significant farther from the wall. Thus, it is possible to distinguish two separate regions:

1. inner region where viscous shear stresses prevail,
2. an outer region where Reynolds turbulent stresses are predominant.

The following observations are conducted when the Reynolds number increases, as shown in the figure.

- $\tau_w = \mu \frac{\partial U}{\partial y}\Big|_{y=0}$ increases, so the velocity gradient at the wall increases.
- $-\rho\langle u' v' \rangle$ the Reynolds stress increases far from the wall.
- $\tau = \mu \frac{\partial U}{\partial y}$ becomes more dominant in the near-wall region.

According to this, the characteristic values for velocity and length are defined.

For the internal region, where $y << \delta_\nu$ or $y^+ << 1$:

- friction velocity

$$u_\tau = \sqrt{\frac{\tau_w}{\rho}} \tag{2.35}$$

- viscous length

$$\delta_\nu = \frac{\nu}{u_\tau} = \frac{\mu}{\rho u_\tau} \tag{2.36}$$

For the external region $y >> \delta_\nu$ or $y^+ >> 1$, the characteristic velocity and length are respectively u_τ and δ.
To describe the velocity profile through these regions, it is necessary to define the friction Reynolds number, Re_τ:

$$Re_\tau = \frac{\delta}{\delta_\nu} = \frac{\delta u_\tau}{\nu} \tag{2.37}$$

2.2.1 Mean velocity profiles

Starting from the condition of impermeability set for the mean velocity in the internal region, when $y/\delta << 1$, it is possible to describe the profile using a Taylor expansion:

$$\langle U(y)\rangle = \langle U(y)\rangle + \left.\frac{d\langle U\rangle}{dy}\right|_{y=0} y + O(y^2) \tag{2.38}$$

Then, dividing Eq. 2.38 by the friction velocity u_τ and multiplying and dividing the right hand side by the viscous length scale δ_ν, the wall coordinate $y^+ = \frac{y}{\delta_\nu}$, and the dimensionless velocity u^+ are introduced:

$$\frac{\langle U(y)\rangle}{u_\tau} = u^+ = \delta_\nu \frac{1}{u_\tau}\left.\frac{d\langle U\rangle}{dy}\right|_{y=0} y^+ + O(y^2) \tag{2.39}$$

The right hand side of Eq. 2.39 becomes as follows, considering Eq. 2.34 and 2.36:

$$\left.\frac{\delta_\nu}{u_\tau}\frac{d\langle U\rangle}{dy}\right|_{y=0} = \left.\frac{\nu}{u_\tau^2}\frac{d\langle U\rangle}{dy}\right|_{y=0} = \left.\frac{\mu}{\rho u_\tau^2}\frac{d\langle U\rangle}{dy}\right|_{y=0} = \frac{1}{\tau_w}\tau_w = 1 \tag{2.40}$$

The obtained results indicate that the profile in the vicinity of the wall exhibits a linear behavior

$$u^+ = y^+. \tag{2.41}$$

The near-wall region corresponding to $0 \leq y^+ \leq 5$ is referred to as the viscous sub-layer (VSL). Using the definition of wall-normal distance in viscous units,

$$y^+ = \frac{y}{\delta_\nu} = \frac{\mu_\tau\, y}{\nu} \tag{2.42}$$

one can observe that y^+ behaves similarly to a local Reynolds number. Its magnitude indicates the relative significance of viscous and turbulent processes. Figure 11 presents the fractional contributions of viscous and Reynolds stresses to the total stress in the near-wall region of channel flow. When these contributions are plotted as functions of y^+, the profiles corresponding to the two Reynolds numbers nearly

coincide. The viscous contribution decreases from 100% at the wall to 50% at $y^+ \approx 12$, and falls below 10% by $y^+ = 50$. A fully developed channel flow is completely specified by ρ, ν, δ, and dp_w/dx or u_τ as seen:

$$u_\tau = \left(-\frac{\delta}{\rho} \frac{dp_w}{dx} \right)^{1/2} \tag{2.43}$$

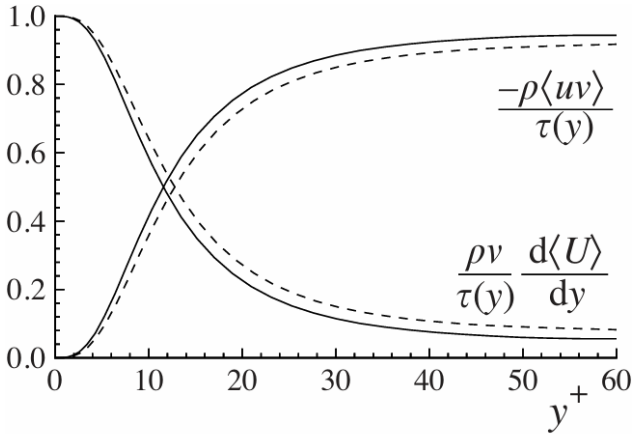

Figure 11: Profiles of the fractional contributions of the viscous and Reynolds stresses to the total stress. DNS data of Kim et al. (1987): dashed lines, Re = 5,600; solid lines, Re = 13,750. (Pope [9]).

Based on the value of y^+, the near-wall flow can be divided into distinct regions:

1. The viscous wall region, where $y^+ < 50$, molecular viscosity directly influences the shear stress.

2. In the outer region with $y^+ > 50$, the direct influence of viscosity on the flow becomes negligible.

There are two independent non-dimensional groups that can be formed by these variables and the y coordinate (e.g., y/δ and $Re_\tau = u_\tau \delta/\nu$), and consequently, the mean velocity profile can be written as follows:

$$\langle U \rangle = u_\tau F_0 \left(\frac{y}{\delta}, Re_\tau \right) \tag{2.44}$$

where F_0 is a universal non-dimensional function to be determined. Since the gradient is the dynamically relevant quantity in both the definition of viscous stress and turbulence production, it is preferable to focus on the velocity gradient $d\langle U \rangle/dy$ rather than on $\langle U \rangle$ itself.
On dimensional grounds, $d\langle U \rangle/dy$ depends on just two non-dimensional parameters, so that:

$$\frac{d\langle U \rangle}{dy} = \frac{u_\tau}{y} \Phi \left(\frac{y}{\delta_\nu}, \frac{y}{\delta} \right) \tag{2.45}$$

where Φ is a universal non-dimensional function. The rationale for choosing these two parameters is that δ_ν represents the relevant length scale in the viscous near-wall region ($y^+ < 50$), whereas δ characterizes the outer region ($y^+ > 50$).

The relationship

$$Re_\tau = \frac{y/\delta_\nu}{y/\delta} \tag{2.46}$$

indicates that the pair (δ_ν, δ) conveys the same information as the variables y/δ and Re_τ, 2.44. According to [1], in the inner layer, where the mean velocity profile is governed by viscous scaling, the function $\Phi(y/\delta_\nu, y/\delta)$ tends, in the limit, to a function that depends only on y/δ_ν:

$$\frac{d\langle U\rangle}{dy} = \frac{u_\tau}{y}\,\Phi_I\left(\frac{y}{\delta_\nu}, \frac{y}{\delta}\right) \tag{2.47}$$

with

$$\Phi_I\left(\frac{y}{\delta_\nu}\right) = \lim_{y/\delta\to 0}\Phi\left(\frac{y}{\delta_\nu}, \frac{y}{\delta}\right) \tag{2.48}$$

By introducing $y^+ = y/\delta_\nu$ and the non-dimensional velocity $u^+(y^+)$, Eq. 2.47 can be used to derive the law of the wall:

$$u^+ = f_w(y^+) \tag{2.49}$$

where

$$f_w(y^+) = \int_0^{y^+} \frac{1}{y^+}\,\Phi_I(y^+)\,dy^+\,. \tag{2.50}$$

The form of the function $f_w(y^+)$ can be established for both small and large values of y^+. In this way, it becomes possible to identify the different layers that characterize the phenomenon under analysis, Table 1.

Region	Location	Properties
Inner layer	$y/\delta < 0.1$	$\langle U\rangle$ determined by u_τ and y^+, independent of U_0 and δ
Viscous wall region	$y^+ < 50$	The viscous contribution to the shear stress is significant
Viscous sublayer	$y^+ < 5$	The Reynolds shear stress is negligible compared to the viscous stress
Buffer layer	$5 < y^+ < 30$	Region between the viscous sublayer and the log-law region
Log-law region	$y^+ > 30$, $y/\delta < 0.3$	The log-law holds in this region

Table 1: Wall regions and layers with their defining properties.

Hence, in Eq. 2.47, the dependence of $\Phi_I(y/\delta_\nu)$ on ν through δ_ν vanishes, so that Φ_I adopts a constant value denoted by k^{-1}:

$$\Phi_I(y^+) = \frac{1}{k}, \quad \text{for} \quad \frac{y}{\delta} << 1 \quad \text{and} \quad y^+ >> 1 \tag{2.51}$$

Thus, in this region, the mean velocity gradient is given by

$$\frac{du^+}{dy^+} = \frac{1}{ky^+} \tag{2.52}$$

which, upon integration, yields the logarithmic law of the wall, or simply the log-law, originally proposed by von Kármán [2]:

$$u^+ = \frac{1}{k} \ln y^+ + B, \tag{2.53}$$

where B is an additive constant and k is the von Kármán constant. Reported values of these log-law parameters show some variation in the literature, but they typically lie within about 5% of

$$k = 0.41, \qquad B = 5.2 \tag{2.54}$$

The layer between the viscous sublayer ($y^+ < 5$) and the logarithmic region ($y^+ > 30$) is termed the buffer layer. This is a transitional zone between the viscosity-dominated and turbulence-dominated parts of the flow.
Because of the self-sustaining turbulence cycle active there, no simple, universally accepted analytical law describes the velocity distribution in this layer.
The different regions and layers commonly used to characterise near-wall turbulent flows are summarised in Fig. 12.

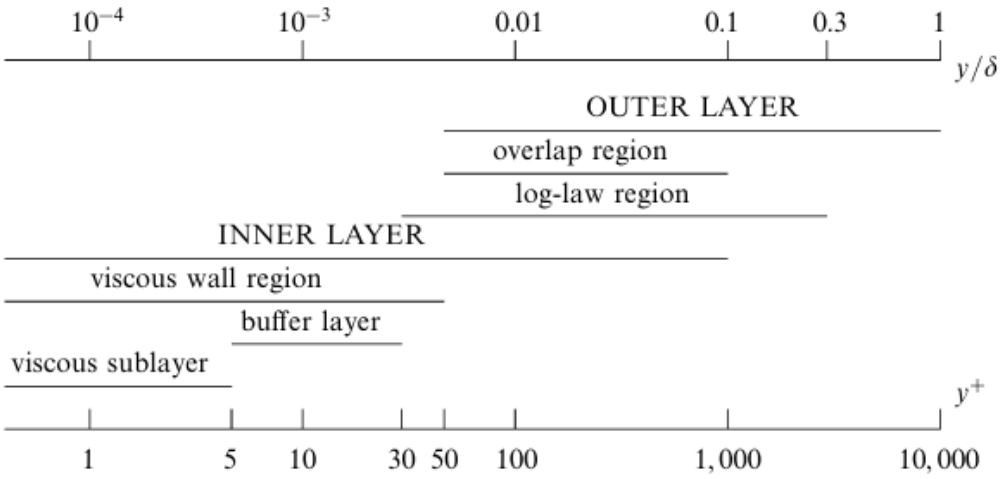

Figure 12: Schematic of the various wall regions and layers, expressed in terms of $y^+ = y/\delta_\nu$ and y/δ, for turbulent channel flow at high Reynolds number, $Re_\tau = 10^4$ (Pope [9]).

2.3 Turbulent boundary layer

The Navier-Stokes equations, B, form the mathematical foundation for describing compressible flows. For a generic flow variable ϕ, statistical analysis relies on an averaging procedure that splits the variable into a mean component $\overline{\phi}$ and a fluctuating component ϕ':

$$\phi = \overline{\phi} + \phi'. \tag{2.55}$$

This operation, known as Reynolds decomposition, is reported in B.6.
In the context of compressible flows, an alternative averaging procedure is often adopted because its properties facilitate the manipulation of the averaged Navier-Stokes equations: the density-weighted, or Favre, average. The Favre average is defined as:

$$\overline{\phi} = \frac{\overline{\rho\phi}}{\overline{\rho}}, \tag{2.56}$$

while its fluctuating part is denoted by ϕ'', such that $\phi = \overline{\phi} + \phi''$. Both Reynolds and Favre decompositions can be replaced by a filtering procedure, which is, for instance, used in Large Eddy Simulations [18].

2.3.1 Incompressible boundary layer

According to the information highlighted in Section 2.2, the plate surface is located at the wall-normal coordinate $y = 0$, where the flow velocity vanishes due to the no-slip boundary condition. The flow is statistically homogeneous in the spanwise direction z.
Outside the boundary layer, the streamwise velocity reaches a uniform value u_∞, under the assumption of a zero-pressure-gradient condition, $dp_\infty/dx = 0$. The boundary layer thickness $\delta(x)$ [9] is generally identified as the wall-normal position where the mean streamwise velocity attains 99% of its free-stream value, commonly denoted by δ_{99}, Fig. 13. This is a poorly conditioned quantity, since it depends on the measurement of a small velocity difference; integral measures are more reliable, such as the displacement thickness

$$\delta^*(x) = \int_0^\infty \left(1 - \frac{\overline{\rho u}}{\rho_\infty u_\infty}\right) dy, \tag{2.57}$$

or the momentum thickness

$$\theta(x) = \int_0^\infty \frac{\overline{\rho u}}{\rho_\infty u_\infty}\left(1 - \frac{\overline{u}}{u_\infty}\right) dy, \tag{2.58}$$

where $\overline{\rho u}$ denotes the average velocity and $\rho_\infty u_\infty$ the free-stream velocity.
The classical Reynolds number $Re_\theta = \rho_\infty u_\infty \theta/\mu_\infty$ is defined starting from the momentum thickness; otherwise, it can be built based on other characteristic lengths, such as the displacement thickness δ^* or the 99% boundary-layer thickness δ_{99}.
All of these are representative of the largest turbulent scales present within the boundary layer.
However, these scales do not describe the inner region of the boundary layer, where viscous effects become increasingly dominant. This is even more pronounced in compressible boundary layers, in which thermodynamic properties change significantly from the freestream to the wall. Different layers can be defined within the main

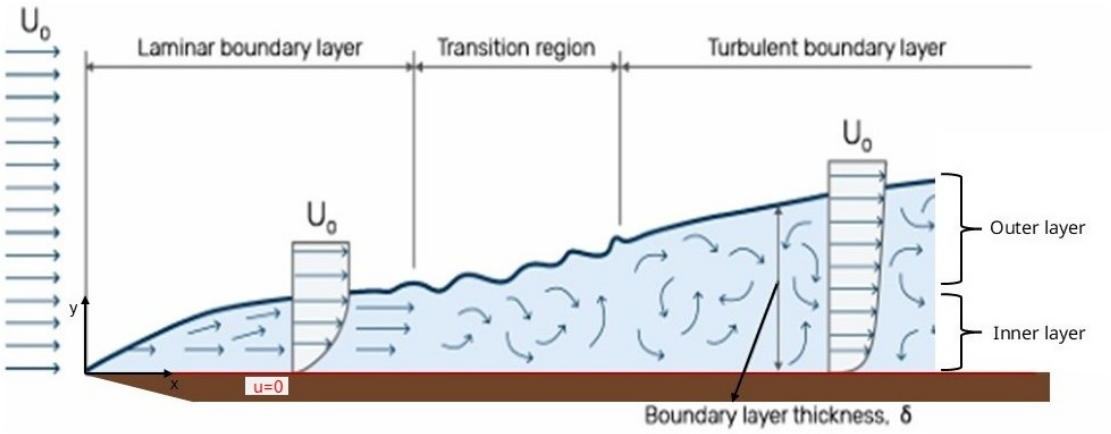

Figure 13: Development of the boundary layer from the laminar to the turbulent region.

boundary layer by physical considerations on the dominating terms of averaged N-S.

It is worth considering the following transformations in order to define the internal solution for the boundary layer. Therefore, the scope is to apply a change in coordinates with L and δ as reference lengths for the x and y directions, respectively:

- $x' = \frac{x}{L_\infty} = x^*$
- $dx' = dx^*$
- $y' = \frac{y}{\delta} = \frac{y}{L_\infty} \cdot \frac{L_\infty}{\delta} = y^* \sqrt{Re}$
- $dy' = \sqrt{Re} dy^*$
- $u' = \frac{u}{U_\infty} = u^*$
- $v' = \frac{v}{V_\infty} = \frac{v}{U\infty} \cdot \frac{U_\infty}{V_\infty} = v^* \sqrt{Re}$
- $p' = p^*$

For high Reynolds numbers, $Re \to \infty$, the boundary layer equations, considering only continuity and momentum conservation, become:

$$\frac{\partial u'}{\partial x'} + \frac{\partial v'}{\partial y'} = 0 \tag{2.59a}$$

$$u' \frac{\partial u'}{\partial x'} + v' \frac{\partial u'}{\partial y'} = -\frac{\partial p'}{\partial x'} + \frac{\partial^2 u'}{\partial y'^2} \tag{2.59b}$$

The first boundary condition is the one related to the boundary layer pressure p:

$$\lim_{y' \to \infty} p'(x') = \lim_{y^* \to 0} p_e^*(x^*, y^*) = p_{e,0}^*(x^*) = p_{e,0}'(x') \tag{2.60}$$

Then, the other two boundary conditions are:

- $y' = 0$, $u' = v' = 0$ impermeability condition,
- $y' = \infty$, $u' \to 1$ asymptotic matching.

For our analysis, it is also worth considering what happens to the solution of the boundary layer over the wall, $y' = 0$

$$\frac{dp_{e,0}^*}{dx} = \frac{\partial^2 u'}{\partial y'^2} \tag{2.61}$$

1. For $dp^*_{e,0}/dx = 0$, the velocity profile starts with an inflection point and approaches the external flow solution asymptotically. This corresponds to the classical Blasius boundary-layer solution.

2. For $dp^*_{e,0}/dx < 0$, the flow accelerates under a favorable pressure gradient. The profile exhibits increased concavity and again tends asymptotically toward the external solution. The near-wall region becomes thicker: the wall shear stress τ_w rises, while the boundary-layer thickness δ is reduced.

3. For $dp^*_{e,0}/dx > 0$, an adverse pressure gradient is present, and the velocity profile bends downward toward the wall. The curvature reverses sign and the inflection point lies inside the boundary layer; the profile has less momentum close to the wall and therefore appears thinner. Under these conditions, τ_w decreases, causing the boundary layer thickness δ to grow.

4. For $dp^*_{e,0}/dx \gg 0$, the adverse pressure gradient is highly intense, leading to $du'/dy'|_{y'=0} = 0$. In this case, the wall shear stress becomes $\tau_w = 0$, and the boundary layer thickness δ increases even more significantly.

The condition 4 is referred to as incipient separation, after which the boundary layer separates, creating a recirculation zone. The concavity of the mean velocity profile is reversed, indicating that the velocity vectors are oriented in the opposite direction (counter flow) compared to the external flow solution. Beyond the separation zone, it is no longer valid to consider a thin boundary layer of thickness δ: the usual boundary layer approximation fails because a large wake region with significant vorticity is now present.

2.3.2 Compressible boundary layer

Compressible flows are characterized by locally variable thermodynamic properties, such as temperature and density, which can alter the applicability of some theoretical laws developed for their incompressible counterparts. In fact, the agreement of a compressible mean velocity profile with the laws depicted would progressively degrade as the Mach number increases, especially in the log-layer.
Van Driest (1956) [3] proposed a compressibility transformation, considering that in the log-layer, turbulent stresses are in equilibrium with the total shear stress; therefore, the eddy viscosity is defined as $\mu_t = \overline{\rho} l^2 \partial\overline{u}/\partial y$, where $l = ky$ is the mixing length, in a more appropriate way. The average density $\overline{\rho} = f(y)$ has been used instead of its value at the wall ρ_w:

$$\sqrt{\frac{\overline{\rho}}{\rho_w}}\frac{\partial \overline{u}}{\partial y} = \frac{u_\tau}{ky}. \tag{2.62}$$

Because the density also varies with y, it cannot be directly integrated to yield a logarithmic law. Instead, the goal is to obtain a rescaled form of the mean velocity profile

$$\frac{\partial \overline{u}_{VD}}{\partial y} = \sqrt{\frac{\overline{\rho}}{\rho_w}}\frac{\partial \overline{u}}{\partial y}, \quad \overline{u}_{VD} = \int_0^u \sqrt{\frac{\overline{\rho}}{\rho_w}} d\overline{u}, \tag{2.63}$$

which is the Van Driest transformed velocity. In practice, the Van Driest (1956) transformation was found to be accurate only up to supersonic speeds $M_\infty \approx 2$ and

only for adiabatic walls. This can be attributed to the physical inconsistency of arguments derived specifically for the log-layer, which do not hold in the viscous sublayer where diabatic effects are strongest. In fact, this region is dominated by viscous stresses, with a strong damping of turbulent fluctuations.
The main aspect in which high-speed compressible boundary layers differ from the incompressible ones is that the momentum and thermal fields are strongly coupled through the density. The dependence of viscosity and thermal conductivity on temperature makes the physics even more complex, promoting the exchange of momentum and heat between different regions of the flow. As it is slowed by viscous effects within the boundary layer, the kinetic energy carried by the flow is converted into thermal energy, resulting in high temperatures and chemical dissociation. Considering the stagnation enthalpy h_0, A, for a calorically perfect gas, a law can be derived:

$$T_0 = T_\infty + \frac{u_\infty^2}{2c_p} = T_\infty(1 + \frac{\gamma - 1}{2} M_\infty^2), \tag{2.64}$$

In compressible boundary layers, although the flow is brought to rest at the wall, nonisentropic processes are present and tend to settle to a slightly lower temperature. The adiabatic wall temperature, T_{aw}, as obtained using a recovery factor, is also indicated.

$$r = \frac{T_{aw} - T_\infty}{T_0 - T_\infty} = \frac{2}{(\gamma - 1)M_\infty^2} \left(\frac{T_w}{T_\infty} - 1 \right). \tag{2.65}$$

In turbulent flows, it becomes approximated by $Pr^{1/3}$, Van Driest (1956) [3]. From the recovery factor, we can define a recovery temperature as

$$T_{aw} = T_r = T_\infty \left(1 + r \frac{\gamma - 1}{2} M_\infty^2 \right). \tag{2.66}$$

Normally, the solid wall is much colder than the adiabatic wall temperature, and thermal equilibrium with the fluid is expected to be reached with much longer time scales than those related to a specific flow regime. Consequently, a finite heat flux q_w is transferred from the flow to the solid wall, acting as the primary mechanism behind viscous aerodynamic heating. The competition between the fluid's tendency to attain the adiabatic wall temperature T_{aw} and the actual wall temperature T_w leads to a local peak in the static temperature distribution.

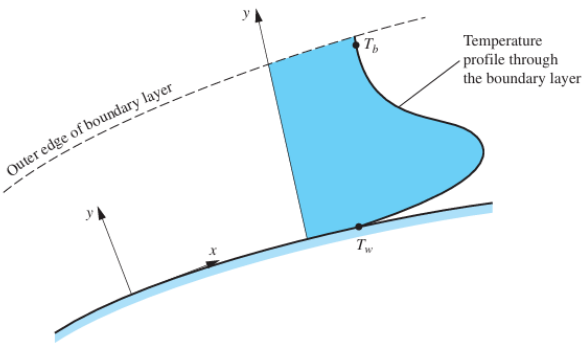

Figure 14: Temperature profile through a boundary layer. $T_b = T_\infty$ the outer edge temperature of the profile. Condition with $T_w < T_{aw}$ means $q_w > 0$, (John D. Anderson, Jr [23]).

3 Numerical methodology

In this section, an overview of turbulence modeling approaches is presented to highlight the differences from the model solution adopted for this case study. Then, a description of the solver and the setup used is provided.

3.1 Turbulence modeling approaches

Numerical simulations are necessary to investigate the Navier-Stokes equations, B, for describing turbulence, which is a chaotic, non-stationary, and multiscale phenomenon.

- DNS: Direct Numerical Simulation method resolves all the physical processes involved in turbulence, therefore the computational cost increases significantly. However, the high-fidelity representation of the flow makes the simulation comparable in value to an experiment. To assess the computational cost of DNS, it is necessary to rely on Richardson's phenomenological theory and Kolmogorov's formal $K41$ framework. Therefore, the number of grid points in e ach direction is proportional to the ratio between the integral scale L and the Kolmogorov scale η. The turbulent kinetic energy dissipation rate is known to be proportional to a characteristic length of the integral scale: $\epsilon \propto U^3/L$, while the Kolmogorov scale depends only on the dissipation and the kinematic viscosity: $\eta = (\nu^3/\epsilon)^{1/4}$.

$$N_x = \frac{L_x}{\Delta_x} \propto \frac{L}{\eta} = \frac{L}{(\nu^3/\epsilon)^{1/4}} \propto \left(\frac{L^4 U^3}{L\nu^3}\right)^{1/4} = Re^{3/4} \tag{3.1}$$

  The estimate for all three spatial directions is $N \propto Re^{9/4}$. From the standpoint of time resolution, it is essential to account for the temporal discretization of the problem. The time step must be small enough to resolve the Kolmogorov time scale τ_η. Denoting by $T = L/U$ the characteristic large-scale time, the required number of time steps is

$$N_t \propto \frac{T}{\tau_\eta} = Re^{1/2}. \tag{3.2}$$

  Consequently, the total simulation time T_{tot}, which scales with the Reynolds number, is

$$T_{tot} \propto (N \times N_t) \propto Re^{11/4} \approx Re^3. \tag{3.3}$$

  This constraint limits the applicability of DNS to relatively low Re values in order to prevent prohibitive computational costs. Nonetheless, a key advantage of direct numerical simulation is the high quality and large amount of data it provides at every time instant for the full velocity vector field at each point in the domain.

- RANS: The Reynolds-Averaged Navier-Stokes method is a numerical approach that relies on the evolution of the mean velocity and on the ability to relax the constraints on spatial fluctuations, even at small scales (η), to obtain a grid path determined by the gradients of the mean field. The flow quantities

are decomposed into their time-averaged and fluctuating components. Based on the Favre average, RANS final form can be written as:

$$\frac{\partial \overline{\rho}}{\partial t} + \frac{\partial(\overline{\rho u_j})}{\partial x_j} = 0, \tag{3.4a}$$

$$\frac{\partial(\overline{\rho}\,\overline{u_i})}{\partial t} + \frac{\partial}{\partial x_j}\left(\overline{\rho}\,\overline{u_i}\,\overline{u_j}\right) = -\frac{\partial \overline{p}}{\partial x_i} + \frac{\partial}{\partial x_j}\left(\overline{\sigma_{ij}} - \overline{R_{ij}}\right), \tag{3.4b}$$

$$\frac{\partial(\overline{\rho}\,\overline{E})}{\partial t} + \frac{\partial}{\partial x_j}\left(\overline{\rho}\,\overline{u_j}\overline{H}\right) = -\frac{\partial}{\partial x_j}(\overline{u_i \sigma_{ij}}) - \frac{\partial \overline{q_j}}{\partial x_j} - \frac{\partial \overline{Q_j}}{\partial x_j}. \tag{3.4c}$$

Here, $\overline{R_{ij}}$ and $\overline{Q_j}$ result from decomposing the convective terms appearing on the left-hand side of the second and third equations. The turbulent stress tensor $\overline{R_{ij}}$ is given by $\overline{R_{ij}} = \overline{\rho}\widetilde{u_i'' u_j''}$, while $\overline{Q_j}$ accounts for temperature-velocity turbulent diffusion as well as higher-order velocity correlations:

$$\overline{Q_j} = \overline{\rho} c_p \widetilde{u_j'' T''} + \frac{\overline{\rho}\widetilde{u_i'' u_i'' u_j''}}{2} + \overline{\rho}\widetilde{u_i'' u_i''} u_j''. \tag{3.5}$$

The appearance of the terms $\overline{R_{ij}}$ and $\overline{Q_j}$ prevents the RANS equations from being closed and hence from admitting a closed-form solution.

- LES: Large Eddy Simulation is a more advanced technique than RANS because it is based on the two assumptions of similarity and universality from Kolmogorov's $K41$ theory. The statistics of the largest scales depend on the geometry of the fluid system, whereas the statistics of the smallest scales are universal. Consequently, in LES the large-scale motions of turbulent flow are resolved directly, and only the small-scale, sub-grid scale (SGS) motions are modeled, which leads to a substantial reduction in computational cost. Therefore, the basic concept of LES is to directly resolve the large scales, which depend on the flow, and to use a model to approximate the influence of the small scales on these larger structures. This approach captures the step-by-step temporal evolution of the large scales and thus represents the non-stationary and multiscale nature of turbulent flows.

The Large Eddy Simulation approach involves four main conceptual steps, [9].

1. Define a filtering operator to decompose the velocity into the sum of a filtered and residual (SGS) component. The filtered velocity field represents the motion of the large eddies, while the residual component represents the small modeled scales.

2. Apply the filtering operator to the Navier-Stokes equation to obtain the evolution of the filtered velocity field.

3. Model the subgrid-scale (SGS) tensor σ_{ij}^{SGS} and the subgrid heat flux q_j^{SGS} to achieve closure.

4. Solve numerically the filtered equations, providing an approximation of the large-scale motions in the realization of the turbulent flow.

By applying the Favre filtering to the governing equation, it is possible to obtain the filtered compressible Navier-Stokes equation for a viscous Newtonian fluid:

$$\frac{\partial \overline{\rho}}{\partial t} + \frac{\partial(\overline{\rho}\tilde{u_j})}{\partial x_j} = 0, \tag{3.6a}$$

$$\frac{\partial(\overline{\rho}\tilde{u_i})}{\partial t} + \frac{\partial}{\partial x_j}\left(\overline{\rho}\tilde{u_i}\tilde{u_j}\right) = -\frac{\partial \overline{p}}{\partial x_i} + \frac{\partial \overline{\sigma}_{ij}}{\partial x_j} + \frac{\partial \sigma_{ij}^{SGS}}{\partial x_j}, \tag{3.6b}$$

$$\frac{\partial(\overline{\rho}\,\tilde{E})}{\partial t} + \frac{\partial(\overline{\rho}\tilde{u_j}\tilde{E})}{\partial x_j} = -\frac{\partial(\overline{p}\tilde{u_j})}{\partial x_j} + \frac{\partial}{\partial x_j}(\lambda\frac{\partial \tilde{T}}{\partial x_j} - q_j^{SGS}) + \frac{\partial}{\partial x_j}\left[(\overline{\sigma}_{ij} + \sigma_{ij}^{SGS})\tilde{u_j}\right]. \tag{3.6c}$$

Here, $\overline{\rho}$ is the filtered density, $\tilde{u_i}$ denotes the *ith* component of the Favre-filtered velocity, $\overline{p}$ is the filtered thermodynamic pressure.
$\tilde{E}$ denotes the Favre-filtered total energy per unit mass and it is equal to $c_v\tilde{T}+\widetilde{u_iu_i}/2$. The thermal diffusivity is $\lambda(\tilde{T}) = c_p\mu(\tilde{T})/Pr$, and the molecular viscosity follows Sutherland's law. The viscous stress tensor $\overline{\sigma}_{ij}$ is expressed as:

$$\overline{\sigma}_{ij} = \mu(\tilde{T})\left(\frac{\partial \tilde{u_i}}{\partial \tilde{x_j}} + \frac{\partial \tilde{u_j}}{\partial \tilde{x_i}} - \frac{2}{3}\frac{\partial \tilde{u_k}}{\partial \tilde{x_k}}\delta_{ij}\right), \tag{3.7}$$

while the SGS stress tensor σ_{ij}^{SGS} is modeled following Boussinesq's hypothesis:

$$\sigma_{ij}^{SGS} = \mu_t\left(\frac{\partial \tilde{u_i}}{\partial \tilde{x_j}} + \frac{\partial \tilde{u_j}}{\partial \tilde{x_i}} - \frac{2}{3}\frac{\partial \tilde{u_k}}{\partial \tilde{x_k}}\delta_{ij}\right) - \frac{2}{3}k^{SGS}\sigma_{ij}, \tag{3.8}$$

and the SGS heat flux q_j^{SGS} is modeled from Fourier's law as:

$$q_j^{SGS} = -c_p\frac{\mu_t}{Pr_t}\frac{\partial \tilde{T}}{\partial x_j}. \tag{3.9}$$

Where the proportionality coefficient is the SGS conductivity $\lambda^{SGS} = -c_p\frac{\mu_t}{Pr}$.
μ_t denotes the SGS viscosity, which can be modeled by different turbulent approaches. In this thesis, the Wall-Adaptive Local Eddy-viscosity (WALE) model is adopted to define it, considering the definition by Nicoud and Ducros (1999) [7] as:

$$\mu_t = \mu^{SGS} = \overline{\rho}(C_w\Delta)^2\frac{(S_{ij}^dS_{ij}^d)^{3/2}}{(S_{ij}S_{ij})^{5/2} + (S_{ij}^dS_{ij}^d)^{5/4}}, \tag{3.10}$$

where S_{ij} denotes the resolved strain-rate tensor and S_{ij}^d the traceless symmetric part of the square of the resolved velocity gradient tensor. The constant $C_w = 0.325$ is determined from statistical correlations fitted against DNS reference data, where Δ denotes the local mesh size and Pr_t is the turbulent Prandtl number, set to 0.9.

3.2 Wall-Modeled LES

In bounded flows, a difficulty arises because peak turbulence generation takes place in the inner region of the boundary layer, where energy is transferred from the smaller to the larger turbulent scales, [17]. When the computational mesh is too coarse to accurately capture these inner-layer dynamics, as is often the case in high-Reynolds-number LES to keep computational costs manageable, the turbulence represented in the outer layer can no longer be considered physically valid. This challenge is referred to as the near-wall problem in LES. The Wall-Modeled Large-Eddy Simulation (WMLES) strategy tackles this by modeling the energetic eddies in the near-wall inner region, and a traditional way to obtain a closed-form solution is through the use of wall-stress models. Nearly all wall-stress models rely on the physical principle of momentum conservation in an approximately parallel shear flow.

3.2.1 Equilibrium wall model

The whole point of this work is to use an equilibrium wall-model (EWM) to avoid resolving any turbulence in the inner layer. Starting from the RANS momentum and energy equations, 3.4b and 3.4c, it is possible to derive the system of ODEs for the equilibrium wall model for calorically-perfect gasses as formulated by Kawai & Larsson [20]. The model acts on a refined inner grid that is embedded in the coarser outer LES grid. In the inner grid, the equilibrium-boundary-layer equations are solved as:

$$\frac{d}{dy}\left(\mu_{wm}^{tot}\frac{dU_{wm}}{dy}\right) = 0, \tag{3.11}$$

$$\frac{d}{dy}\left(\lambda_{wm}^{tot}\frac{dT}{dy}\right) = -\frac{d}{dy}\left(\mu_{wm}^{tot}U_{wm}\frac{dU_{wm}}{dy}\right) \tag{3.12}$$

where

$$\mu_{wm}^{tot} = \mu_{wm} + \mu_{t,wm}, \tag{3.13}$$

$$\lambda_{wm}^{tot} = \frac{c_p\mu_{wm}}{Pr} + \frac{c_p\mu_{t,wm}}{Pr_{t,wm}} \tag{3.14}$$

represent the total model viscosity and thermal diffusivity.
The wall-model eddy viscosity is defined as:

$$\mu_{t,wm} = k\rho_{wm}yu_\tau D \tag{3.15}$$

where

$$u_\tau = \sqrt{\frac{\tau_{w,wm}}{\rho_{wm}}} \tag{3.16}$$

and $k = 0.41$ is the Von Karman constant, $\rho_{wm} = p^{LES}/(RT_{wm})$ is the wall model density distribution, and p^{LES} is the external LES pressure. In order to correct the near-wall behavior, Eq. 3.15 has to be complemented with a damping function, D, which under the classical Van Driest formulation is $D = [1 - exp(-y^+/A^+)]^2$, with $A^+ = 17$ indicating the dimensionless height above the wall where the molecular and turbulent viscosities become of the same order of magnitude. y^+ is the wall-normal coordinate normalized to viscous units, $Pr_{t,wm} = 0.9$ is the turbulent Prandtl number, and $\mu_{wm} = \mu_{wm}(T_{wm})$ is the laminar wall model viscosity, which satisfies

Sutherland's law, B.22. Under the equilibrium assumption, the bracketed quantities in Eqs. E.1 and E.2 are constant across the wall-modeled layer. These conserved quantities correspond to the sum of the viscous and turbulent shear stress (in Eq. E.1) and to the sum of molecular heat conduction, turbulent heat transport (left hand side of Eq. E.2) and aerodynamic heating (right hand side of Eq. E.2). Fig. 40 illustrates how this system of ODEs is solved on a dedicated grid that is embedded within the main LES mesh. The equations are computed over an independent grid that goes from $y = 0$ to $y = h_{wm}$ where an exchange of information between both grids occurs. The inner wall-model simulation takes the LES flow variables at the location as its free-stream boundary condition:

$$U_{wm} = u^{LES}, \quad T_{wm} = T^{LES}, \quad P_{wm} = p^{LES} \tag{3.17}$$

These quantities are used to define the wall shear stress τ_w and the heat flux q_w, which are then fed back to the LES solver as boundary conditions. The accuracy of the computation of τ_w and q_w is increased by stretching the grid near the wall. WMLES models are specifically designed so that the first grid point is located as far from the wall as feasible. This feature is both the main advantage and the main drawback of the WM strategy: the no-slip condition for velocity, as well as isothermal or adiabatic temperature boundary conditions, are no longer enforced directly. Instead, the influence of the wall is represented indirectly through modeled wall shear stress and heat flux.

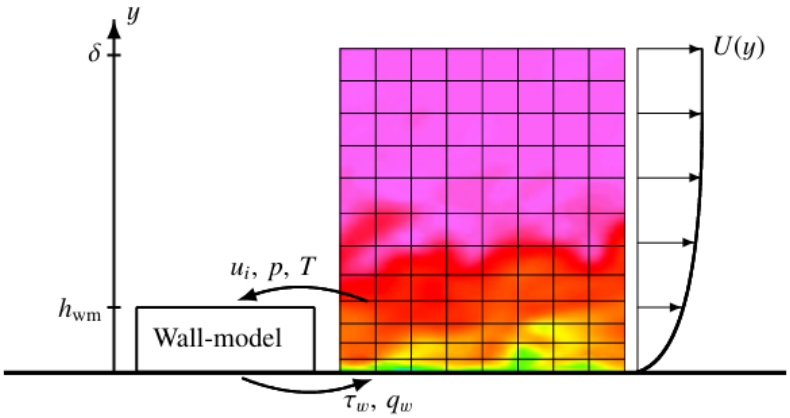

Figure 15: Instantaneous snapshot of a boundary layer with overlaid LES grid. The wall-model models the flow in a layer of thickness h_{wm}: it is fed instantaneous velocity and temperature information from the LES, and returns the instantaneous wall stress and heat flux to the LES, which then uses these as the wall boundary condition., Kawai & Larsson [20].

3.3 STREAmS

The analysis was performed with STREAmS (Bernardi et al,. (2021) [26]), an open-source numerical solver for compressible flows oriented to modern High-Performance-Computing (HPC) platforms using Message-Passing-Interface (MPI) parallelization and supporting multi-GPU architectures (CUDA paradigm), that solves the Navier-Stokes equations, B.19.The cluster used to evaluate the problem is Leonardo (CINECA), a new pre-exascale cluster with Ampere NVIDIA GPUs.
To accurately handle discontinuities, STREAmS employs a hybrid discretization approach for the convective terms of the Navier-Stokes equations. In smooth regions, the solver utilizes sixth-order energy-preserving schemes, a numerical strategy that guaranties the discrete system maintains the conserved quantities (energy, momentum, mass) of the continuous equations. In the vicinity of shocks, it switches to a Weighted Essentially Non-Oscillatory (WENO) scheme. The WENO method assigns larger weights to stencils that promote a smooth transition across discontinuities, thereby preventing the emergence of spurious oscillations. The switch between the energy-preserving scheme and the WENO shock-capturing scheme is governed by the Ducros shock sensor, Ducros et al. (1999) [8]. The methodology is based on solving the compressible Navier–Stokes equations, assuming that the molecular viscosity μ follows Sutherland's law with a reference free-stream temperature of $T_\infty = 220$ K. The Prandtl number is taken as $Pr = 0.72$, and the thermal conductivity is defined as $k = \frac{\mu c_p}{Pr}$, where c_p denotes the specific heat at constant pressure. A cartesian grid is used in order to solve the system of equations which is completed by the equation of state for a calorically perfect gas.

3.3.1 Immersed Boundary Method

In STREAmS, a technique known as the Immersed Boundary Method (IBM) [11] is used to enforce the no-slip, no-penetration, and isothermal or adiabatic boundary conditions on the surface. The main advantage of this method is that it is formulated on a Cartesian grid, which does not have to conform to the geometry. This approach enables the simulation of viscous flow with immersed boundaries on grids that do not need to follow the exact geometry of the object. Consequently, grid generation becomes much easier, since creating body-fitted structured or unstructured grids is extremely laborious.
The principle of this approach is to first define a surface grid along the boundaries and then use it as a boundary condition to construct a grid within the fluid region. As a result, the solid boundary intersects this Cartesian volume grid. Since the grid does not conform to the solid surface, enforcing the boundary conditions requires modifying the governing equations in the neighborhood of the boundary. Therefore, it is essential to use a method capable of handling both Dirichlet and Neumann boundary conditions. In STREAmS a ghost node method is implemented.
The boundary condition on the IB is imposed by means of ghost cells, defined as cells located inside the solid that have at least one neighboring cell in the fluid. For each of these cells, an interpolation scheme is constructed that embeds the boundary condition at the IB. A simple option is bilinear (trilinear in 3D) interpolation, where a generic flow variable ϕ can be expressed as follows:

$$\phi(x, y) = C_1 xy + C_2 x + C_3 y + C_4 \tag{3.18}$$

where C_i are the interpolation coefficients. An IBM configuration is defined by the following elements:

- x_g denotes a ghost node,
- x_i represents the associated image point,
- x_b identifies the position of the boundary surface.

In the IBM method, the flow variable ϕ is interpolated at the location x_{int} in order to impose the boundary conditions and accurately evaluate τ_w and q_w. Given the distance $d = \|x_b - x_g\|$, the image point is placed according to:

$$x_{int} = x_g + 2nd \tag{3.19}$$

where n is the local normal direction to the boundary passing through the ghost node x_g.
A no-slip wall condition is applied by interpolating a generic flow variable ϕ in the proximity of x_{ip} and then setting its value at the corresponding ghost point. If ϕ is governed by a Dirichlet-type boundary condition, with ϕ_b the prescribed value of ϕ at x_b, the ghost value ϕ_g is given by:

$$\phi_g = 2\phi_b - \phi_{int} \tag{3.20}$$

For a Neumann-type boundary condition, instead, one simply sets:

$$\phi_g = \phi_{int} \tag{3.21}$$

For an adiabatic no-slip wall, condition 3.20 is enforced on all velocity components. Condition 3.21 is instead used to specify a zero-gradient condition for both temperature and pressure. In the case of isothermal no-slip walls, the wall temperature is imposed according to Eq. 3.20, while the velocity and pressure fields are treated in the same way as in the adiabatic configuration:

$$u_g = -u_{int}, \quad v_g = -v_{int}, \quad w_g = -w_{int}, \tag{3.22}$$

$$T_g = 2T_b - T_{int}, \qquad p_g = p_{int} \tag{3.23}$$

The use of a second-order numerical scheme for near-wall quantities makes this method effective, provided that the boundary surface is adequately resolved.
The near-wall treatment makes it possible to prescribe the correct shear stress and heat flux values without requiring very fine grid resolution in the near-wall region. The point x_{int} serves as the initial position of the interface between the outer LES solver and the near-wall zone where the ODEs are solved.

$$\tau_w^{wm} = \mu_w \left(\frac{U_i^{int} - U_i^g}{\Delta y_i} \right) \tag{3.24}$$

$$q_w^{wm} = \lambda_w \left(\frac{T_i^{int} - T_i^g}{\Delta y_i} \right) \tag{3.25}$$

The wall-modeled wall-shear stress and heat flux are enforced as Dirichlet boundary conditions by modifying the overall viscosity and diffusivity fields, by prescribing an effective viscosity and diffusivity at the bound location:

$$\mu_g^{tot} = 2\mu_{eff} - \mu_{int}^{tot} \tag{3.26}$$

$$\lambda_g^{tot} = 2\lambda_{eff} - \lambda_{int}^{tot} \tag{3.27}$$

where

$$\mu_{eff} = \frac{\tau_w^{WM}}{\tau_w^{WR}}\mu_w \tag{3.28}$$

$$\lambda_{eff} = \frac{q_w^{WM}}{q_w^{WR}}\lambda_w \tag{3.29}$$

Eq. 3.28 and 3.29 respectively denote the laminar wall viscosity, corrected by the ratio between modeled and resolved shear stress, and the laminar wall diffusivity, corrected by the ratio between modeled and resolved heat fluxes. These quantities represent the missing SGS (SubGrid Scale) contribution at the wall, which supplies the appropriate wall shear stress and heat flux to the outer LES field according to, [24]:

$$\tau_w^{LES} = \mu_{eff}\frac{U_i^{int} - U_i^g}{\Delta y_i} = (\mu_w + \mu_w^{SGS})\frac{U_i^{int} - U_i^g}{\Delta y_i} \tag{3.30}$$

$$q_w^{LES} = \lambda_{eff}\frac{T_i^{int} - T_i^g}{\Delta y_i} = (\lambda_w + \lambda_w^{SGS})\frac{T_i^{int} - T_i^g}{\Delta y_i} \tag{3.31}$$

Thus, in this approach, effective quantities are defined so that the viscous shear stress and heat flux obtained from LES discretization coincide with the values predicted by the wall model.
Therefore, in the case of WMLES, the SGS viscosity and diffusivity at the wall location are not null. These quantities can be fed back to the LES outer field, correcting the velocity and temperature gradients by a factor that provides the desired shear stress and heat flux at the wall location. It is worth pointing out that when grid resolution progressively increases from the purely WM to the WR case, it is likely that the matching location of the wall model falls inside the buffer layer. A region not suitable to act as an exchange location with the LES field since it is characterized by extreme velocity and pressure fluctuations. To avoid this occurrence, the WM-matching locations are identified by the condition of being at least the third off the wall point and having $y^+ > 40$.

3.3.2 Simulation Setup

Supersonic turbulent boundary layers at a free-stream Mach number of $M_\infty = 2.9$ over a compression ramp characterized by an angle of $\theta = 24^\circ$ are simulated with a wall-modeled LES (WMLES) in order to avoid the expensive computational cost associated with performing the same simulation using direct numerical simulation (DNS). The computational domain, with dimensions $140\delta_{in} \times 40\delta_{in} \times 9\delta_{in}$, is discretized in the STREAmS solver using a Cartesian, non-body-conformal structured grid. Stretched grid configurations are employed, with a uniform spatial step in the z direction of the domain, to more accurately capture the flow behavior and the influence of pressure gradients near the ramp, and to assess their differences and consistency with the reference experiment of Dawson et al., (2013) [19].
Therefore, the node density decreases as one moves away from the wall and farther from the ramp corner region.
The simulation domain is divided into three regions, Fig 16:

1. An initial smooth-wall section dedicated to the development of a turbulent boundary layer.

2. At the streamwise position $x = 80\delta_{in}$ (δ_{in} is the boundary layer thickness at the inflow), a flow recirculation region forms, and an oblique shock wave is generated due to the presence of a ramp with an inclination angle of $\theta = 24°$,

3. A downstream smooth-wall recovery region exists before the outflow at the end of the compression ramp, where the flow experiences an expansion.

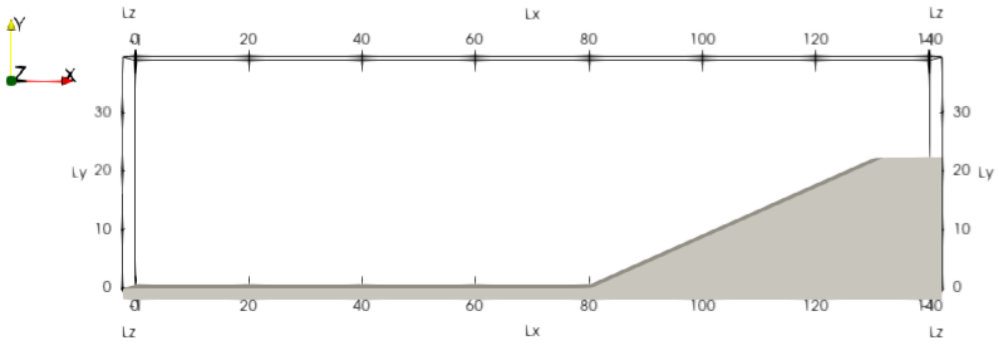

Figure 16: Schematic of the computational domain: $L_x = 140\,\delta_{in}$, $L_y = 40\,\delta_{in}$, and $L_z = 9\,\delta_{in}$. The free-stream flow with $M_\infty = 2.9$ enters the domain from the right-hand side and exits on the left-hand side.

Different simulation cases are carried out using various mesh configurations, ranging from a coarse grid to a finer one, in order to assess the differences and analyze how the equilibrium wall model behaves under these conditions. Table 2 summarizes the setup of each grid, labeled with the letter G followed by the corresponding number of grid points. Figure 19 illustrates the variation of the spatial steps in the x and y directions, namely Δx and Δy, respectively. In the x direction, a constant grid spacing is adopted upstream of the ramp at $x/\delta = 80$ and downstream of it, while a refined spacing is used in the vicinity of the ramp corner to accurately capture the separation region and the recirculation zone associated with shock-wave formation. A similar strategy is applied in the y direction, where the mesh is refined near the wall.

Grid	Run	N_{tot}
600-250-80	G1	12M
800-300-80	G2	19.2M
656-270-80	G3	14.17M
904-350-90	G4	28.47M

Table 2: Mesh grid simulation setup. N_{tot} indicates the number of points used for each grid configuration.

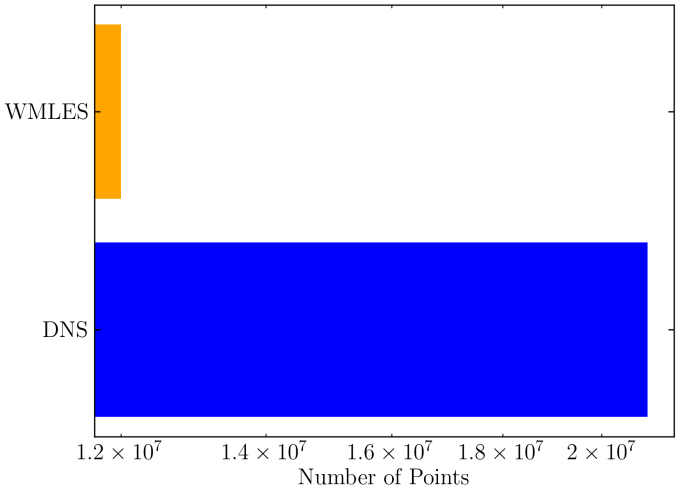

Figure 17: Comparison of the total number of grid points N_{tot} between the coarse case of WMLES and DNS by Wu & Martin (2008) [13].

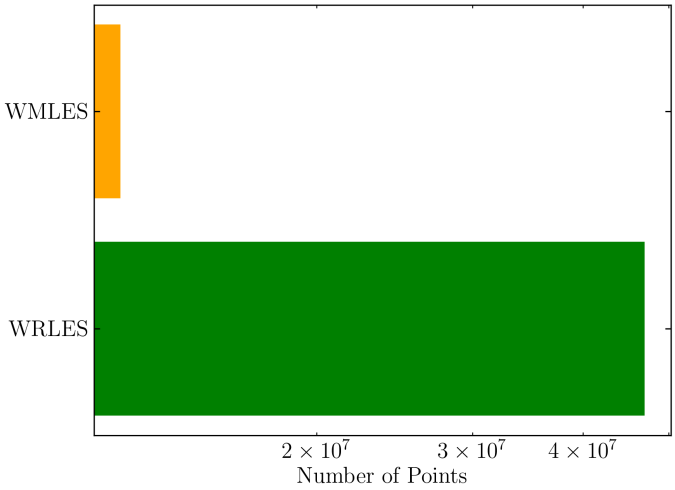

Figure 18: Comparison of the total number of grid points N_{tot} between the coarse case of WMLES and WRLES by Dawson et al., (2013) [19].

For this thesis, the aim was to impose the same simulation setup defined by Dawson et al. (2013) [19], considering different grid configurations ranging from the coarse to the fine one. In Fig.18, a comparison of the computational requirements of the simulations is shown in order to confront the total number of points between the coarser grid *G1* characterized by $N_{tot} = 12M$ and the DNS by Wu & Martin (2008) [13] used as reference data for this work, with a total number of grid points equal to $N_{tot} = 21M$. The same is done between the total number of grid points of the finer WRLES configuration, $N_{tot} = 47M$, implemented by Dawson et al. (2013) [19], and again the WMLES one. Therefore, assuming that the computational cost scales with the number of grid cells, the DNS is about 2 times more expensive, and the WRLES is 4 times more expensive than the WMLES simulation.
Moreover, other input parameters are involved to lead to a correct simulation and to define different output values that allow for better validation of the conclusions for this work:

- h_{wm}: The choice of the matching location h_{wm} where the WMLES approach is applied. This parameter specifies the distance of the wall-model interface point in terms of the local cell size.

- Re_τ: The friction Reynolds number, Eq. 2.37. This quantity is used to initialize the simulation. The actual value of $\mu_\tau = \sqrt{\tau_w/\rho}$ is only known at the end of the computation, as it depends on the chosen mesh, the wall-modeling itself, the boundary conditions, and thus on μ_{eff}.

- μ_{eff}: The clipping factors are described as constraints in subsection 3.3.1 for the definitions of τ_w and q_w. The need to impose clipping on the effective viscosity, μ_{eff}, is intended to prevent numerical instabilities that may lead to a simulation blow-up in the case of a strong adverse pressure gradient.

- *Ducros-sensor*: It is used to distinguish the regions with high values of dilatation (shocks) from the region of high vorticity. The Ducros sensor attains a value close to 1 in the regions of high dilatation while reducing it down to 0 in the regions of high vorticity with no dilatation. This is necessary because accurately resolving turbulence requires low numerical dissipation, and this lack of dissipation can cause oscillations and eventual blow-up of the simulation in the presence of discontinuities. This sensor is an extension of Jameson's scheme, achieved by multiplying the pressure fluctuation-based sensor by a function of the local dilatation and vorticity

$$\Phi = \frac{(\nabla \cdot u)^2}{(\nabla \cdot u)^2 + |\nabla \times u|^2 + \epsilon} \tag{3.32}$$

  where u is the velocity vector, $\nabla \cdot u$ is the velocity divergence, $|\nabla \times u|$ is the vorticity module, and ϵ is a small number to avoid division by zero [8].
  For all simulations, a value of 0.005 was selected. This choice corresponds to a dissipative scheme that is activated only when anomalous peaks are detected.

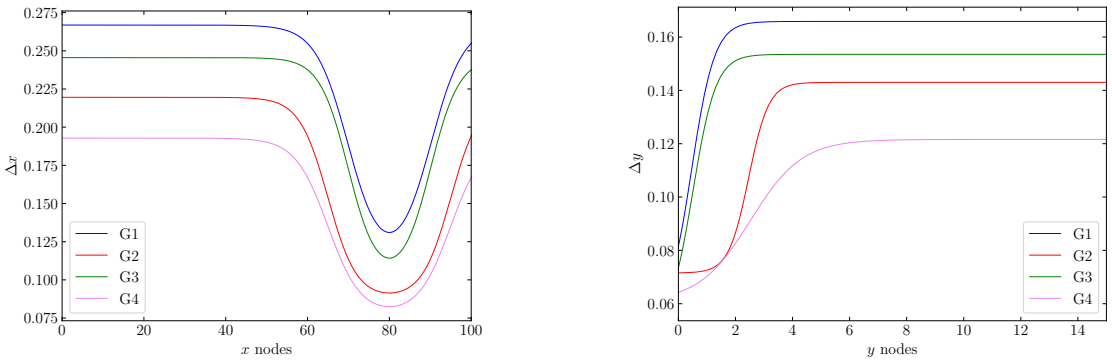

(a) Stretching along x direction

(b) Stretching along y direction

Figure 19: Stretching mesh configuration for all the cases considered. In the x direction, the stretching is applied both before and after the start of the ramp at $x = 80\delta$. In the y direction, the mesh is finer near the wall for the first nodes, and then gradually returns to a uniform configuration.

4 Results

An overview of the mean flow results is provided, focusing on the average values of pressure, density, and temperature. This allows for a graphical confirmation of the aspects highlighted by the gas-dynamic behavior of the flow in this specific case study. In addition, a statistical analysis of the results is carried out to validate the mean flow findings and to confirm the model, emphasizing the advantages and limitations encountered during the work.

4.1 Mean flow visualization

The different grid setups used in this work do not produce any appreciable net difference in the mean flow visualization, therefore, it was decided to present only one representative graph for each data set, *G1*. Figure 20 shows the averaged fields of pressure, density, and temperature, respectively.
Focusing on the pressure field, the strong influence that shock-wave formation exerts on the flow properties can be observed, along with how these are modified as a consequence. At the beginning of the compression ramp, the corresponding station shows a shock wave that is not yet fully developed, as the jump in the flow quantities is not clearly defined. This confirms that the flow already senses the presence of the compression ramp and that, at an upstream location, the shock begins to form, becoming fully established above the separation region. This is further supported by the fact that the average pressure values near $x/\delta = 80$ transition smoothly from 1 to 4. Considering the white shock-wave line, one can clearly see an abrupt change from 1 to values exceeding 4. These observations are similarly evident in the density and temperature plots because of the correlation through the ideal gas law.
An adverse pressure gradient causes heating of the boundary layer at the ramp corner, which is confirmed by assuming constant pressure in the wall-normal direction and thus obtaining the relation $\rho \propto 1/T$. This indicates that a hot wall leads to a small density at and above the wall. For each visualization, it is also possible to observe the opposite event with respect to the compression ramp: an expansion. This is a reverse phenomenon, as all quantities decrease, highlighting the quality of the results obtained.
Figure 20c illustrates the development of the thermal boundary layer from the wall temperature toward the freestream value. The color pattern confirms the evolution presented in 2.3, showing a peak value close to the wall. Near the ramp corner, where the flow experiences a more chaotic behavior, the intensified color pattern highlights the strong entropic phenomenon associated with the shock wave.
The evolution of the mean streamwise velocity, Fig. 21, for case *G1ML3* is analyzed in *PARAVIEW* to qualitatively assess how it changes at different y/δ locations. This is carried out by placing a slice along both the smooth and the oblique sections of the y-domain direction. The expansion region is not considered, as it is outside the scope of this study. The progression of the mean streamwise velocity and the recovery to 99% of the freestream velocity are evidenced by the color scale confirming the evolution of the velocity field from the no-slip boundary condition imposed at the wall, 3.3.1. In the compression ramp region, the flow first slows down, but then its velocity increases again along the ramp, confirming the dynamic properties of the shock wave associated with the compression ramp. The separation zone causes the

turbulent flow to behave more chaotically due to the presence of an adverse pressure gradient, which is responsible for the deceleration of the flow.

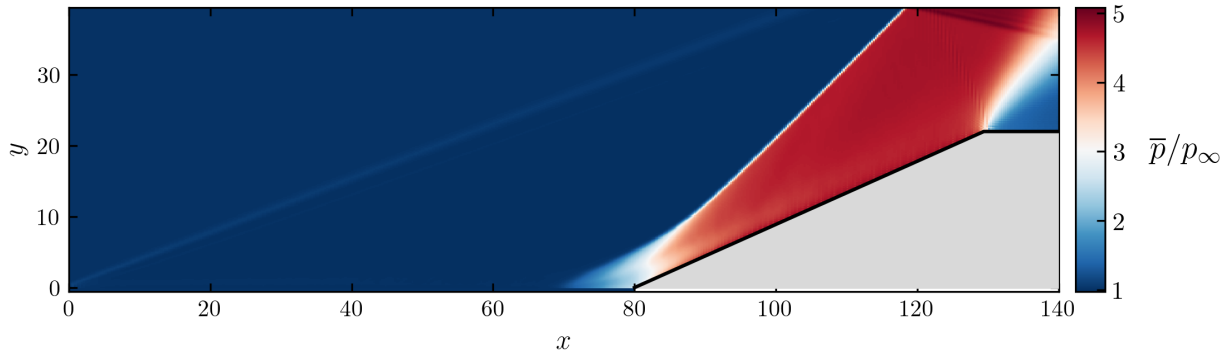

(a) Mean pressure distribution in a $x - y$ slice.

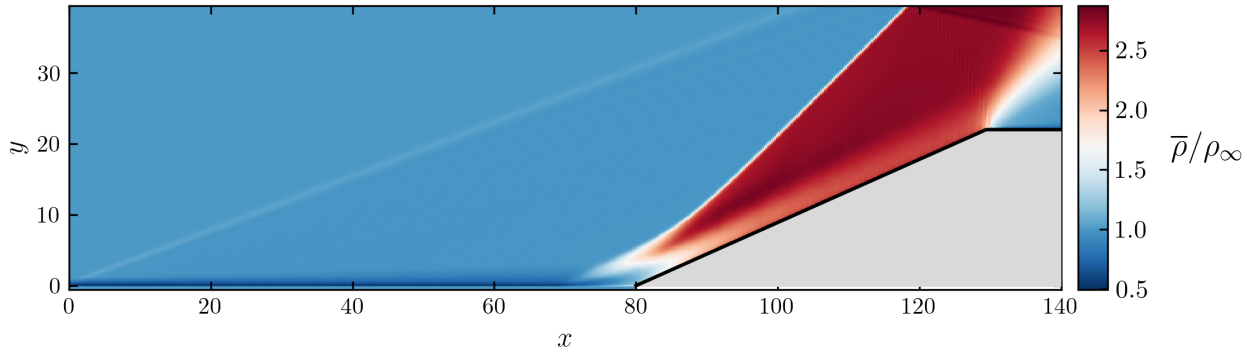

(b) Mean density field in a $x - y$ slice.

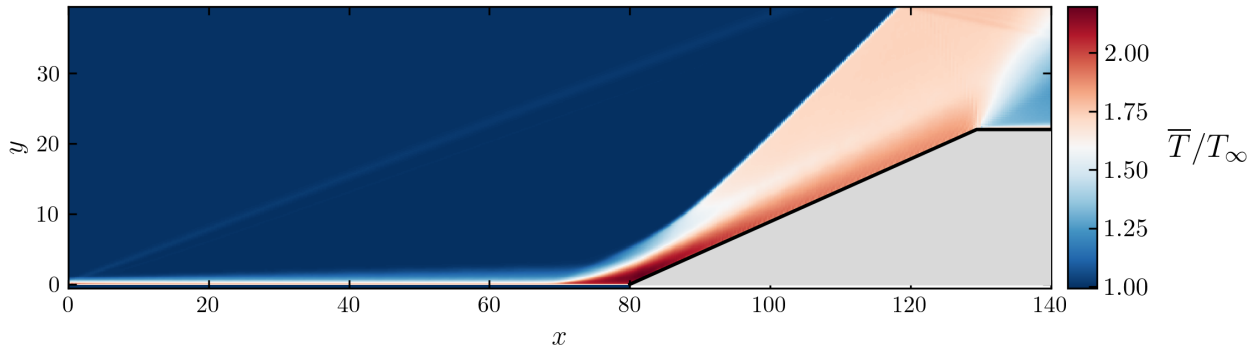

(c) Mean temperature field in a $x - y$ slice.

Figure 20: Mean flow fields across the simulation domain. The start of the compression ramp corner is located at $x = 80\delta$. The grey solid figure indicates the ramp. An expansion region can be observed at the end of the ramp.

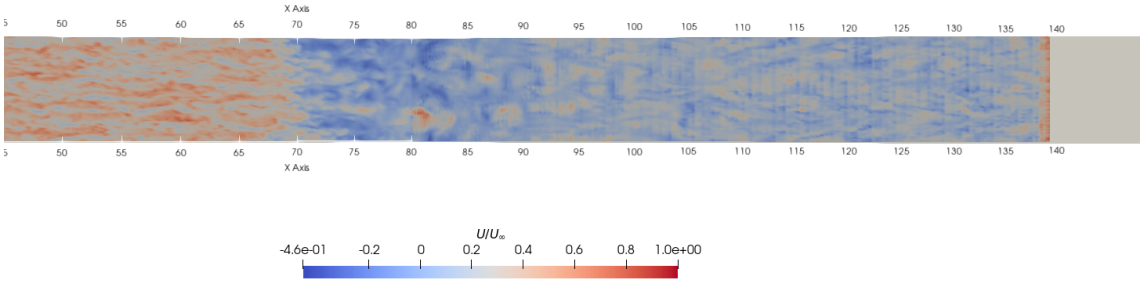

(a) Mean streamwise velocity evolution for the case *G1ML3* along the $x - z$ plane from $x/\delta = 45$ to $x/\delta = 130$, with the slice taken at $y/\delta = 0.1$.

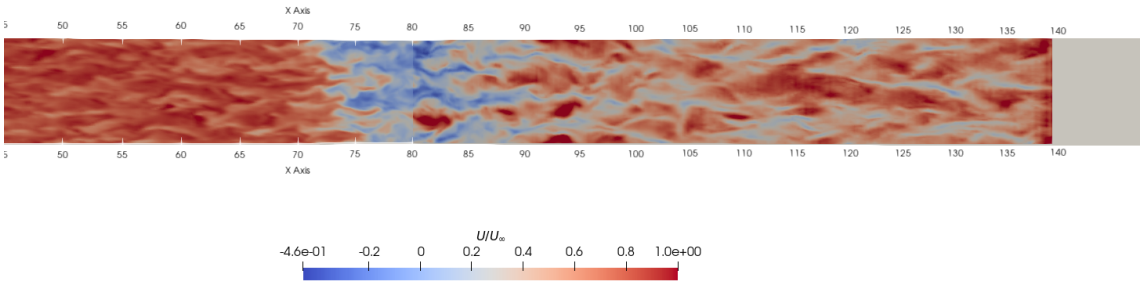

(b) Mean streamwise velocity evolution for the case *G1ML3* along the $x - z$ plane from $x/\delta = 45$ to $x/\delta = 130$, with the slice taken at $y/\delta = 0.5$.

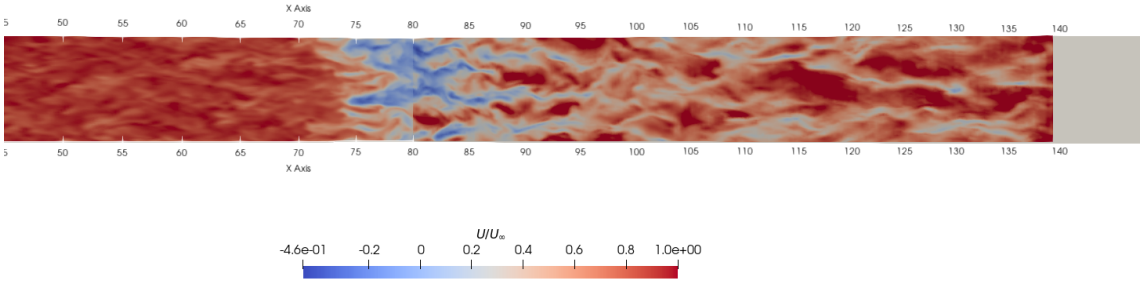

(c) Mean streamwise velocity evolution for the case *G1ML3* along the $x - z$ plane from $x/\delta = 45$ to $x/\delta = 130$, with the slice taken at $y/\delta = 0.8$.

Figure 21: *G1ML3* mean streamwise velocity evolution at different y/δ along the domain from $x/\delta = 45$ to $x/\delta = 130$. The expansion region beyond $x/\delta = 130$ is not considered.

For a deeper understanding of the evolution of turbulent boundary layers in the interaction region, the instantaneous coherent vortex structure is studied through the second invariant of the velocity gradient tensor Q:

$$Q = \frac{1}{2}(\overline{\Omega}_{ij}\overline{\Omega}_{ij} - \overline{S}_{ij}\overline{S}_{ij}) \tag{4.1}$$

where

$$\overline{\Omega}_{ij} = \frac{1}{2}\left(\frac{\partial \overline{u}_i}{\partial x_j} - \frac{\partial \overline{u}_j}{\partial x_i}\right), \qquad \overline{S}_{ij} = \frac{1}{2}\left(\frac{\partial \overline{u}_i}{\partial x_j} + \frac{\partial \overline{u}_j}{\partial x_i}\right) \tag{4.2}$$

The variables denote the symmetric and asymmetric parts of the velocity gradient tensor; respectively, the presence of a vortex is determined by whether the local rate of rotation is larger than the rate of strain or not.

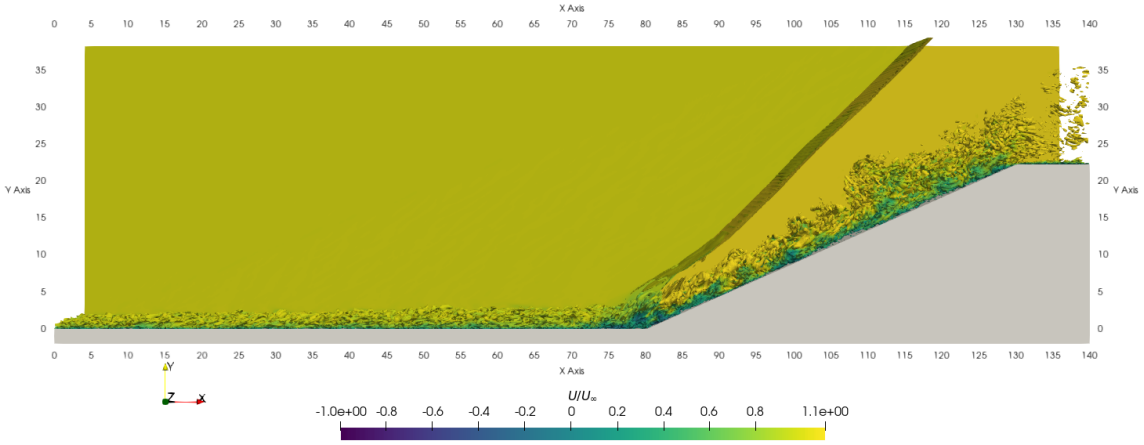

Figure 22: Mean streamwise velocity evolution in $x-y$ plane along the domain with Q-criterion visualization.

Figure 22 shows a quality visualization of the evolution of the mean streamwise velocity obtained using the Q-criterion, highlighting the vortex structures along the domain. This representation is consistent with what Figure 21 illustrates at different values of y/δ: the no-slip condition at the wall and the evolution of the boundary layer along the x-direction of the domain.
A complete view of the mean streamwise velocity recovery of the freestream condition is indicated by the black contour level, Fig. 23, where the $0.99U_\infty$ is indicated.

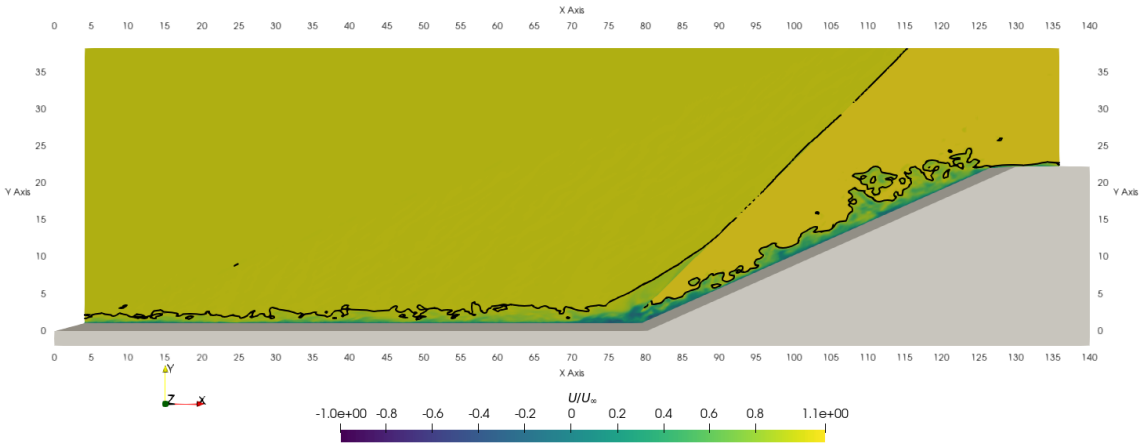

Figure 23: Mean streamwise velocity evolution in $x-y$ plane along the domain with Q-criterion visualization. The black line represents the boundary layer thickness δ_{99}.

Figures 24, 26 and 28 illustrate the local rotational motion of the flow, the vorticity, at different y/δ. For the smooth part of the domain, a decrease in vorticity intensity for each component is confirmed. Moreover, the occurrence of shock-turbulent boundary-layer interaction (STBLI) is emphasized by the peak in the color pattern within the separation region. It is evident that the boundary layer undergoes compression near the corner, which increases the velocity gradient $\partial u/\partial y$ and, thus, the vorticity. This interpretation is reinforced by the color distribution in the proximity of the ramp corner, where areas of high vorticity are more distinctly delineated. A full visualization of the vorticity is provided in Fig. 25, 27 and 29.

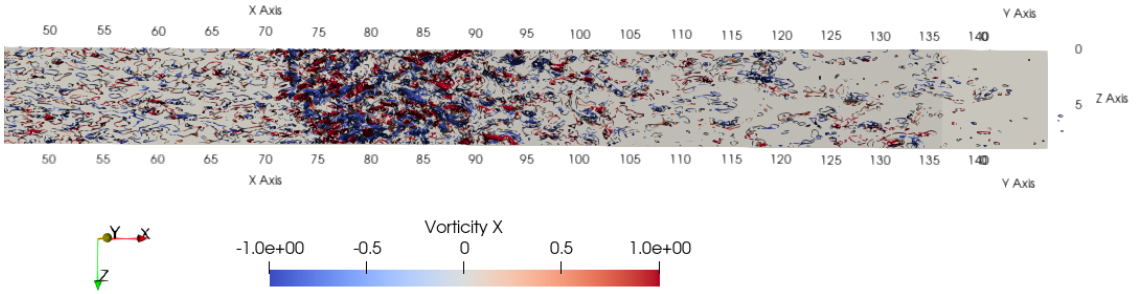

(a) Vorticity component in the x-direction for the case *G1ML3*, from $x/\delta = 45$ to $x/\delta = 130$, with the slice taken at $y/\delta = 0.5$.

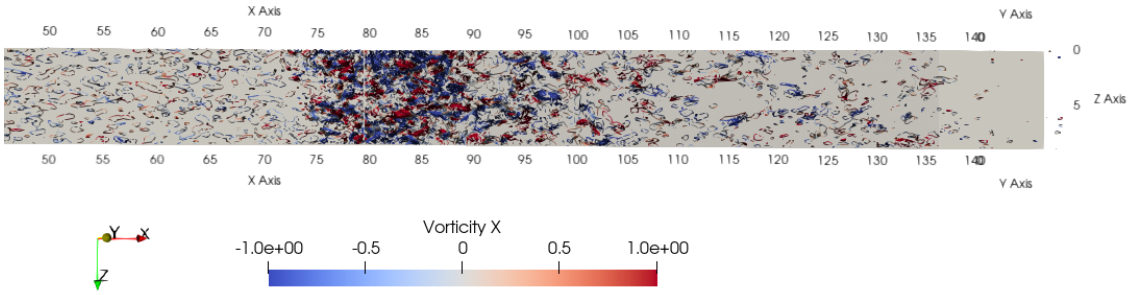

(b) Vorticity component in the x-direction for the case *G1ML3*, from $x/\delta = 45$ to $x/\delta = 130$, with the slice taken at $y/\delta = 1$.

Figure 24: *G1ML3* vorticity component in the x-direction for various values of y/δ. Blue denotes negative vorticity corresponding to clockwise rotation, while red denotes positive vorticity associated with counterclockwise vortex motion.

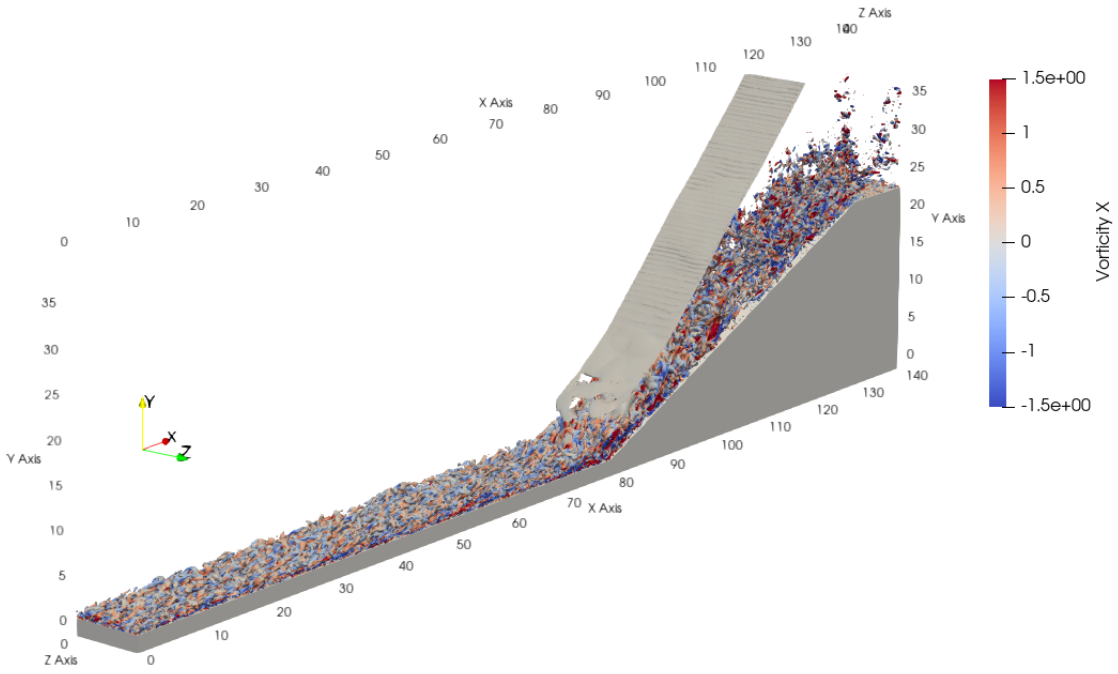

Figure 25: Vorticity along the x-direction of the domain.

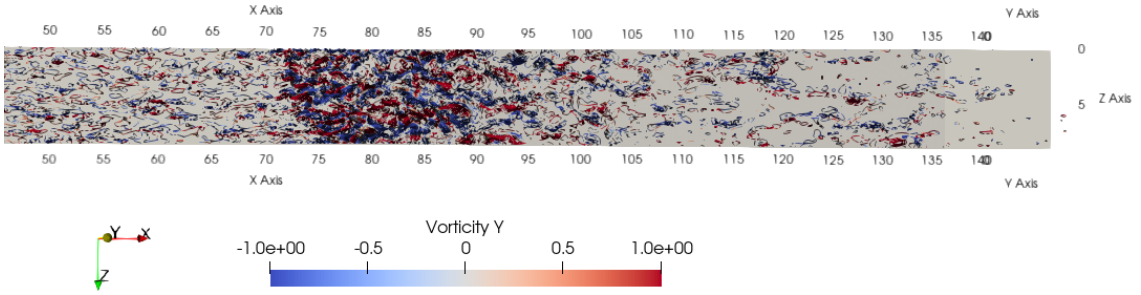

(a) Vorticity component in the y-direction for the case *G1ML3*, from $x/\delta = 45$ to $x/\delta = 130$, with the slice taken at $y/\delta = 0.5$.

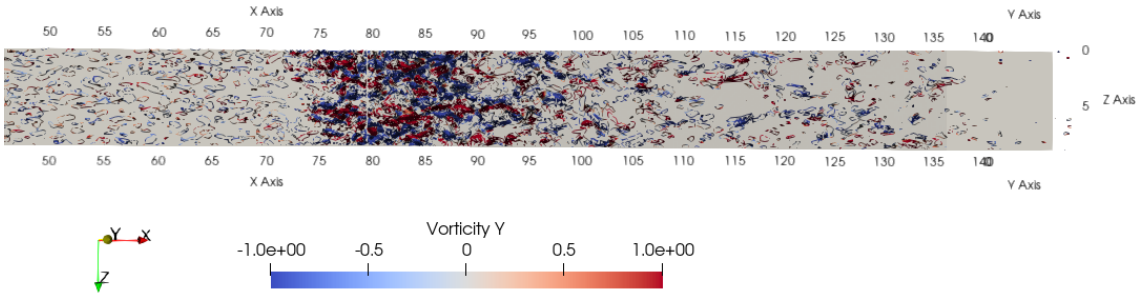

(b) Vorticity component in the y-direction for the case *G1ML3*, from $x/\delta = 45$ to $x/\delta = 130$, with the slice taken at $y/\delta = 1$.

Figure 26: *G1ML3* vorticity component in the y-direction for various values of y/δ. Blue denotes negative vorticity corresponding to clockwise rotation, while red denotes positive vorticity associated with counterclockwise vortex motion.

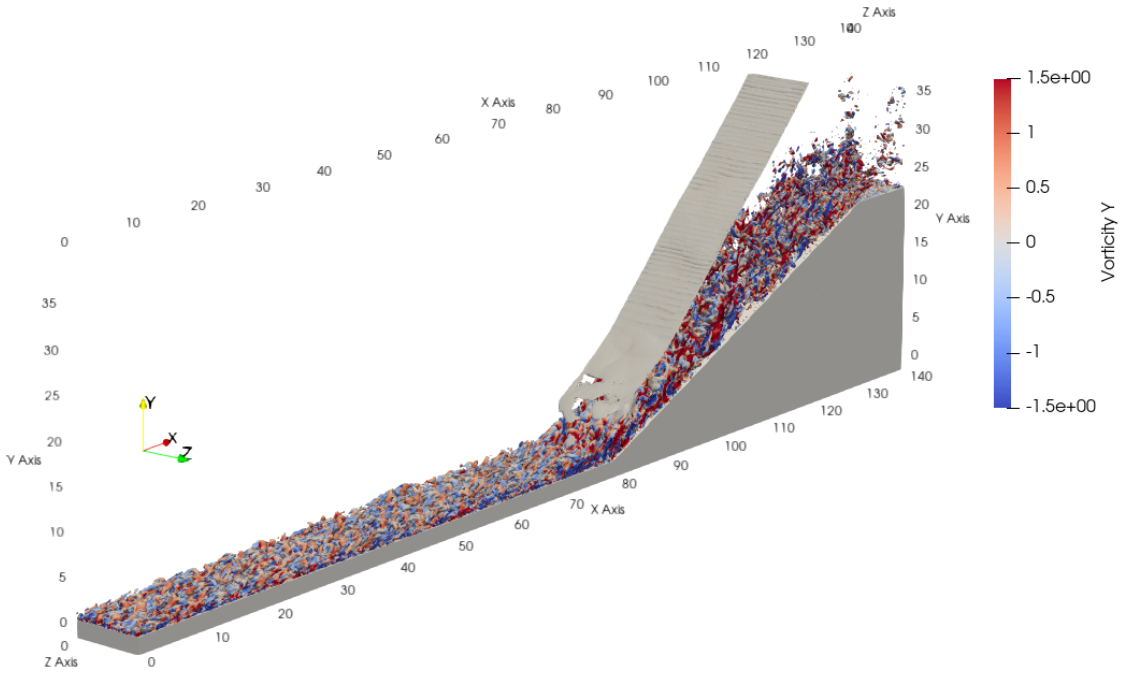

Figure 27: Vorticity along the y-direction of the domain.

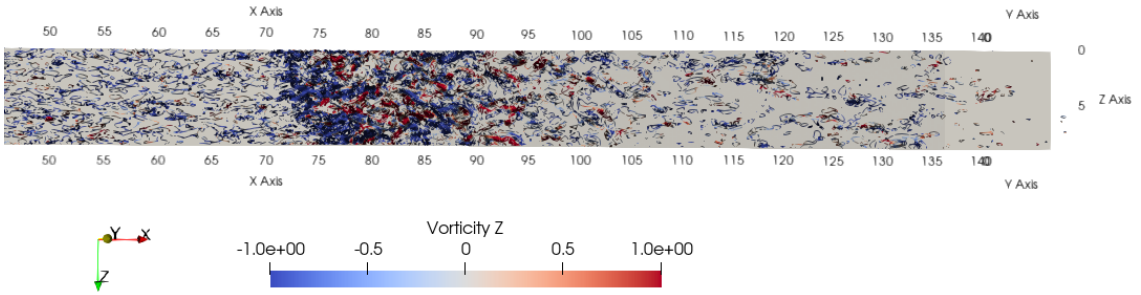

(a) Vorticity component in the z-direction for the case *G1ML3*, from $x/\delta = 45$ to $x/\delta = 130$, with the slice taken at $y/\delta = 0.5$.

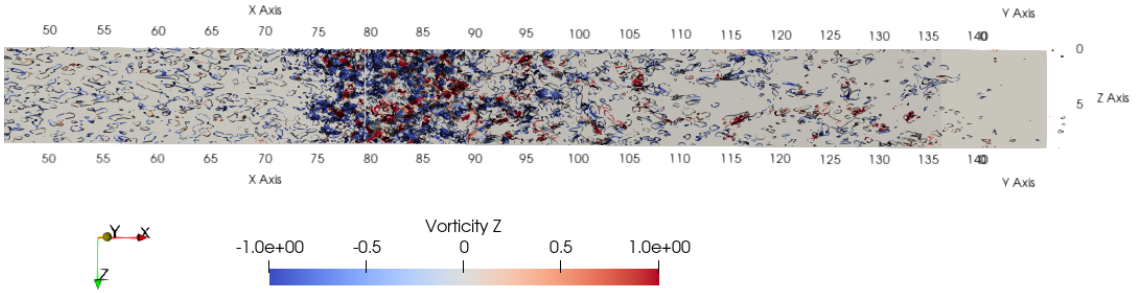

(b) Vorticity component in the z-direction for the case *G1ML3*, from $x/\delta = 45$ to $x/\delta = 130$, with the slice taken at $y/\delta = 1$.

Figure 28: *G1ML3* vorticity component in the z-direction for various values of y/δ. Blue denotes negative vorticity corresponding to clockwise rotation, while red denotes positive vorticity associated with counterclockwise vortex motion.

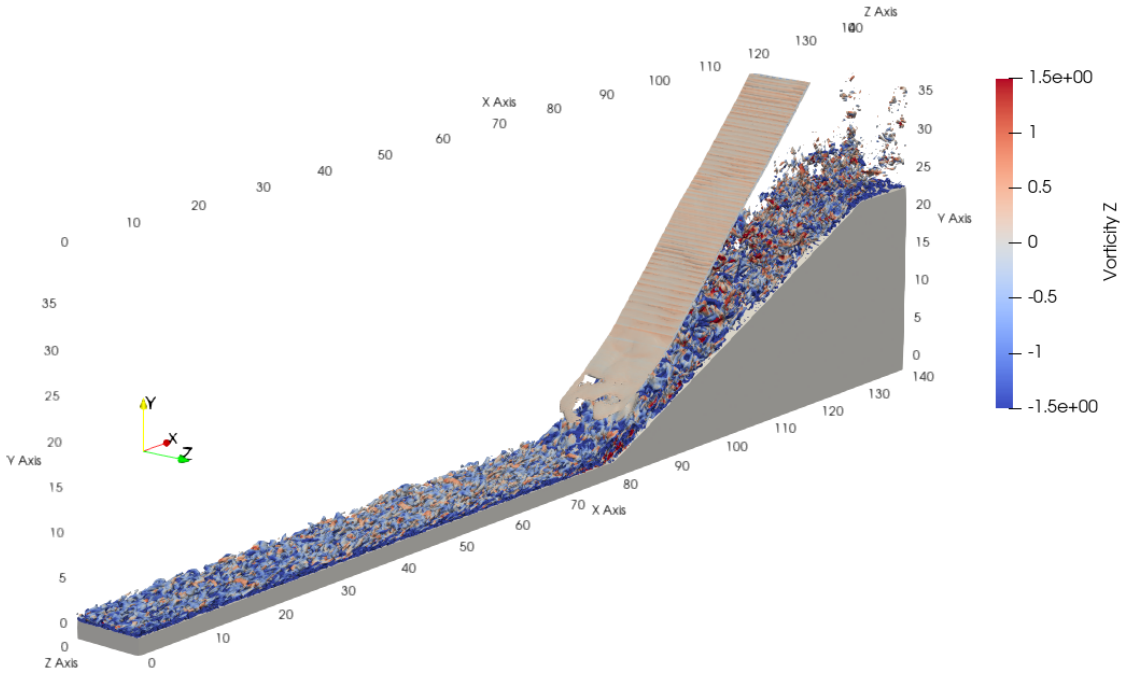

Figure 29: Vorticity along the z-direction of the domain.

From the definition of the vorticity vector field $w(x, y, z)$ as the curl of the velocity vector

$$w = \nabla \times v, \tag{4.3}$$

it appears in the decomposition of the velocity field as the rotation term in the fundamental theorem of kinematics, which states that the velocity of a fluid element $v + dv$ in a continuum is composed of the rates of translation v, deformation $D \cdot dr$, and rotation $1/2\nabla(v \times dr)$.
The color pattern indicates the two vorticity orientations:

- blue indicates a negative w and it signifies a clockwise flow rotation.
- red indicates a positive w and it signifies a counterclockwise flow rotation.

According to Lighthill's relations [25], to fulfill the no-slip condition and the solenoidality of the vorticity, the vorticity flux depends only on the pressure change along the wall. This is confirmed by the intense color pattern indicated by the slice taken along the flow direction for each component and by the full visualization of them. Moreover, it is possible to confirm the relations between the wall temperature and the vorticity highlighted by Zhu et al., (2016) [21]. This clarifies how elevated wall temperature, in this case in the lower y/δ direction and close to the ramp corner where the adverse pressure gradient is more evident, enlarges the separated flow region and generates larger scale vortical structures.

4.2 Turbulent statistics

In this section, the post-processing results for each simulation are examined to validate the mean flow visualization and to assess the ability of the equilibrium wall model to produce accurate results, in comparison with DNS reference datasets and the benchmark study by Dawson et al., (2013) [19].

4.2.1 Stretched grid configuration

Grid	Run	$Re_{\tau,in}$	h_{wm}	μ_{eff}
600-250-80	G1ML3	170	3	10-10
800-300-80	G2ML3	170	3	40-40
656-270-80	G3ML3	170	3	10-20
904-350-90	G4ML3	170	3	10-20

Table 3: Simulation configuration used to generate the reference data in this study. Computational meshes ranging from coarse, *G1*, to fine, *G4*, are employed while keeping all input parameters constant.

Table 3 collects all the information related to the input parameters selected for the reference simulations performed in this work. The decision to refine the grid near the beginning of the ramp is made to capture as much of the relevant physics as possible in that region, without changing the fundamental approach of our study, which relies on a wall model rather than a far more accurate but much more expensive direct numerical simulation, Fig. 19.
The matching location was set at the third cell off the wall, which corresponds to the location where the EWM provides the wall shear stress, τ_w, and the wall heat flux, q_w.
A key parameter is the effective viscosity μ_{eff}, 3.3.1: the reported values represent the minimum (negative value) and maximum limits that the simulation must satisfy. Figure 30 shows a comparison between the simulation results obtained in this work and the wall-resolved LES (WRLES) data reported in Dawson et al., (2013) [19]. The results shown in the following graph indicate that the adopted modeling choices are satisfactory, as the overall trend is in good agreement with a Dawson-like behavior. However, near the onset of the ramp, the model fails to reproduce the same C_f distribution. In this region, a negative friction coefficient is expected due to the presence of a recirculation bubble and the strong adverse pressure gradient. Consequently, the EWM is unable to accurately capture this condition. Since the same matching location and Re_τ were chosen as input parameters, it can be observed that the finer grid configurations, *G2ML3* and *G4ML3*, reproduce the C_f trend in the smooth region before the separation point more precisely. The model also predicts the separation point similarly to the WRLES, at approximately $x \approx -4.5\delta$, highlighting its good agreement with the reference solution. In contrast, the coarser grids predict separation upstream of the actual location. Table 4 summarizes the results for each simulation considered. The friction Reynolds numbers Re_τ, C_f, and δ_{99} are evaluated at the reference location, corresponding to the station selected by Dawson, located at $x = -9\delta$ upstream of the ramp onset.
Even if the finer grid, as already mentioned, better reproduces the result behavior

of the case, the coarser grid yields a deviation error $\epsilon_{\%}$ for the C_f close to $10-11\%$. In contrast, the boundary layer thickness is well defined close to 2 for each case. An observation can be made starting from the definition of the friction coefficient:

$$C_f = 2\left(\frac{u_\tau}{U_\infty}\right)^2 \tag{4.4}$$

and, using the definition of Re_τ in 2.37, it is possible to relate these two parameters, highlighting the strong dependence on the equilibrium wall model through the value of the friction velocity u_τ. When comparing the C_f curve with the results presented by Dawson, one can note that the Reynolds friction coefficient differs because the reference boundary-layer thickness is not the same; consequently, C_f changes even if the wall shear stress τ_w is identical.

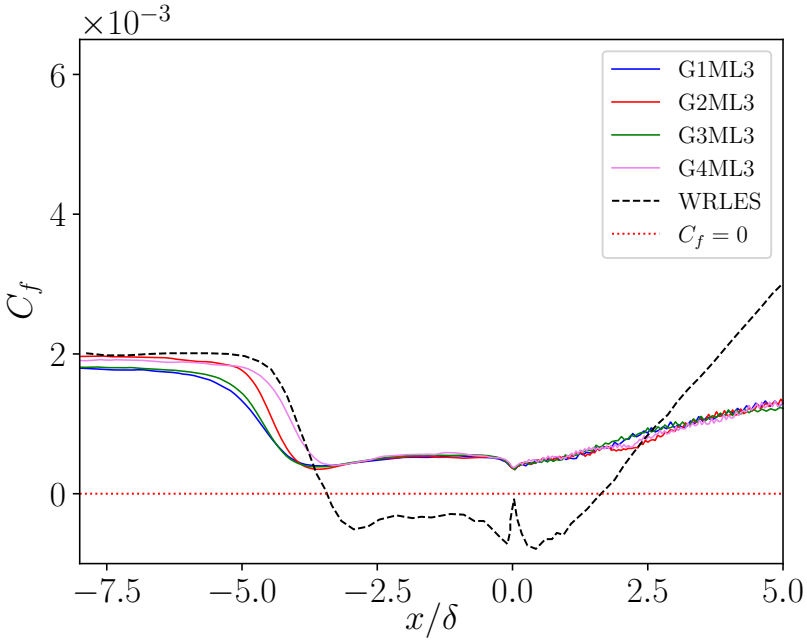

Figure 30: C_f comparison between the WRLES mesh case reported by Dawson et al. (2013) and the grid configuration selected for this study. All tests are scaled to the reference location defined in Dawson et al., (2013): $x = -9\delta$ from the initial ramp location, to enable a consistent comparison.

Grid	Run	Re_τ	C_f	δ_{99}	Δ_x^+	Δ_y^+	Δ_z^+
600-250-80	G1ML3	285	1.79-03	2.13	17.6 - 35.9	11.2 - 22.3	15.1
800-300-80	G2ML3	297.1	1.98e-03	2.11	12.8 - 30.9	10 - 20.1	15.8
656-270-80	G3ML3	280.2	1.80e-03	2.08	15.3 - 32.9	10 - 20.6	15.1
904-350-90	G4ML3	289.1	1.92e-03	2.1	11.4 - 26.7	8.9 - 16.8	13.8

Table 4: Present the results at the reference position, $x = -9\delta$. The data are evaluated at the same matching height, $h_{wm} = 3$. Δ^+ denotes the spatial separation expressed in viscous units.

The final entries in the table report the range of values, Δ^+ for each coordinate, which can therefore be directly compared with those reported by Dawson for the WMLES coarse-mesh and WRLES cases.
From Table 5, it emerges that the present simulations yield Δ_x^+ and Δ_z^+ values that are systematically higher than those reported by Dawson. This increase is consistent with the slightly larger total number of grid points employed in the present work, which shifts the current meshes toward a medium-resolution classification according to Dawson's criteria.
Δ_y^+ values are the more significant ones; although Dawson's mesh case is labeled as coarse, it employs small wall-normal spacings: Dawson's case is so well-resolved that a wall-resolved model is not required, as all the necessary near-wall information is already captured.
In contrast, for the other case it becomes clear that using a wall model is advantageous, although a value of $\Delta_y^+ > 40$ would be preferable for our velocity profile, since the first cell is then located not in the linear region or buffer layer, but likely within the logarithmic layer.

Case	N_{Total}	Δ_x^+	Δ_y^+	Δ_z^+
600-250-80	12M	17.6 - 35.9	11.2 - 22.3	15.1
800-300-80	19.2M	12.8 - 30.9	10 - 20.1	15.8
656-270-80	14.17M	15.3 - 32.9	10 - 20.6	15.1
904-350-90	28.47M	11.4 - 26.7	8.9 - 16.8	13.8
Dawson WM-C	7M	8 - 16	3 - 11	8

Table 5: Comparison between Dawson course mesh results and our simulations for what concern Δ^+ quantities and the total numbers used in the simulations.

Considering the same stretched grid configuration shown in Fig. 19, it is useful to investigate the behavior, accuracy, and possible underestimation of specific WMLES quantities by re-evaluating this mesh setup while varying some of the input parameters.
Tables 6, 7, 8, 9 present all mesh cases with different matching locations and two different values of $Re_{\tau,in}$ examined: It is clear that a lower model's matching location produces better results compared to the mesh grid configuration. In fact, the values of C_f decrease with matching locations, indicating an overestimation of the friction parameter. The same conclusion applies to the input Reynolds friction number, since for the same mesh and matching location, the friction coefficient does not change significantly.
Further confirmation is provided by Fig. 31 and Fig. 32, corresponding to the coarse and fine mesh cases, respectively, where it is clear that the C_f profile is well defined for a lower value of the matching location.
A similar analysis can be carried out by examining the evolution of Re_τ and the boundary layer thickness. Given the strong correlation between these two quantities, one can infer that a higher value of the matching location results in a higher wall shear stress and, consequently, a higher friction velocity.

Run	$Re_{\tau,in}$	h_{wm}	μ_{eff}	C_f	Re_τ	δ_{99}	Δx^+	Δy^+	Δz^+
G1ML10	190	10	10-20	2.84e-3	369	1.91	25.2-51.4	16-32	21.7
G1ML10	170	10	10-10	2.9e-3	327	1.92	22.3-45.4	14.2-28.2	19.1
G1ML6	190	6	10-30	2.9e-3	371	1.88	25.7-52.4	16.4-32.6	22.1
G1ML6	170	6	10-20	2.9e-3	336	1.97	22.4-45.6	14.3-28.3	19.2
G1ML4	190	4	10-20	2.2e-3	343	2.01	22.3-45.4	14.2-28.2	19.1
G1ML4	170	4	20-30	2.3e-3	309	2.04	19.8-40.5	12.8-25	17

Table 6: *G1* simulation setup and results with different values of h_{wm} and Re_τ.

Run	$Re_{\tau,in}$	h_{wm}	μ_{eff}	C_f	Re_τ	δ_{99}	Δx^+	Δy^+	Δz^+
G2ML10	190	10	10-20	3e-3	373.5	1.88	18.1-43.6	14.2-28.4	22.3
G2ML10	170	10	10-20	3.0e-3	331.5	1.89	16-38.4	12.5-24.3	19.6
G2ML6	190	6	10-20	2.84e-3	373.9	1.93	17.6-42.4	13.8-27.6	21.7
G2ML6	170	6	10-20	2.8e-3	337	1.98	15.5-37.3	12.2-24.3	19.1
G2ML4	190	4	10-20	2.27e-3	343.9	1.99	15.8-37.9	12.4-24.7	19.4
G2ML4	170	4	20-30	2.3e-3	310.74	2.03	13.9-33.5	10.9-21.8	17.2

Table 7: *G2* simulation setup and results with different values of h_{wm} and Re_τ.

Run	$Re_{\tau,in}$	h_{wm}	μ_{eff}	C_f	Re_τ	δ_{99}	Δx^+	Δy^+	Δz^+
G3ML10	190	10	10-20	2.9e-3	367.5	1.85	22.6-48-5	14.8-30.3	22.2
G3ML10	170	10	10-20	3.0e-3	337	1.93	19.9-42.8	13.1-26.8	19.6
G3ML6	190	6	10-20	2.8e-3	372	1.92	22-47.5	14.5-29.7	21.7
G3ML6	170	6	10-20	2.8e-3	327	1.92	19.4-41.7	12.7-26	19.1
G3ML4	190	4	10-20	2.2e-3	341	2.00	19.4-41.7	12.77-26.1	19.1
G3ML4	170	4	10-20	2.2e-3	307.8	2.04	17-36.9	11.3-23	16.9

Table 8: *G3* simulation setup and results with different values of h_{wm} and Re_τ.

Run	$Re_{\tau,in}$	h_{wm}	μ_{eff}	C_f	Re_τ	δ_{99}	Δx^+	Δy^+	Δz^+
G4ML10	190	10	20-30	3.0e-3	374.7	1.88	16.4-38.4	12.8-24.2	19.9
G4ML10	170	10	10-20	3.0e-3	334.1	1.91	14.4-33.7	11.2-21.3	17.5
G4ML6	190	6	10-20	2.78e-3	365.3	1.91	15.7-36.8	12.3-23.2	19.1
G4ML6	170	6	10-20	2.8e-3	334.4	1.98	13.9-32.5	10.8-20.5	16.8
G4ML4	190	4	10-20	2.2e-3	341	1.99	14.1-33.0	11.0-20.8	17.1
G4ML4	170	4	20-30	2.2e-3	303	2.02	12.3-28.9	9.6-18.2	15

Table 9: *G4* simulation setup and results with different values of h_{wm} and Re_τ.

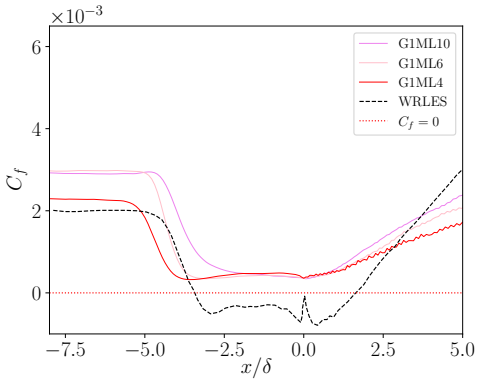

(a) C_f comparison in the case of mesh **G1** at different matching location with an input $Re_\tau = 170$.

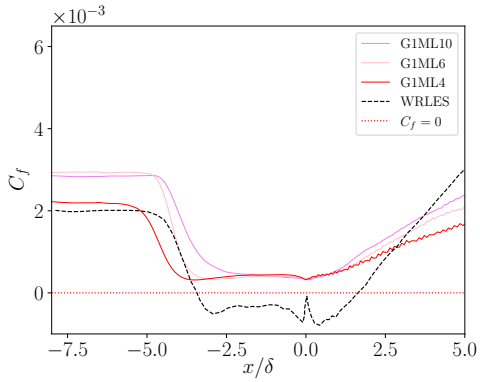

(b) C_f comparison in the case of mesh *G1* at different matching location with an input $Re_\tau = 190$.

Figure 31: C_f comparison in the case of mesh **G1** at different matching location $h_{wm} = 10, 6$ and 4 with an input $Re_\tau = 170, 190$.

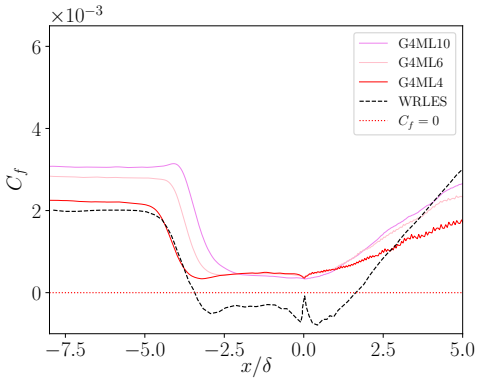

(a) C_f comparison in the case of mesh *G4* at different matching location with an input $Re_\tau = 170$.

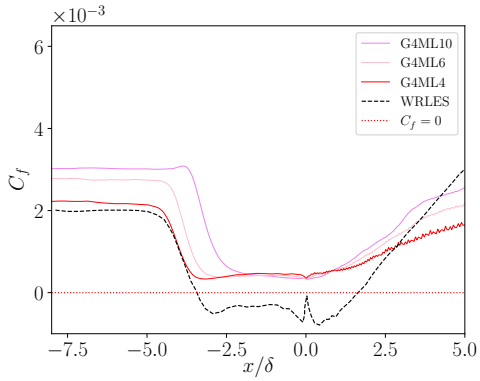

(b) C_f comparison in the case of mesh *G4* at different matching location with an input $Re_\tau = 190$.

Figure 32: C_f comparison in the case of mesh **G4** at different matching location $h_{wm} = 10, 6$ and 4 with an input $Re_\tau = 170, 190$.

Therefore, the WMLES approach produces substantial errors in the prediction of skin friction in the separation and recovery regions. This behavior was expected because the wall model is formulated for equilibrium boundary layers, whereas STBLI is a strongly non-equilibrium phenomenon.
Furthermore, information at the matching location is transferred to the wall exclusively in the wall-normal direction through the wall-model equations, owing to their ODE character and the limited connectivity of the model. Consequently, the near-wall information transfer exhibits reduced directionality, and effects that are intrinsically aligned with the wall, such as pressure gradients, are not represented. In non-equilibrium flows, where variations parallel to the wall are crucial in the near-wall region, it is therefore inappropriate to expect equilibrium boundary layer formulations to yield accurate skin-friction predictions, particularly for separation and reattachment locations.

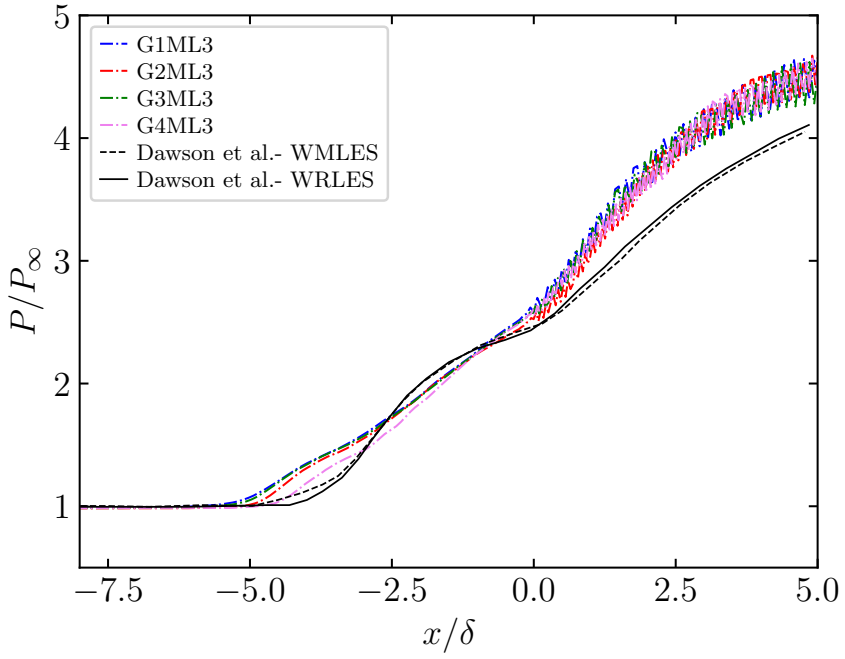

(a)

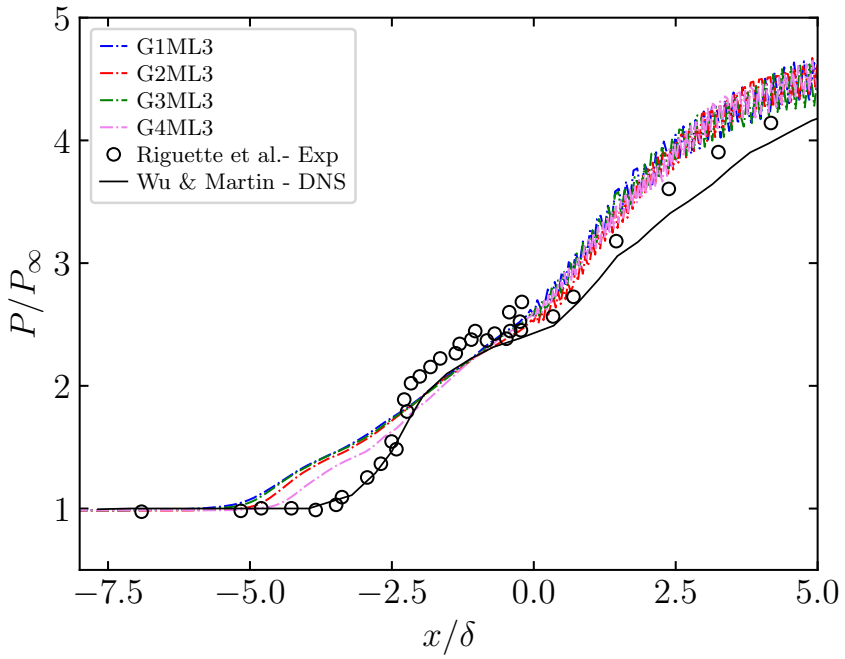

(b)

Figure 33: Mean wall-pressure p/p_∞ distribution comparison with respect to (a) WMLES (dashed black line) and WRLES (solid black line) Dawson's data and (b) the experimental results of Riguette et al., (2009) (black circle), and the DNS by Wu & Martin (2008) (black line).

Figure 33 presents the mean wall-pressure distribution to validate the findings obtained from the C_f graphs. The comparison is made with Dawson's reference data for both WRLES and WMLES, together with the experimental measurements of Riguette et al. (2009)[14] and the DNS results [13] and it reveals a similar behavior only from a qualitative point of view. Starting with the smooth region in the domain where the pressure gradient is null, the model works perfectly with respect to the comparison data. Then, a pressure increase is present all along the last part of the smooth region close to the ramp corner, where it is possible to define the separation point. Also, an inflection point at approximately $x/\delta = -2.5$ in the shock oscillation region is present establishing a downstream plateau. These aspects are better captured by the finer grid configuration, *G4*, even though all of the simulations are affected by an overestimation of the mean pressure distribution in the region after the separation point and do not accurately reproduce the plateau where a strong adverse pressure gradient is expected, resulting in a negative C_f. Moreover, numerical instabilities and limited accuracy in the ramp region are present, defining how the model does not correctly reproduce the reattachment region of the flow. The increase in pressure immediately downstream of the ramp corner at $x/\delta = 0$ can be explained by the presence of a succession of compression waves propagating toward the wall.

4.2.2 Oblique shock wave

Regarding the analysis of the oblique shock wave generation due to the flow encountering a compression ramp along its path, it is possible to compare the oblique shock angle derived from the simulations with the theoretical value.
Starting from the input parameters in this case study:

- free-stream Mach number $M_1 = 2.9$,
- ramp angle $\theta = 24°$,
- specific heat ratio for calorically-perfect gasses $\gamma_{air} = 1.4$,

and according to the theoretical framework discussed in 2.1.2, two distinct mathematical solutions can be found for the shock wave inclination, denoted as β_s and β_w:

- $\beta_s = 79.53°$,
- $\beta_w = 43.67°$.

Additional confirmation is obtained from the graphical solution, C, and from this stage onward, exploiting the known characteristics of the normal shock, one can determine the relevant ratios that may arise in this case.
From Eq. 2.13, the wall-normal Mach number in the upstream region can be computed, and through the gas-dynamic table for a normal shock wave, the downstream normal Mach number, Mn_2, is readily obtained. By subsequently applying Eq. 2.16, the corresponding value of M_2 is determined.
Assuming the weak solution, the results are:

$$Mn_1 = 2,$$

$$\frac{P_2}{P_1} = 4.5, \quad \frac{\rho_2}{\rho_1} = 2.667, \quad \frac{T_2}{T_1} = 1.687, \quad \frac{P_{0,1}}{P_{0,2}} = 0.7209, \quad Mn_2 = 0.5774,$$

$$M_2 = 1.715.$$

The shock is defined as a mathematical discontinuity across which the fluid properties change. It represents a strongly entropic phenomenon, and for this reason, it is convenient to characterize it using the pressure gradient:

$$px_{i,j} = \left.\frac{\partial p}{\partial x}\right|_{(x_i,x_j)} \tag{4.5}$$

since the pressure varies from a lower value downstream of the shock to a higher value upstream. The spatial derivative ∇p therefore exhibits a very sharp peak, reflecting the almost instantaneous nature of this change. Figure 34 illustrates different shock wave zones along the y direction in this case study, and from this, the evaluation is done from the collision point of the shock zone. Therefore, Fig. 35 presents the interpolation curves passing through the maximum values of the shock, evaluated within a region of interest along the y direction. This region is chosen to be sufficiently distant from the wall and from any instabilities or effects associated with flow recirculation near the ramp, where the shock is not clearly defined.

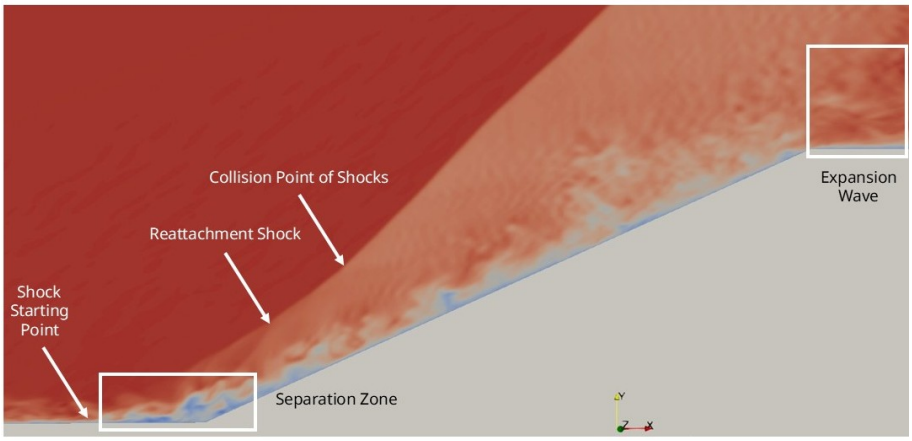

Figure 34: Schematic illustration of the oblique shock wave that is produced by the compression ramp. Main points and zone are reported.

If j denotes the index in the y direction, this operation yields:

$$\left[\frac{\partial p}{\partial x}(x_1, y_j),\ \frac{\partial p}{\partial x}(x_2, y_j)\ ...\right] \tag{4.6}$$

Along the y-direction, the peak value of px indicates the locations of the shocks and corresponds to the positions highlighted by the red dots in Figure 35. The representation quality of the oblique shock is ensured by using contour levels, chosen to balance spatial resolution with visual clarity. Moreover, to evaluate the oblique shock angle β, the median of the x_i coordinates of the shock points is computed, and a range of $\pm 2\sigma$ is applied to obtain a more clearly defined shock. An interpolation is then performed to connect all the selected points that provide an accurate representation of the shock line.
Table 10 presents the shock-angle values obtained both from the numerical analysis and from theoretical predictions. The percentage deviation, Eq. 4.7, of the numerical results from the theoretical ones is contained within 2%, which corresponds to a discrepancy of roughly one degree. On the basis of these findings, and consistently with the graphical representation of the $\theta - \beta - M$ theory C, it can be stated that the simulations carried out provide an accurate reproduction of the phenomenon under investigation.

Oblique shock angle	Theory	G1ML3	G2ML3	G3ML3	G4ML3	ϵ%
β	43.67°	44.45°	44.75°	44.44°	44.80°	2

Table 10: Comparison between theoretical oblique shock angle and the ones from simulation.

$$\epsilon_\beta = \left|\frac{\beta_{theory} - \beta_{test}}{\beta_{theory}}\right| \cdot 100\% \tag{4.7}$$

Regarding the properties of the flow as it passes through the oblique shock, the analyses used to determine the ratio between the upstream and downstream conditions of this phenomenon are defined as follows:

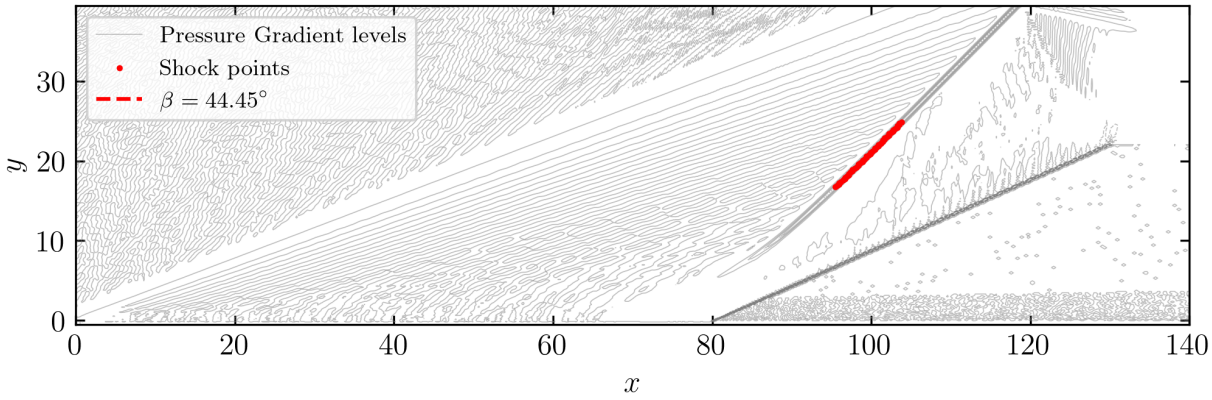

(a) *G1ML3* oblique shock angle $\beta = 44.45°$.

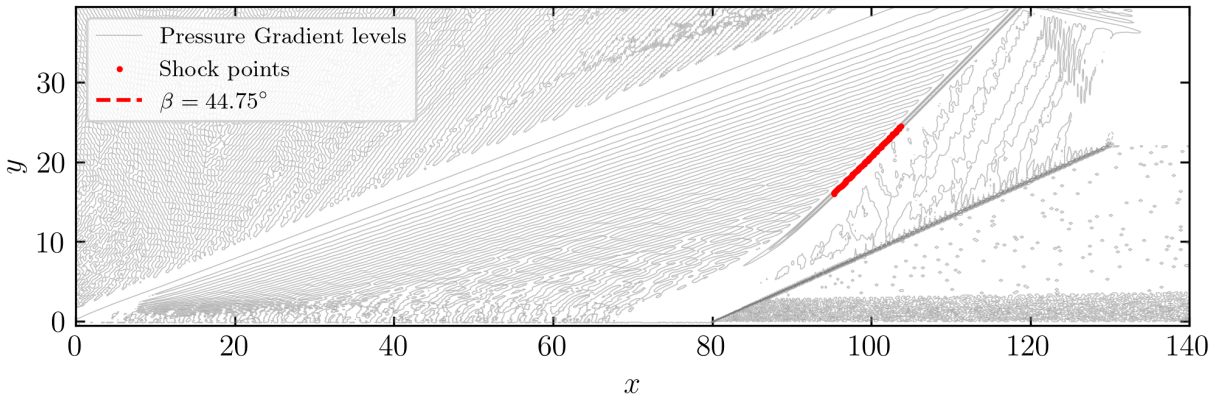

(b) *G2ML3* oblique shock angle $\beta = 44.75°$.

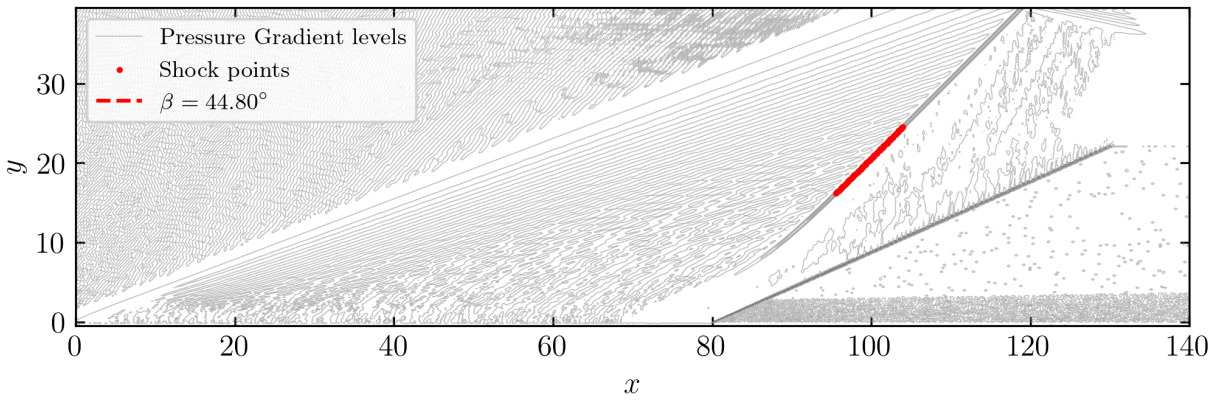

(c) *G4ML3* oblique shock angle $\beta = 44.80°$.

Figure 35: Oblique shock angles for 3 analyzed cases: *G1* is the coarse mesh, *G2* is the medium case and *G4* the fine mesh configuration. Each of these cases are evaluated for an input $Re_\tau = 170$ ad a matching location $h_{wm} = 3$. The pressure gradient contour levels of 20 to better highlight the trajectory of the oblique shock. The red points and the interpolation curve are defined in a region sufficiently distant from the recirculation zone near the beginning of the ramp.

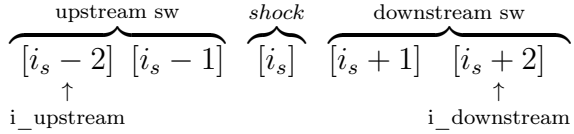

The grid coordinates sketch represented is useful to visualize how the code can read the values and then evaluate the position of the shock through the mesh grid. The shock is located by its coordinates i_s, which are considered as the central coordinates that identify the shock wave. The upstream and downstream quantities are defined by selecting positions that are a certain number of cells away from the shock location. This is necessary because if the upstream and downstream points are chosen as the immediately adjacent cells, i.e., at $i_s - 1$ and $i_s + 1$, the code may fail to capture the undisturbed values of these quantities, as they would still lie within the shock region. To avoid this and ensure reliable results, the properties are evaluated at a distance of $n = 5$ cells from the shock position i_s, so that the chosen points are no longer in the transition zone.

Property ratio	Theory	G1ML3	G2ML3	G3ML3	G4ML3	ϵ%
p_2/p_1	4.5	4.65	4.69	4.65	4.66	3-4
ρ_2/ρ_1	2.66	2.72	2.72	2.72	2.71	2
T_2/T_1	1.68	1.71	1.72	1.71	1.72	2

Table 11: Comparison flow property ratio between the theoretical and simulation values.

Table 11 reports the flow properties in terms of the ratios of pressure, density, and temperature between the regions upstream and downstream of the shock wave. By examining the percentage deviation, as defined in Eq. 4.7 for the oblique shock angle, of these quantities with respect to the theoretical reference values, it is possible to note that the model performs well in reproducing the discontinuities in these properties. A deviation of approximately $\approx 2\%$ for both density and temperature can be regarded as acceptable. Since the pressure ratio is obtained as the product of density and temperature ratios:

$$\frac{p_2}{p_1} = \frac{\rho_2}{\rho_1} \cdot \frac{T_2}{T_1}, \tag{4.8}$$

the associated errors in these previous quantities combine, leading to an overall deviation in pressure of about $\approx 3 - 4\%$.
Regarding the Mach number of the oblique shock wave downstream region, it is possible to determine it based on the oblique shock angle and the relevant flow properties, as has already been done, in order to verify the results from this perspective, Table 12.

Mach number	Theory	G1ML3	G2ML3	G3ML3	G4ML3	ϵ%
M_2	1.715	1.652	1.629	1.653	1.6259	3-5

Table 12: Comparison Mach number values with respect to the theoretical one.

4.2.3 Boundary layer thickness

In this section, the boundary-layer thickness of the profile is presented for various stations along the domain. This is done to evaluate the mean velocity profile and to better understand the influence of an adverse pressure gradient, as well as how this profile aligns with the behavior observed in the compression ramp study and thus, the formation of a recirculation region near the start of the ramp itself and the generation of the oblique shock.
The reported profiles are chosen to assess the transition from the initial smooth-wall freestream condition at the start of the domain and how this changes due to the jump, as well as how this can be confirmed through a gas-dynamic description of the phenomenon. Subsequently, the graphs illustrate the behavior of the turbulent boundary layer recovering its characteristic shape along y/δ direction far from the wall.
For this presentation, all assessed grid configurations are included, from the coarsest, *G1*, to the finest, *G4*, using the same matching location $h_{wm} = 3$. The various plots are compared against the reference data of Dawson et al. [19], the experimental measurements of Riguette et al. (2009) [14], and the DNS results of Wu & Martin (2008) [13], in order to validate and evaluate the quality of the present results.

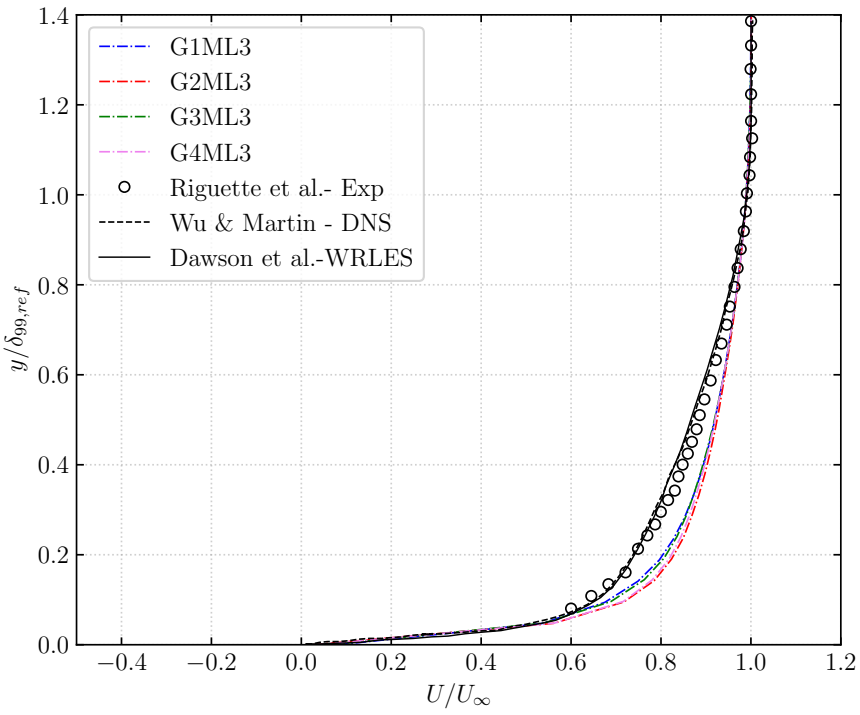

Figure 36: Mean streamwise velocity profile at the reference position $x/\delta = -9$, measured from the ramp corner. The solid black circles represent the experimental data of Ringuette et al. (2009) at $M_\infty = 3$, while the black dashed line shows the DNS results of Wu & Martin (2008) at $M_\infty = 2.9$. The solid black line is the WRLES case defined by Dawson et al,. (2013). The colored dash-dotted curves correspond to the cases examined in this study, which employ different grid configurations but share the same input parameters: Re_τ and h_{wm}.

The velocity is normalized using the free-stream value, U_∞. This reference value is obtained through a two-dimensional interpolation to determine a velocity sufficiently far from the wall, where the boundary layer has recovered 99% of the free-stream velocity. A different method is adopted for evaluating the free-stream velocity after the oblique shock, due to the gas-dynamic effects governing this phenomenon. Since U_∞ changes across the shock, a "safe zone" is implemented in the code to accurately capture the post-shock profile. This zone is chosen to be adequately distant from the shock to avoid its direct influence while also remaining outside the boundary-layer region.
Regarding the results shown in Figure 36, concerning the situation before the shock wave, a good agreement can be observed between the present outcomes and the reference values from both DNS and experimental data.
In Fig. 37, the influence of an adverse pressure gradient on the development of the turbulent boundary layer is visible, as an incipient separation is represented. This confirms the behavior described in Section 2.3, where the boundary layer thickness δ increases, corresponding to a thinner velocity profile near the wall. Furthermore, the opposite direction of the near-wall velocity with respect to the free-stream is supported by these plots: the change in concavity indicates a recirculation region in the flow close to the ramp corner.
Figure 37f shows the evolution of the mean streamwise velocity downstream of the ramp corner, where the flow gradually returns to a behavior similar to that observed in the smooth region of the domain. The curvature changes once more, and the thickness δ decreases.
It is important to highlight how the modeling of the inner region close to the wall, together with the influence of the IBM configuration implemented in the solver, makes it necessary to account for the first fluid cell near the wall.
This confirms that the near-wall region is not directly resolved by an EWM and, as a consequence, the physics of the boundary layer itself is not adequately captured. Nevertheless, the set of figures presented shows that the mean streamwise velocity is generally well reproduced.
In particular, for the case illustrated in Fig. 38, data from Riguette et al. (2009) [14] and from DNS [13] are presented for stations located downstream of the ramp corner. This is done to highlight that the gradual decrease in the boundary layer edge velocity from $x = 4\delta$ to $x = 8\delta$ corresponds to the gradual pressure rise observed in the surface-pressure distribution, Fig. 33, indicating that the flow at these locations is still turning and decelerating in the final stages of the compression.
These plots underscore the limitations in capturing the correct near-wall behavior of δ and show how the model fails to accurately reproduce the profile, instead predicting an excessively large value of δ. The two finer grids, *G2* and *G4*, replicate the shape of the reference data used to validate the mean velocity profile more faithfully, even though their differences from the coarser grids are not very pronounced.

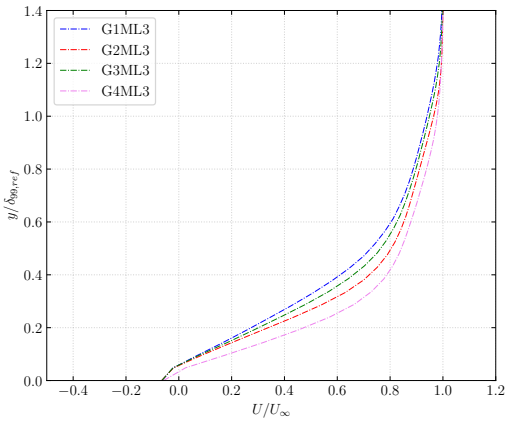

(a) Mean streamwise velocity at station $x/\delta = -3$.

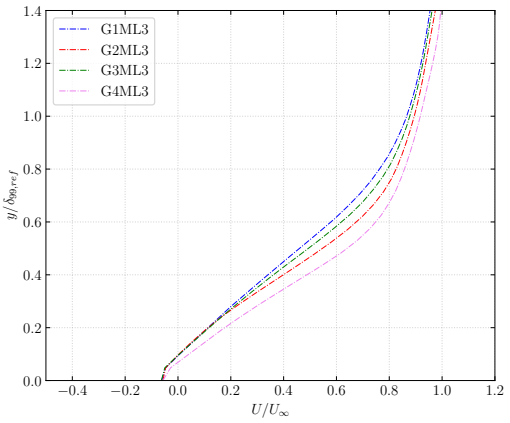

(b) Mean streamwise velocity at station $x/\delta = -2$.

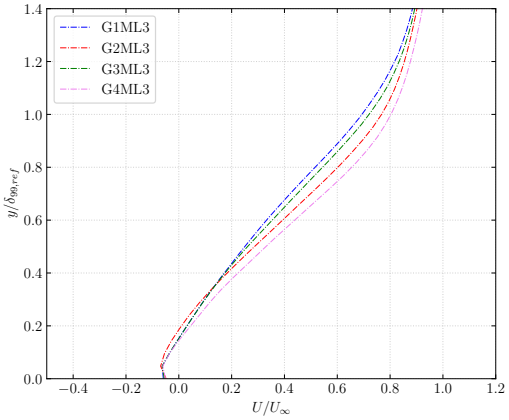

(c) Mean streamwise velocity at station $x/\delta = -1$.

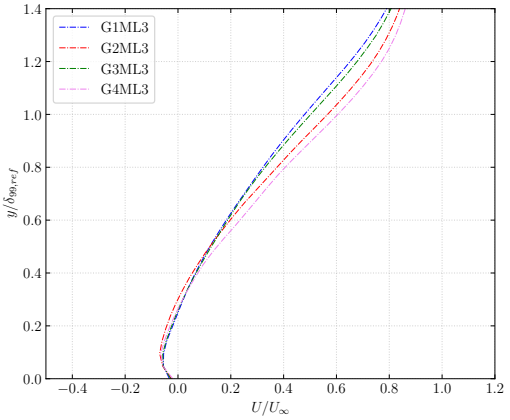

(d) Mean streamwise velocity at station $x/\delta = 0$.

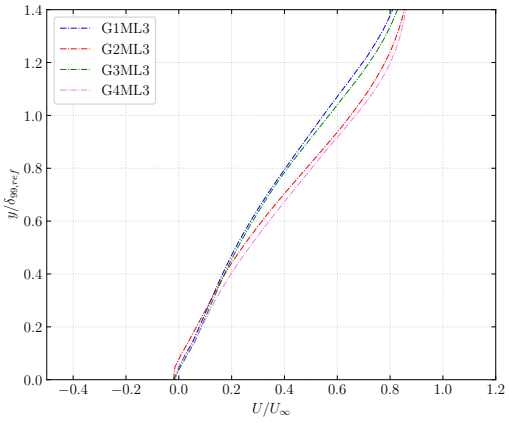

(e) Mean streamwise velocity at station $x/\delta = 1$.

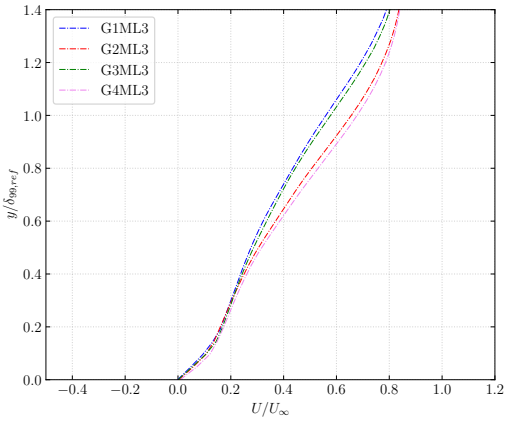

(f) Mean streamwise velocity at station $x/\delta = 2$.

Figure 37: Mean streamwise velocity profiles at various streamwise positions x/δ within our domain of interest, shown both upstream and downstream of the ramp corner, are presented relative to the reference position at $x/\delta = 80$, which corresponds to $x/\delta = 0$ in Dawson et al. (2013).

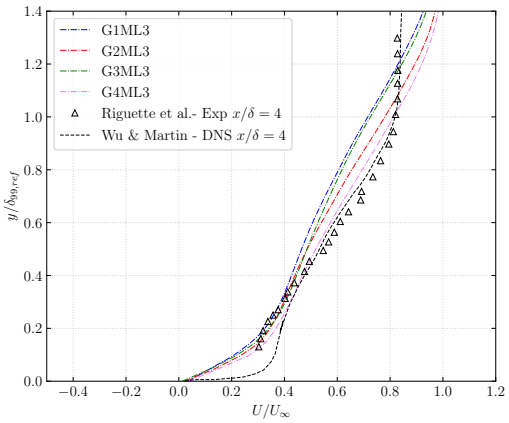

(a) Mean streamwise velocity at station $x/\delta = 4$.

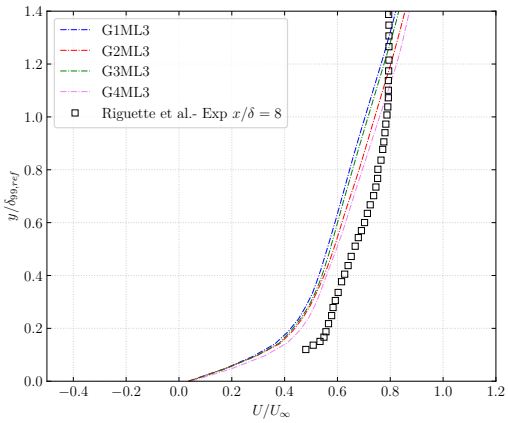

(b) Mean streamwise velocity at station $x/\delta = 8$.

Figure 38: Mean streamwise velocity profiles at two different streamwise stations: panel (a) shows the profiles compared against two data sets, namely the experimental measurements of Riguette et al,. (2009), plotted as black triangles, and the DNS results of Wu & Martin (2008), shown as a black dashed line, both at $x/\delta = 4$.Panel (b) shows the profile at $x/\delta = 8$, for which only the data set from Riguette et al. (2009), indicated by black squares, is available.

5 Conclusions

The analysis of a compressible turbulent boundary layer over a compression ramp using a wall model implemented in the open numerical solver STREAmS, with an IBM model to implement the boundary condition, was tested, highlighting the advantages and limitations of this approach compared to other numerical methods for investigating flow behavior. Considering the setup used for this work and the constraints imposed for the simulation, a good agreement of the data is shown. The emergence of changes in flow properties across the oblique shock wave is well captured, as demonstrated by the concordance between mean flow visualizations and statistical analyzes when compared with the theoretical values. The error is under the $\epsilon_{prop} = 4\%$ for the properties, and the shock wave oblique angle identification is approximately $\epsilon_{\beta} = 2\%$.
A systematic comparison was carried out with the reference WMLES and WRLES of Dawson et al. (2013) [19], the experimental data of Riguette et al. (2009) [14], and the DNS of Wu & Martin [13] in order to validate the obtained simulation results. The friction coefficient along the smooth part of the domain is well captured, indicating the importance of the model's matching location over the grid configuration.
In contrast, the EWM does not adequately represent the non-equilibrium state associated with the separation and recovery zones during a strong adverse pressure event, highlighting its inaccurate prediction of skin friction. This is further confirmed by the mean wall-pressure distribution, as the model does not capture the correct inflection point of the separation region and exhibits significant instabilities along the ramp portion of the domain.
The discrepancy in the correct evaluation of the reference boundary layer thickness leads to different values of the Reynolds friction number and the viscous spatial separation, meaning that the model does not accurately capture the right wall shear stress coefficient with respect to Dawson's.
This behavior was expected because the wall model is formulated for equilibrium boundary layers, whereas STBLI is a strongly non-equilibrium phenomenon. Moreover, at the matching location, information is communicated to the wall solely in the wall-normal direction via the wall-model equations, due to their ODE-based formulation and the model's limited connectivity. As a result, the transfer of near-wall information becomes less directional, and phenomena that are inherently oriented along the wall, such as pressure gradients, are not captured. In non-equilibrium flows, where variations parallel to the wall play a key role in the near-wall region, it is therefore unreasonable to expect equilibrium boundary layer models to provide reliable skin-friction predictions, especially for separation and reattachment locations.
Because an IBM is implemented within the WMLES to simplify grid generation, it is necessary to introduce ghost nodes and impose wall-related boundary conditions. This, however, leads to an inaccurate representation of the mean velocity profile, as the near-wall region is not correctly resolved. Overall, the boundary layer is well captured in both the pre-shock and post-shock regions, underlining the effect of an adverse pressure gradient acting along the domain.
For future analysis, a possible improvement of WMLES in the numerical solver STREAmS, along with IBM, could be made by considering a dynamic matching

height that effectively turns off the wall model in regions of strong non-equilibrium while simultaneously utilizing local grid refinement to better resolve the near wall region in those areas. In this way, the method might switch between wall modeled LES of equilibrium conditions and locally refined, wall resolved LES of non-equilibrium conditions. For practical aerospace applications, it is important to extend the analysis to higher Mach and Reynolds numbers, as well as to consider the possibility of a rough surface to provide further validation of the WMLES. In conclusion, the thesis confirms the potential of WMLES as an effective tool for simulating turbulent boundary layers interacting with compression ramps. However, predictive accuracy remains dependent on wall-model assumptions and grid resolution, and additional methodological refinement is required for complex turbulent flows.

A Thermodynamic

Consider the relationship between internal energy e and enthalpy h:

$$e(T,p), h(T,p) \quad \rightarrow \quad h = e + \frac{p}{\rho} \tag{A.1}$$

In the presence of a perfect gas, the internal energy and enthalpy are only a function of the temperature T. Then the two quantities can be written as follow:

$$de = c_v(T)dT, \quad dh = c_p(T)dT \tag{A.2}$$

Considering a calorically perfect gas, the specific heat quantities c_p and c_v are constant:

$$e = c_v T, \quad h = c_p T \tag{A.3}$$

and then:

$$h = c_p T = e + \frac{p}{\rho} \quad \rightarrow \quad c_p T = c_v + RT \quad \rightarrow \quad c_p - c_v = R \tag{A.4}$$

Dividing by c_v, the equation gives γ:

$$\underbrace{\frac{c_p}{c_v}}_{\gamma} - 1 = \frac{R}{c_v} \quad \rightarrow \quad c_v = \frac{R}{\gamma - 1}, \quad c_p = \frac{\gamma}{\gamma - 1}R \tag{A.5}$$

It's worth considering the principles of thermodynamics.

- **First principle of thermodynamic**:
  Taking a system with a certain level of internal energy e, the variation of energy occurs for two reasons:
  - heat exchange,
  - work done on the system.

  Both are taken as positive quantities for conservation if they enter the system.

  $$de = \delta q + \delta w \tag{A.6}$$

  Its application is important in the following three cases:
  1. Adiabatic transformation $\delta q = 0$
  2. Reversible transformation $\delta w_{|REV} = -pd(\frac{1}{\rho})$
  3. Isenthalpic transformation

- **Second principle of thermodynamic**:
  This principle is based on the definition of the state function called entropy, $S(T,P)$:

  $$dS = \frac{dq_{|REV}}{T} \Leftrightarrow S_2 - S_1 = \int_1^2 \frac{dq_{|REV}}{T} \tag{A.7}$$

The change in entropy between two states is greater than or equal to the value given by the integral expression. For a perfect gas, the evaluation of e and h, based on the definition

$$TdS = dq_{|REV} \quad \rightarrow \quad dq_{|REV} = 0 \quad \rightarrow \text{Isenthalpic Transformation} \tag{A.8}$$

follows from this relationship. Then

$$de = dq_{|REV} + dw_{|REV} = TdS - pd\left(\frac{1}{\rho}\right) \tag{A.9}$$

$$dh = de + d\left(\frac{p}{\rho}\right) = TdS - pd\left(\frac{1}{\rho}\right) + pd\left(\frac{1}{\rho}\right) + \frac{1}{\rho}dp \tag{A.10}$$

The entropy of a perfect gas is:

$$c_p dT = TdS + \frac{1}{\rho}dp \quad \rightarrow \quad dS = cp\frac{dT}{T} - \frac{1}{\rho T}dp \quad \rightarrow \quad dS = cp\frac{dT}{T} - \frac{dp}{p}R \tag{A.11}$$

Then

$$S_2 - S_1 = c_p \ln\frac{T_2}{T_1} - R\ln\frac{p_2}{p_1} \tag{A.12}$$

Entropy expressed as a function of temperature and density, $S(T, \rho)$:

$$\frac{p_2}{p_1} = \frac{\rho_2 T_2}{\rho_1 T_1} \quad \rightarrow \quad S_2 - S_1 = c_v \ln\frac{T_2}{T_1} - R\ln\frac{\rho_2}{\rho_1} \tag{A.13}$$

To wrap up this section, the expression describing an isoenthalpic process can be written as:

$$\frac{p_2}{p_1} = \left(\frac{\rho_2}{\rho_1}\right)^{\gamma} = \left(\frac{T_2}{T_1}\right)^{\frac{\gamma}{\gamma-1}} \tag{A.14}$$

These relationships are not valid in aerodynamics:

1. In the presence of heat exchange, there are no adiabatic conditions.
2. Dissipative phenomena include thermal diffusion and viscosity.

It is not applicable within the boundary layer due to viscous effects: heat is transferred between the flow and the wall through this region. The connection between a shock wave and a compressible fluid is characterized as a dissipative phenomenon.

B Navier-Stokes equations

Fluid mechanics is described by the Navier-Stokes equations, which express the conservation of mass, momentum balance, and energy for Newtonian fluids.

B.1 Divergence theorem

Considering a chosen volume v, the divergence theorem states:

$$\int_{\partial v} \mathbf{F} \cdot \hat{n} dS = \int_{v} \vec{\nabla} \cdot \mathbf{F} dv \tag{B.1}$$

where ∂v is the edge of the volume, $\mathbf{F}$ is a tensor of at least first order and $\hat{n}$ is the normal to the surface element dS.

B.2 Reynolds transport theorem

Taking a system of fluid particles in the volume v_s and evaluating it in different time instants $v_s(t) \neq v_s(t+dt)$. Assuming the control volume is exactly the one at the instant t, we have $v_s(t) = v_c$ and the two quantities of interest are:

- $\mathbf{B}$ extensive.
- $\mathbf{b}$ intensive.

The Reynolds transport theorem states that:

$$\frac{d}{dt}\mathbf{B} = \frac{d}{dt}\int_{v_{s(t)}} \rho \mathbf{b} dv = \frac{d}{dt}\int_{v_c} \rho \mathbf{b} dv + \int_{\partial v_c} \rho \mathbf{b} \vec{V} \cdot \hat{n} dS \tag{B.2}$$

This theorem allows to build a relationship between a physical law and the control volume v_c which is fixed over time, by adding a flux term that takes into account the quantities going in and out the frontiers.

B.3 Mass conservation equation

The law of conservation of mass states that the time variation of mass in a system has to be zero:

$$\frac{d}{dt} m_s = 0, \quad where \quad m_s = \int_{v_s(t)} \rho dv \quad \& \quad v_c = v_s(t) \tag{B.3}$$

Applying the Reynolds transport theorem B.2:

$$\frac{d}{dt} m_s = 0 = \frac{d}{dt}\int_{v_s(t)} \rho dv = \frac{d}{dt}\int_{v_c} \rho dv + \int_{\partial V_c} \rho \vec{V} \cdot \hat{n} dS \tag{B.4}$$

Then applying the divergence theorem B.1 to the second integral sign and taking the time derivative inside the integral sign due to the fact that v_c is time independent:

$$\int_{v_c} \frac{\partial \rho}{\partial t} dv + \int_{v_c} \vec{\nabla} \cdot (\rho \vec{V}) dv = \int_{v_c} \left[\frac{\partial \rho}{\partial t} + \vec{\nabla} \cdot (\rho \vec{V}) \right] dv = 0 \tag{B.5}$$

Since B.5 is valid for every v_c, then the integral sign can be omitted and the mass balance equation can be written the differential form, called conservative form:

$$\frac{\partial \rho}{\partial t} + \vec{\nabla} \cdot (\rho \vec{V}) = 0 \tag{B.6}$$

B.4 Momentum conservation

The second dynamic law says that the external force acting on a body $\vec{F_e}$, both volume forces $\vec{F_v}$ and surface forces $\vec{F_s}$ is equal to the momentum system $\vec{Q_s}$ variation over time:

$$\frac{d}{dt}\vec{Q_s} = \vec{F_e} \quad where \quad \vec{Q_s} = \int_{v_s(t)} \rho \vec{V} dv \tag{B.7}$$

Applying B.2:

$$\frac{d}{dt}\int_{v_s(t)} \rho \vec{V} dv = \frac{d}{dt}\int_{v_c} \rho \vec{V} dv + \int_{\partial v_c} \rho \vec{V}\vec{V}\hat{n} dS = \vec{F_{e,v}} + \vec{F_{e,s}} \tag{B.8}$$

where the two external force elements can be expressed as follow:

$$Volume \;\; Force \quad d\vec{F_{e,v}} = \rho \vec{f} dv \tag{B.9}$$

$$Surface \;\; Force \quad d\vec{F_{e,s}} = \vec{t}_{(\hat{n})} dS = \vec{\vec{T}} \cdot \hat{n} dS \tag{B.10}$$

For Newtonian fluids a constitutive relation between the stress tensor $\vec{\vec{T}}$ and the velocity gradient exists:

$$\vec{\vec{T}} = -p\vec{\vec{I}} + 2\mu\vec{\vec{E}} - \frac{2}{3}\mu(\vec{\nabla} \cdot u)\vec{\vec{I}} = -p\vec{\vec{I}} + \vec{\vec{\sum}} \tag{B.11}$$

where $\vec{\vec{I}}$ is the identity matrix, $\vec{\vec{E}} = \frac{1}{2}(\vec{\nabla}\vec{V} + \vec{\nabla}\vec{V}^T)$ is the deformation tensor and $\vec{\vec{\sum}}$ is the viscous stress tensor.
Applying B.1 and again removing every integral sign because of the same v_c, the momentum conservation equation in the conservative form is derived:

$$\frac{\partial \rho \vec{V}}{\partial t} + \vec{\nabla} \cdot (\rho \vec{V}\vec{V}) = \rho \vec{f} - \vec{\nabla} p + \vec{\nabla} \cdot \vec{\vec{\sum}} \tag{B.12}$$

B.5 Energy conservation

Applying the first principle of thermodynamic **??** and considering a time variation is possible to define the system energy:

$$E_s = \int_{v_s(t)} \rho \left(e + \frac{V^2}{2} \right) \tag{B.13}$$

where e is the internal energy and $\frac{v^2}{2}$ the kinematic energy per unit mass. Then by applying B.2:

$$\frac{d}{dt}E_s = \frac{d}{dt}\int_{v_s(t)} \rho \left(e + \frac{V^2}{2} \right) dv = \dot{Q}_v + \dot{Q}_s + \dot{W}_v + \dot{W}_s \tag{B.14}$$

where the heat and work contributes have been separated in volume and surface terms, using the Fourier law $\vec{q} = -k\vec{\nabla}T$:

$$d\dot{Q}_v = \rho \dot{Q} dv, \quad d\dot{Q}_s = -\vec{q} \cdot \hat{n} dS = k\vec{\nabla}T \cdot \hat{n} dS \tag{B.15}$$

$$d\dot{W}_v = \vec{V} \cdot (\rho\vec{f})dv = \rho\vec{V} \cdot \vec{f}dv, \quad d\dot{W}_s = \vec{V} \cdot \vec{t}_{\hat{n}}dS = \vec{V} \cdot \vec{\vec{T}} \cdot \hat{n}dS \tag{B.16}$$

Then, using the Reynolds transport theorem B.2, the divergence theorem B.1, and the constitutive equation B.5, the conservative form of the energy balance equation states:

$$\rho\frac{D}{Dt}\left(e + \frac{V^2}{2}\right) = -\rho\dot{Q} - \vec{Q} \cdot \vec{q} + \rho\vec{V}\vec{f} - \vec{\nabla} \cdot (p\vec{V}) + \vec{\nabla}(\vec{V} \cdot \vec{\vec{\sum}}) \tag{B.17}$$

where for Newtonian fluids $\vec{\vec{T}} = -p\vec{\vec{I}} + \vec{\vec{\sum}}$ then $\vec{\nabla}(\vec{V} \cdot \vec{\vec{T}}) = -\vec{\nabla} \cdot (p\vec{V}) + \vec{\nabla}(\vec{V} \cdot \vec{\vec{\sum}})$ and the right-hand terms of the equation is the total derivative:

$$\rho\frac{D}{Dt}\left(e + \frac{V^2}{2}\right) = \frac{\partial}{\partial t}\left[\rho\left(e + \frac{V^2}{2}\right)\right] + \nabla \cdot \left[\rho\left(e + \frac{V^2}{2}\right)\vec{V}\right] \tag{B.18}$$

The final system will look like:

$$\frac{D\rho}{Dt} + \vec{\nabla} \cdot (\rho\vec{V}) = 0 \tag{B.19a}$$

$$\rho\frac{D\vec{V}}{Dt} = -\vec{\nabla}p + \vec{\nabla}\vec{\vec{\sum}} + \rho\vec{f} \tag{B.19b}$$

$$\rho\frac{Dh_0}{Dt} = \frac{\partial p}{\partial t} + \vec{\nabla}(\vec{V} \cdot \vec{\vec{\sum}}) + \rho\vec{V} \cdot \vec{f} + \rho\dot{Q} - \vec{\nabla} \cdot \vec{q} \tag{B.19c}$$

where ρ, $\vec{V}$,T,p are the density, velocity, temperature and pressure fields respectively, while again $\vec{\vec{\sum}}$ is the viscous stress tensor, which, for Newtonian fluids, is written as:

$$\vec{\vec{\sum}} = \mu(\vec{\nabla}\vec{V} + \vec{\nabla}\vec{V}^T) - \tfrac{2}{3}\mu(\vec{\nabla} \cdot \vec{V})\vec{\vec{I}} \tag{B.20}$$

and h_0 is the total enthalpy, defined as:

$$h_0 = h + \frac{V^2}{2} \tag{B.21}$$

The system B.19 is considered complete for an ideal gas, considering the equations in A and the following one: $p = \rho RT$. The viscosity μ follows Sutherland's law in order to account for its variation with temperature

$$\mu(T) = \mu_\infty \left(\frac{T}{T_\infty}\right)^{\frac{3}{2}} \frac{T_\infty + S}{T + S} \tag{B.22}$$

where $S = 110K$ in the case of air. Possibly, a power law can be used to express the viscosity dependence on temperature:

$$\mu(T) = \mu_\infty \left(\frac{T}{T_\infty}\right)^n \tag{B.23}$$

where $n = \frac{2}{3}$ in the case of air.

B.6 RANS

The Reynolds-averaged Navier-Stokes equation is based on the mean value of various signals $U(t)$, averaged over a number of N experiments.The definition of the Reynolds average is:

$$U(x_i,t) = \langle u(x,t) \rangle = \frac{1}{N} \sum_{k=1}^{N>>1} u^{(k)}(x_i,t) \tag{B.24}$$

where $u(x,t)$ is the instantaneous velocity.
If the experiment is performed in a stationary regime, the Reynolds average coincides with the time average and $U(x_i,t) = U(x_i)$. The averaged field of these quantities recovers the symmetries of the boundary condition. The same condition is valid in space.
A fundamental property is that the Reynolds average operator is linear: the derivative of the mean value is equivalent to calculating the average of the derivative.

$$\langle \frac{\partial}{\partial x} u \rangle = \frac{1}{N} \sum_{k=1}^{N>>1} \frac{\partial}{\partial x} u^{(k)} = \frac{\partial}{\partial x} \left[\frac{1}{N} \sum_{k=1}^{N>>1} u^{(k)} \right] = \frac{\partial}{\partial x} \langle u \rangle = \frac{\partial}{\partial x} \langle U \rangle \tag{B.25}$$

B.6.1 Reynolds decomposition

Every instantaneous quantity $u(x,t)$ can be expressed as the sum of the mean value and the fluctuation with respect to the mean value:

$$u(x,t) = U(x,t) + u'(x,t) \tag{B.26}$$

The consequence of considering the Reynolds average is that $\langle u' \rangle = 0$ Considering the Navier-Stokes equations:

$$\frac{\partial u_j}{\partial x_j} = 0 \tag{B.27a}$$

$$\frac{u_i}{\partial t} + \frac{\partial}{\partial x_j}(u_i u_j) = -\frac{1}{\rho}\frac{\partial p}{\partial x_i} + \frac{\partial}{\partial x_j}(2we_{ij}) \tag{B.27b}$$

Applying the Reynolds decomposition and averaging, the RANS equations state:

$$\vec{\nabla} \cdot \vec{U} = 0 \tag{B.28a}$$

$$\frac{D\vec{U}}{Dt} = -\frac{\vec{\nabla} p}{\rho} + \vec{\nabla} \cdot (2we_{ij}) - \vec{\nabla} \cdot \langle u'u' \rangle \tag{B.28b}$$

where $\vec{\nabla} \cdot \langle u_i' u_j' \rangle$ is the symmetric Reynolds stress tensor: $\langle u_i' u_j' \rangle = \langle u_j' u_i' \rangle$

C $\theta - \beta - M$

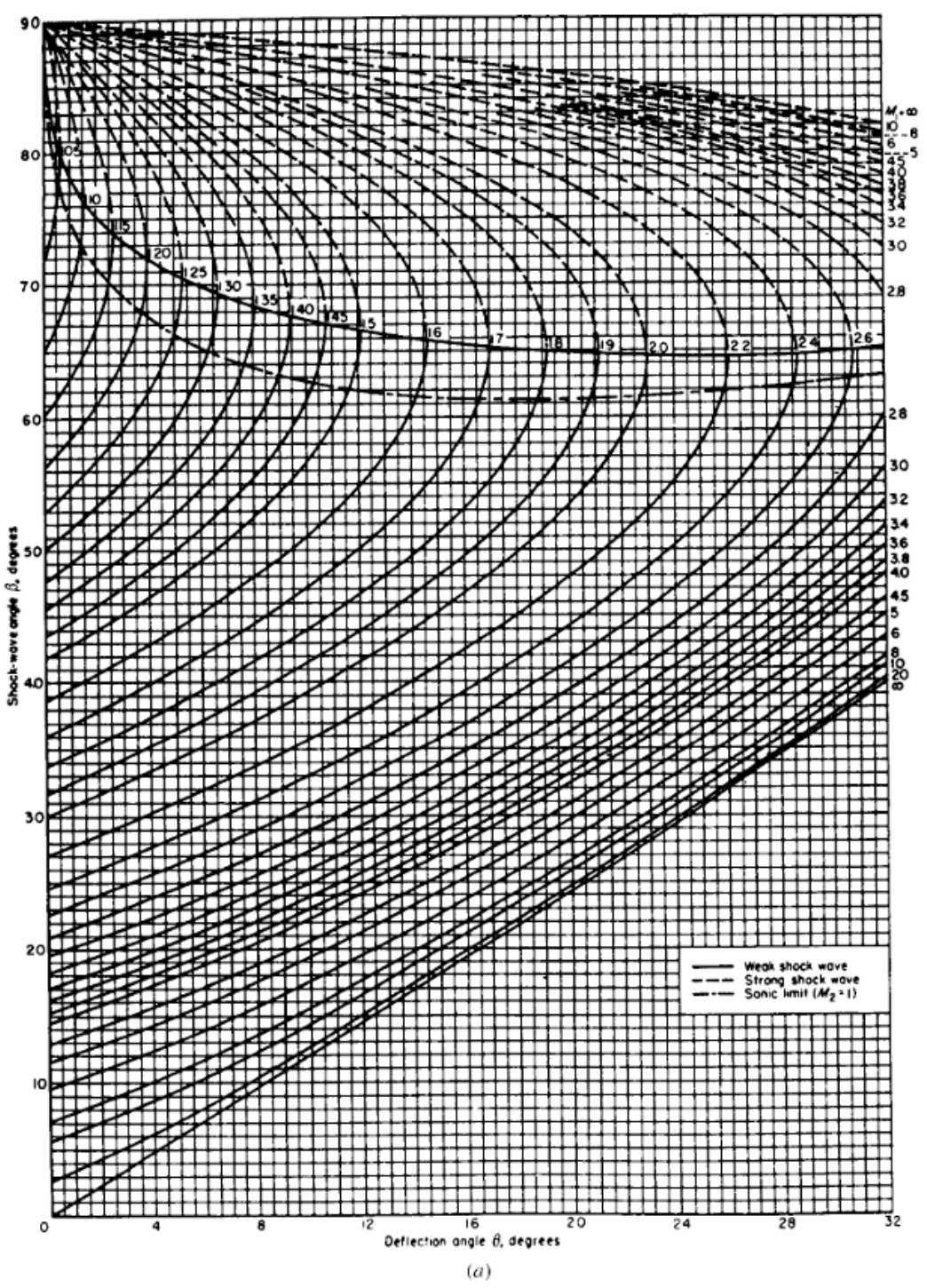

Figure 39: Graph used for the $\theta - \beta - M$ relation for different input values:θ and M.

D Bibliography

References

[1] Prandtl, L. (1925). Bericht uber die Entstehung der Turbulenz. Z. Angew. Math. Mech. 5, 136–139.

[2] von Karman, T. (1930). Mechanische Ahnlichkeit und Turbulenz. In Proc. Third Int. Congr. Applied Mechanics, Stockholm, pp. 85–105.

[3] E. Van Driest. The problem of aerodynamic heating. Aeronaut. Engng. Rev., 15(10):26–41, (1956).

[4] Deardorff, J. W. (1970). A numerical study of three-dimensional turbulent channel flow at large Reynolds numbers. J. Fluid Mech. 41, 453–480. DOI: https://doi.org/10.1017/S0022112070000691

[5] Schumann, U. (1975). Subgrid scale model for finite difference simulations of turbulent flows in plane channels and annuli. J. Comput. Phys. 18, 376–404. DOI: https://doi.org/10.1016/0021-9991(75)90093-5

[6] Baggett, J. S. (1998). On the feasibility of merging LES with RANS for the near-wall region of attached turbulent flows. In Annu. Res. Briefs, pp. 267–277. Center for Turbulence Research.

[7] Nicoud, F., Ducros, F. Subgrid-Scale Stress Modelling Based on the Square of the Velocity Gradient Tensor. Flow, Turbulence and Combustion 62, 183–200 (1999). DOI: https://doi.org/10.1023/A:1009995426001

[8] F Ducros, V Ferrand, F Nicoud, C Weber, D Darracq, C Gacherieu, T Poinsot. Large-Eddy Simulation of the Shock/Turbulence Interaction, Journal of Computational Physics, Volume 152, Issue 2, (1999). DOI:https://doi.org/10.1006/jcph.1999.6238

[9] Pope SB. *Turbulent Flows*. Cambridge University Press; (2000). DOI: https://doi.org/10.1017/CBO9781316179475

[10] Piomelli, U., Balaras, E. (2002). Wall-layer models for large-eddy simulations. Annual Review of Fluid Mechanics, 34(34), 349–374. DOI: https://doi.org/10.1146/ANNUREV.FLUID.34.082901.144919

[11] Rajat Mittal, Gianluca Iaccarino. (2005).*Immersed boundary methods*. Annual Review Fluid Mechanics 37:239-261. DOI: https://doi.org/10.1146/annurev.fluid.37.061903.175743

[12] Piomelli, U. (2008). *Wall-layer models for large-eddy simulations*. Prog. Aero. Sci. 44, 437–446. DOI: https://doi.org/10.1016/j.paerosci.2008.06.001

[13] Wu M, Martin MP. *Analysis of shock motion in shockwave and turbulent boundary layer interaction using direct numerical simulation data*. Journal of Fluid Mechanics. (2008); 594:71-83. DOI: https://doi.org/10.1017/S0022112007009044

[14] Riguette et al., (2009) *"Experimental Study of a Mach* 3 *Compression Ramp Interaction at* $Re_\theta = 2400$*"*. AIAA JOURNAL Vol. 47, No. 2, February 2009 DOI: https://doi.org/10.2514/1.38248

[15] Bermejo-Moreno, I. (2011). *"Wall-modeled large eddy simulation of shock/turbulent boundary-layer interaction"* in. Annual Research Briefs, 49.

[16] Gary S. Settles, Seymour M. Bogdinoff and Irwin E. Vast: "Incipient Separation of a Supersonic Turbulent Boundary Layer at High Reynolds Numbers". DOI: https://doi.org/10.2514/6.1975-7

[17] Jimenez, J. (2012) Cascades in wall-bounded turbulence. Annu. Rev. Fluid Mech. 44, 27–45. DOI: https://doi.org/10.1146/annurev-fluid-120710-101039

[18] T. B. Gatski and J. P. Bonnet. *Compressibility, turbulence and high speed flow.* Academic Press, (2013)

[19] David M. Dawson et al., (2013). *"Assessment of Wall-Modeled Large Eddy Simulation for Supersonic Compression Ramp Flows"*. AIAA 2013-3638. Session: Numerical Analysis of Hyper-/Supersonic Inlets. DOI: https://doi.org/10.2514/6.2013-3638

[20] Johan Larsson et al., (2016). *"Large eddy simulation with modeled wall-stress: recent progess and future directions.* DOI: https://doi.org/10.1299/mer.15-00418

[21] Xing-Kun Zhu, Chang-Ping Yu, Fu-Lin Tong and Xin-Liang Li, Numerical Study on Wall Temperature Effects on Shock Wave/Turbulent Boundary-Layer Interaction, 2016 DOI:https://doi.org/10.2514/1.J054939

[22] Fulin Tong, Changping Yu, Zhigong Tang, Xinliang Li, Numerical studies of shock wave interactions with a supersonic turbulent boundary layer in compression corner:Turning angle effects, 2017. DOI:https://doi.org/10.1016/j.compfluid.2017.03.009

[23] John D. Anderson, Jr (2017) "Fundamentals of Aerodynamics". Published by McGraw-Hill Education, 2 Penn Plaza, New York, NY 10121.

[24] De Vanna F, Cogo M, Bernardini M, Picano F, Benini E, et al. *"A wall-modeled/wall resolved LES method for turbulent wall flows"*. In: ECCOMAS congress 2020.2021. DOI: http://dx.doi.org/10.23967/wccm-eccomas.2020.045.

[25] Ernst Heinrich Hirschel, Arthur Rizzi, Christian Breitsamter, Werner Staudacher (2021). *"Separated and Vortical Flow in Aircraft Wing Aerodynamics"*. DOI: https://doi.org/10.1007/978-3-662-61328-3

[26] Bernardini M et al. (2021). *"STREAmS: A high-fidelity accelerated solver for direct numerical simulation of compressible turbulent flows"*. In: Computer Physics Communications 263. DOI: https://doi.org/10.1016/j.cpc.2021.107906

[27] Kshitij Sabnis, Holger Babinsky. *A review of three-dimensional shock wave-boundary-layer interactions.* Progress in Aerospace Sciences, Volume 143, 2023. DOI: https://doi.org/10.1016/j.paerosci.2023.100953

E Riassunto in italiano

Abstract

La necessità di prevedere la fisica che governa le interazioni tra onde d'urto e strati limite turbolenti è uno dei temi cruciali per le applicazioni dell'ingegneria aerospaziale, che spaziano dal rientro atmosferico, alla progettazione di sistemi di propulsione efficienti, fino all'interazione fluido-struttura e alla riduzione del rumore nei velivoli ad alta velocità. L'elevatissimo costo computazionale richiesto per risolvere tutte le scale presenti in un flusso rappresenta una sfida significativa nelle simulazioni numeriche. Le simulazioni numeriche dirette (DNS) sono limitate a numeri di Reynolds relativamente bassi a causa del loro elevato costo computazionale, mentre le simulazioni ai grandi vortici (LES) utilizzano modelli di sottoscala per rappresentare i moti turbolenti di piccola scala non risolti, rendendo così possibili simulazioni a numeri di Reynolds più elevati. Le simulazioni mediate di Reynolds delle equazioni di Navier-Stokes (RANS), grazie al loro basso costo computazionale, possono essere impiegate su un ampio intervallo di numeri di Reynolds, poiché forniscono accesso al campo di moto medio a scapito di una rappresentazione risolta nel tempo delle caratteristiche locali del flusso. Tuttavia, la cattura delle strutture di strato limite generate dalle pareti solide è ancora proibitiva dal punto di vista computazionale per la maggior parte delle condizioni di flusso di interesse pratico.
Lo scopo di questo lavoro è implementare per la prima volta una tecnica di wall-model per simulazioni LES utilizzando un Immersed Boundary Method (IBM) nel solutore numerico open source STREAmS, riducendo il costo computazionale necessario a descrivere l'interazione tra un flusso supersonico e una rampa di compressione, a partire dal valore di una certa distanza dalla parete, detta posizione di accoppiamento (matching location).
L'attenzione principale è rivolta all'implementazione dello stesso setup e alla validazione rispetto a un lavoro recente presentato da Dawson et al. (2013) [19], in cui il numero di Mach di corrente libera è $M_\infty = 2.9$ e l'angolo della rampa è $\theta = 24°$. I risultati ottenuti utilizzando configurazioni di griglia che vanno da grossolane a fini e diverse posizioni di accoppiamento sono coerenti con le previsioni teoriche. La scelta della posizione di accoppiamento ha un impatto maggiore rispetto alla specifica configurazione di griglia sul coefficiente d'attrito previsto e sulla distribuzione media di pressione nel dominio, evidenziando che, a posizione di accoppiamento fissata ma con diverse configurazioni di griglia, la griglia più fine cattura più efficacemente l'influenza del gradiente di pressione avverso. Essi mettono in evidenza i limiti del modello a parete d'equilibrio nel rappresentare fedelmente la fisica quando si verifica separazione del flusso, in particolare se confrontato con una DNS e con analisi sperimentali, Wu & Martin (2008) [13] e Riguette et al. (2009) [14]. Per quanto riguarda l'onda d'urto obliqua, il modello predice con accuratezza il salto delle proprietà del fluido attraverso l'onda stessa e l'angolo obliquo, con un errore di deviazione inferiore rispettivamente a $\epsilon_{prop} = 4\%$ e $\epsilon_\beta = 2\%$.
In futuro, potrebbe essere utile indagare l'implementazione di modelli in grado di rappresentare flussi fortemente non in equilibrio e superfici rugose, al fine di ottenere una comprensione più completa del caso supersonico.

Introduzione

Negli ultimi anni, l'interesse per lo studio dell'interazione fra strato limite turbolento in regime supersonico e onde d'urto è diventato uno dei principali temi di ricerca. Questo è dovuto soprattutto alla necessità di conoscere e prevedere il comportamento di velivoli che volano dentro e fuori l'atmosfera in regime supersonico o ipersonico, determinando la nascita di carichi aerodinamici e scambi di calore importanti che portano ad influenzare strettamente l'integrità strutturale degli stessi. Conoscere accuratamente come i carichi meccanici e termici si distribuiscono intorno ai velivoli a causa dell'interazione con il flusso rappresenta un nodo cruciale nella definizione di nuove procedure di design più efficienti. La complessità dello studio aumenta quando il flusso è turbolento e compressibile, da qui la necessità di validare nuovi modelli numerici per simulare il comportamento del flusso e soprattutto semplificare lo studio dell'interazione con la parete. I principali modelli numerici usati nella valutazione di flussi in regime turbulento sono:

- DNS: La simulazione numerica diretta ci permette di risolvere tutta la scala turbulenta ma risulta estremamente costosa dal punto di vista computazionale. Questo limite si incontra soprattutto quando vogliamo simulare condizioni simili a quelle reali.

- LES: La simulazione dei vortici di grandi dimensioni permette di ridurre il costo computazionale rispetto alle DNS risolvendo le grandi scale ma modellando quelle piccole. Il modello riesce a cattutare la evoluzione temporale delle grandi scale riuscendo a rappresentare la caratteristica di non stazionarità e multiscala di un flusso turbolento.

- RANS: Le simulazioni mediate di Reynolds delle equazioni di Navier-Stokes risulta essere estremamente poco costosa visto che le scale risultano essere modellate visualizzando solo il campo medio a scapito di una rappresentazione risolta. Migliori per applicazioni industriali.

L'introduzione di un modello a parete che ci permetta di modellare il flusso nella regione vicino alla parete ma risolvere con l'impiego di una LES quello distante dalla stessa è il principale obiettivo della tesi. Il caso di studio prevedere l'implemantazione di un WMLES con IBM nel risoluture numerico STREAmS per simulare l'interazione di uno strato limite turbulento con un'onda d'urto, considerando un flusso a Mach 2.9 e un angolo della rampa di compressione pari a $\theta = 24°$. La validazione è stata effettuata con diverse mesh, dalla più rada alla più fine, in termini di numero di nodi con ulteriore variazione della matching location per osservare i limiti del modello. Per la determinazione del coefficiente di attrito e dell'evoluzione della pressione lungo il dominio, sono stati impiegati come dati di riferimento il caso di studio analogo proposto da Dawson et al., (2013) [19] e da simulazioni DNS ed esperimenti rispettivamente Wu & Martin (2008) [13] e Riguette et al., (2009) [14]. Questo in ultima analisi ci ha permesso di evidenziare la bontà dei risultati ottenuti e di porre i commenti necessari su cui sviluppare un'implementazione migliore in futuro.

Wall-Modeled LES

La strategia adottata ha come obiettivo quello di modellare la regione vicino alla parete e risolvere invece le scale turbolente all'esterno. Basandosi sulla descrizione formulata da Kawai & Larsson (2016)[20], otteniamo un sistema di equazioni partendo dalle equazioni di momento e energia del modello RANS imponendo la condizione di conservazione tra termini convettivi e gradiente di pressione:

$$\frac{d}{dy}\left(\mu_{wm}^{tot}\frac{dU_{wm}}{dy}\right)=0, \tag{E.1}$$

$$\frac{d}{dy}\left(\lambda_{wm}^{tot}\frac{dT}{dy}\right)=-\frac{d}{dy}\left(\mu_{wm}^{tot}U_{wm}\frac{dU_{wm}}{dy}\right) \tag{E.2}$$

L'algoritmo che gestisce il modello è caratterizzato dalla definizione di una posizione dove lo scambio di informazioni tra il modello a parete e il solver LES avviene: questa è definita come matching location. Le equazioni sono risolte tra la parete e la matching location h_{wm}, dove il modello prende come condizioni al contorno le variabili di flusso definite dalla LES: u_{LES}, p_{LES} e T_{LES}. Attraverso il modello otteniamo una stima dello sforzo di taglio τ_w e del flusso di calore scambiato q_w che sono poi mandate nuovamente al solver LES come condizione al contorno. Per il campo definito dalla LES, il valore appropriato di sforzo di taglio e di flusso di calore è poi corretto attraverso l'impiego di una viscosità e diffusività efficace:

$$\tau_w^{LES}=\mu_{eff}\frac{U_i^{int}-U_i^g}{\Delta y_i}=(\mu_w+\mu_w^{SGS})\frac{U_i^{int}-U_i^g}{\Delta y_i} \tag{E.3}$$

$$q_w^{LES}=\lambda_{eff}\frac{T_i^{int}-T_i^g}{\Delta y_i}=(\lambda_w+\lambda_w^{SGS})\frac{T_i^{int}-T_i^g}{\Delta y_i} \tag{E.4}$$

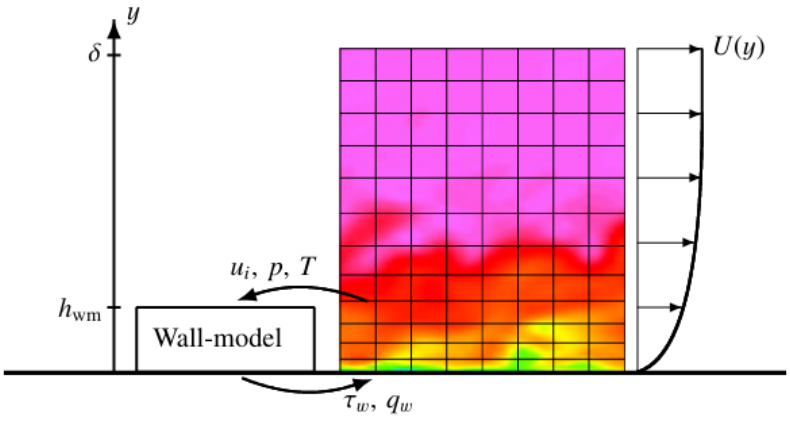

Figure 40: Rappresentazione instantanea dello strato limite con griglia LES e Wall-Model. Il modello a parete modella il flusso in uno strato di spessore h_{wm}: scambio di infomrazioni instantae di velocià e temperature e restituisce lo sforzo di taglio a parete e flusso di calore alla LES, che poi li utilizza come condizioni al contorno, Kawai & Larsson [20].

Setup

L'analisi dell'interazione tra strato limite supersonico turbolento con un'onda d'urto obliqua è stata effettuata sfruttando il codice open source STREAmS (Bernardini et al., [26]) orientato alle moderne piattaforme per il calcolo computazionale ad alte prestazioni che fa uso di librerie per il calcolo parallelo. Il codice supporta architetture multi-GPU e risolve le equazioni di Navier-Stokes per un gas viscoso e termicamente conduttivo. Per la prima volta si è voluto implementare un modello di equilibrio a parete (EWM) con gestione per le condizioni a contorno definite da un modello IBM che permette di impiegare una griglia Cartesiana non conforme con la geometria del corpo, in questo caso una rampa. La condizione di non scorrimento, di non penetrazione e di adiabaticità alla parete è soddisfatta sfruttando un modello che si basa sulla definizione di nodi fantasma (ghost nodes), punti definiti nel volume solido che hanno almeno un punto fluido. L'utilizzo di uno schema numerico di secondo ordine per le quantità vicino alla parete permette di garantire l'efficacia del modello garantendo il valore corretto di sforzo di taglio e di flusso di calore senza sfruttare una griglia eccessivamente fine vicino alla parete. Il dominio computazionale che deve essere gestito è definito come $140\delta \times 40\delta \times 9\delta$ dove un assottigliamento della mesh è implementato in corrispondenza della rampa in modo tale da risolvere maggiormente senza uscire dallo scopo della tesi.

Risultati

I risultati sono distinti fra qualitativi e quantitativi. L'analisi è volta ad osservare la qualità dei dati ottenuti per capire i limiti e le potenzialità di un modello di equilibrio a parete. La valutazione delle quantità medie di pressione, densità e temperatura mostra invece come il salto delle proprietà termodinamiche relative all'onda d'urto obliqua è catturato adeguatamente. Conferma è poi data dalla determinazione dell'errore percentuali del salto di proprietà fra monte e valle, angolo dell'onda d'urto obliqua e della valutazione del Mach di valle. Gli errori rispettivamente sono $\epsilon_{prop}\% = 4$, $\epsilon_{\beta}\% = 2$ e $\epsilon_{M_{valle}}\% < 5$. Si può considerare ora la valutazione del profilo di velocità e quindi dello spessore dello strato limite lungo il dominio. I profili ottenuti restituiscono una buona coerenza con la teoria del fenomeno di studio in esame, evidenziando le variazioni a cui sono soggette le variabili del flusso. La visualizzazione della vorticità, permette di osservare come in prossimità della rampa vi sia un incremento di tale caratteristica del flusso sottolineando l'effetto di un gradiente avverso di pressione e dell'aumento di temperatura data la natura fortemente entropica dell'onda d'urto. Il confronto con i dati di riferimento, come DNS e WRLES, sottolinea come nella zona prima della rampa il modello catturi molto bene il profilo, cosa che non succede per quanto riguarda la zona di ricircolo e lungo la rampa, dove il modello non è in grado di riprodurre correttamente il profilo di velocità. Il coefficiente di attrito C_f e la variazione della pressione P/P_∞ lungo il dominio evideniziano i limiti del modello nella riproduzione corretta del punto di separazione, della zona di ricircolo e del punto di riattacco rimarcando un limite nel visualizzare un C_f negativo coerente con il gradiente avverso del caso di studio. Il profilo di pressione ottenuto rispetto a quelli di riferimento presenta un andamento buono soprattutto nella zona pre separazione sottolineando nuovamente i limiti del modello nel riprodurre correttamente i fenomeni di non equilibrio.

Conclusioni

L'obiettivo della tesi è quello di analizzare per la prima volta un modello di equilibrio per modellare la regione vicino a parete, sfruttando un IBM per la gestione della griglia Cartesiana e delle condizioni al contorno. Per quanto riguarda l'interazione dello strato limite turbolento con un'onda d'urto obliqua dovuta alla geometria del problema, sono stati ottenuti dei buoni risultati, ma con limitazioni nella valutazione di una regione caratterizzata da un forte gradiente di pressione e quindi da fenomeni di non equilibrio. Il modello restituisce una adeguata approssimazione delle variazioni delle proprità termodinamiche con un errore percentuale pari a $\epsilon_{prop}\% = 4$. Lo stesso, nella determinazione attraverso il gradiente di pressione della linea dell'onda d'urto obliqua e del Mach di valle $\epsilon_{\beta}\% = 2$ e $\epsilon_{M_{valle}}\% < 5$. Le limitazioni principali le riscontriamo nella determinazione del profilo di velocità insieme al coefficiente di attrito. Per quanto riguarda il profilo di velocità, osservando la sua evoluzione a diverse stazioni del dominio, si può evidenziare come il modello di equilibrio riproduca correttamente il profilo nella zona liscia, prima della zona di separazione, dove abbiamo un valore costante del gradiente di pressione. I profili nelle stazioni successive riportano l'influenza del gradiente avverso, ma soprattutto l'incapacità del modello di riprodurre correttamente il profilo nella zona vicino alla parete. Stesse limitazioni si incontrano nella valutazione del coefficiente di attrito dove il modello fallisce nel riprodurre un C_f negativo, aspettato teoricemente, che non riproduce accuratemente la zona di riattacco del flusso lungo la parete sottolineando una instabilità nel modello stesso. Questo è confermato dall'andamento medio della pressione lungo il dominio, rimarcando come le zone di ricircolo e di riattacco non siano coerenti con quelle riportate dai dati DNS di riferimento. In futuro quindi sarà necessario migliorare il modello per valutare correttamente gli effetti di non equilibrio.
Un ulteriore modifica è legata alla possibilità di implementare una superficie rugosa in modo da approsimare maggiormente casi reali di studio per possibili applicazioni aeronatiche.